RADIO FREQUENCY SENSOR ARRAYS FOR DIELECTRIC CONSTANT ESTIMATION

BY

MUHAMMAD TAYYAB

A Thesis Presented to the
DEANSHIP OF GRADUATE STUDIES

KING FAHD UNIVERSITY OF PETROLEUM & MINERALS

DHAHRAN, SAUDI ARABIA

In Partial Fulfillment of the
Requirements for the Degree of

MASTER OF SCIENCE

In

ELECTRICAL ENGINEERING

MAY 2017

KING FAHD UNIVERSITY OF PETROLEUM & MINERALS
DHAHRAN 31261, SAUDI ARABIA

DEANSHIP OF GRADUATE STUDIES

This thesis, written by **MUHAMMAD TAYYAB** under the direction of his thesis adviser and approved by his thesis committee, has been presented to and accepted by the Dean of Graduate Studies, in partial fulfillment of the requirements for the degree of **MASTER OF SCIENCE IN ELECTRICAL ENGINEERING**.

Thesis Committee

Prof. Mohammad S. Sharawi (Adviser)

Prof. Abdelsalam Al-Sarkhi (Member)

Dr. Khurram K. Qureshi (Member)

Dr. Ali Ahmad Al-Shaikhi
Department Chairman

Prof. Salam A. Zummo
Dean of Graduate Studies

17/5/17
Date

To My Lovely Father (Muhammad Rafique), Mother, Wife, Doughter (Zainab Batool), Son (Muhammad Hussain), Nephew (Muhammad Hanzala) and Brothers.

ACKNOWLEDGMENTS

First praise is to Allah, the Almighty, on whom ultimately we depend for sustenance and guidance. Moreover, may his peace and blessings of Allah be upon Prophet Muhammad (PBUH), a guidance and inspiration to our lives.

I wish to express my appreciation to Prof. Mohammad S. Sharawi for the new ideas, useful comments, remarks and engagement through the learning process of this master thesis. I would also like to express my gratitude to Prof. Abdelsalam Al-Sarkhi for the fluid mechanics lab support. I also wish to thank my thesis committee member Dr. Khurram K. Qureshi for his valuable comments. I would like to thank King Fahd University of Petroleum and Minerals (KFUPM), for the support of materials and funds. I would like to thank Dr. Atif Shamim and his research group, King Abdullah University of Science and Technology (KAUST), for their support in fabrication and experimental validation of the biomedical sensor. I would finally, like to thank my loved ones, who have supported me throughout the entire process. I will be grateful forever for your love.

TABLE OF CONTENTS

LIST OF TABLES

LIST OF FIGURES

THESIS ABSTRACT

NAME:	Muhammad Tayyab
TITLE OF STUDY:	Radio Frequency sensor arrays for dielectric constant estimation
MAJOR FIELD:	Electrical engineering
DATE OF DEGREE:	May 2017

Coming up with radio frequency (RF) sensors and methods for estimating the dielectric constant of substances in an evolving field. Such sensors have important applications in biomedical and oil exploration areas in addition to many others. This work will present RF sensor arrays for the biomedical and oil exploration applications.

The measurement of the single phase portion in a multiphase flow is very important to oil and petrochemicals industries. This work presents an RF sensor design for dielectric constant estimation of two or three phase combinations of oil, water and gas. The 28-port RF sensor is designed and optimized to operate at 250 MHz. Using the transmission coefficient of each RF sensor port, an equation is obtained for dielectric constant estimation by applying the Least Squares (LS)

method. Three different static two phase combinations including oil-water, gas-water, gas-oil and three phase combination of oil-water-gas are experimentally validated with an average measured error percentages of 5.5%, 17.3%, 16% and 6.2% respectively. A shake test (dynamic case) for the three phase combination was performed to resemble an actual three phase flow and the average measured error was 9.3%. The proposed sensor can estimate two or three phase combination of oil, water and gas with an average error of less than 10%. The proposed sensor is low cost, with low complexity and is the first to provide low error estimations to 2 or 3-phase static or dynamic flows that was implemented on a flexible AP9131 substrate of 0.1016 mm thickness and $6 \times 27.93cm^2$ size that can be wrapped around an acrylic pipe.

The second part of this work presents the design of an RF sensor array for pulmonary edema monitoring inside the patient chest. A low complexity, low power, small size, wearable, Inkjet printed, cheap and non-invasive radio frequency (RF) based sensor array for pulmonary edema and emphysema monitoring inside the patient chest is proposed. The RF sensor consists of 38 electrodes and 37 ports. The size of the sensor is $4cm \times 89.4cm$. The sensor is optimized to operate at 60 MHz. The transmission coefficients S_{i1} are measured at each passive port and then the LS method is used to form an equation for average dielectric constant estimation. The dielectric constant estimation method is used to detect the presence of excess water/air in the lungs. Using a dielectric assessment kit (DAK), the electrical properties of outer and inner layers of a human and porcine lungs

are obtained using different solutions of water, salt, isopropyl alcohol (IPA) and glycerin. The average measured dielectric constants of normal human lung, edema and emphysema infected lungs are estimated with errors of 3.54%, 4.83% and 4%, respectively. Another test was conducted using porcine lung electrical properties which are formed using a water and salt mixture. To detect the different stages of pulmonary edema, 200 ml water balls are inserted in the inner layer of the chest model. The measured errors are 2.68%, 0.87%, 2.18% and 2.8% for normal porcine lung, adding 6 water balls, adding 12 water balls and adding 18 water balls, respectively. The proposed sensor array can be integrated within clothes, thus making it easy for patients to be monitored.

ملخص الرسالة

الاسم: محمد طيب

عنوان الدراسة: مصفوفات مجس راديو التردد لتقدير ثابت العزل الكهربائي

التخصص: الهندسة الكهربائية

تاريخ الدرجة العلمية : أيار 2017

الإتيان بمجسات راديوية التردد (RF) وطرق لتقدير ثابت العزل الكهربائي للمواد في مجال متطور. تلك المجسات لديها تطبيقات هامة في مجالات الأبحاث النفطية والطبية الحيوية بالإضافة إلى مجالات أخرى. هذا العمل يستعرض مصفوفة مجس RF لتطبيقات الأبحاث النفطية والطبية الحيوية.

القياسات الخاصة بقسم أحادي الطور في تدفق متعدد الأطوار هام جداً في صناعات النفط والبتروكيماويات. هذا العمل يستعرض تصميم مجس RF لتقدير ثابت العزل الكهربائي لتركيبات ثنائية أو ثلاثية الأطوار من نفط وماء وغاز. مجس RF ذو الـ28 منفذ تم تصميمه ومعايرته ليعمل على تردد 250 ميجاهيرتز. استخدام معامل الانتقال لكل منفذ مجس RF، تم الحصول على معادلة لتقدير ثابت العزل الكهربائي من خلال تطبيق طريقة التربيعات الأقل (LS). ثلاثة تركيبات مختلفة ثنائية الأطوار تحتوي على نفط-ماء، غاز-ماء، غاز-نفط وتركيبات ثلاثية الأطوار من نفط-ماء-غاز تم التحقق منها عملياً مع معدل نسب خطأً مُقاسة 5.5%، 17.3%، 16% و 6.2% بالترتيب. اختبار اهتزازي (حالة متحركة) للتركيب ثلاثي الأطوار تم تطبيقه لمماثلة التدفق ثلاثي الأطوار الحقيقي وكان معدل الخطأ المُقاس 9.3%. المجس المقترح يمكنه تقدير تركيب ثنائي أو ثلاثي الأطوار من نفط، ماء وغاز بمتوسط خطأ أقل من 10%. المجس المقترح منخفض السعر، مع تعقيد منخفض وهو الأول الذي يوفر تقديرات منخفضة الخطأ لتدفقات ثابتة أو متحركة ثنائية أو ثلاثية الأطوار التي تم تنفيذها على مادة AP9131 مرنة بسمك مقداره 0.1016 ملليميتر وحجم 6×27.93 سنتيميتر مربع التي بالإمكان لفها حول أنبوب أكريليكي.

الجزء الثاني من العمل يستعرض التصميم لمصفوفة مجس RF لمراقبة الوذمة الرئوية داخل صدر المريض. تم اقتراح مصفوفة مجس RF منخفض التعقيد، منخفض القدرة، صغير الحجم، قابل للارتداء، مطبوع من خلال نفث الحبر، رخيص غير ضارة لمراقبة الوذمة الرئوية والانتفاخ الرئوي داخل صدر المريض. مجس الـ RF يحتوي على 38 قطب كهربائي و 37 منفذ. حجم المجس هو 4×89.4 سنتيميتر مربع. المجس تم معايرته ليعمل على تردد 60 ميجاهيرتز. معاملات الانتقال Si1تم قياسها على كل منفذ غير فعالومن ثم تم استخدام طريقة التربيعات الأقل LS لتكوين معادلة لتقدير معدل ثابت العزل الكهربائي. طريقة تقدير ثابت العزل الكهربائي تم استخدامها لكشف ظهور فائض ماء/هواء في الرئتين. باستخدام عدة تقديرات العازل (DAK)، تم الحصول على الخصائص الكهربائية للطبقات الداخلية والخارجية للإنسان ورئيتي الخزير باستخدام محاليل مختلفة من ماء، ملح، ايزوبروبيل (IPA) وجلسيرين. معدل ثوابت العزل الكهربائي المُقاسة لرئتي الإنسان الطبيعي، المصابة بالوذفة الرئوية والمصابة بالانتفاخ الرئوي تم تقديرها بنسبة خطأ 3.54%، 4.83% و 4% بالترتيب. اختبار آخر تم باستخدام الخصائص الكهربائية لرئة الخنزير والتي تم تشكيلها باستخدام مزيج من الماء والملح. لكشف المراحل المختلفة للوذمة الرئوية، تم إدخال كرات تحوي 200 مل ماء للطبقة الداخلية من نموذج الصدر. الخطأ المُقاس يساوي 2.68%، 0.87%، 2.18% و2.8% لرئة الخنزير الطبيعية، بإضافة 6 كرات من الماء، بإضافة 12 كرة من الماء وبإضافة 18 كرة من الماء، بالترتيب. مصفوفة المجس المقترحة يمكنها أن تتكامل مع الملابس، لذا، تصبح سهلة لمراقبة المرضى.

CHAPTER 1

INTRODUCTION

Non-invasive monitoring methods of material or fluids is an important aspect in oil industries as well as medical applications. These methods are important to track material or fluid property changes. The techniques available for multi phase flow measurements in the oil industry are, the conventional method, impedance technique, radiation attenuation method, resonant cavity method, pulse neutron activation, nuclear magnetic resonance (NMR), x- ray and microwave methods. Many of them are expensive and have bulky measurement setups. A method for continuous, uninterrupted and unattended monitoring of the 2-phase and 3-phase combination of oil, water and gas is an important requirement for the oil industry.

The traditional methods of non-invasive imaging in the medical field are the magnetic resonance imaging (MRI), computed tomography (CT) and X-ray. These methods are expensive and require heavy equipment. The frequent use of these methods will effect the patients health due to hight frequency exposure. Unattended and uninterrupted monitoring of a patient health is an essential requirement in medical devices. The commercial available devices can monitor respiration rate, temperature and heart rate. Some wearable health monitoring devices are also available. But these devices cannot monitor deep tissue changes and many of them are very expensive. A low cost, wearable and continuously monitoring sensor is an important requirement in medical field.

1.1 Applications of Dielectric Constant Estimation

We can apply dielectric constant estimation methods to both the oil industry and medical fields among many others such as food and drinks industries. We focus here on the oil and biomedical aspects.

- In oil industry, the volume fraction of individual substances can be calculated by estimating the average dielectric constant of the multiphase flow inside the pipeline.
- The different stages of pulmonary edema (due to accumulation of fluid inside the lungs) and emphysema (due to accumulation of air inside the lungs) can be differentiated by the average dielectric constant estimation of the human chest tissue.

In this work, we will propose RF sensor solutions and this accompanied with dielectric constant estimation methods are used to address the multiphase flow in plastic pipelines as well as monitoring the fluid content for pulmonary edema patients.

1.2 2-Phase/3-Phase oil combination

Multiphase flow occurs in the oil and gas industry, steam generators, heat exchangers, oil transportation, chemical reactors and a lot of process equipments. It also exists in many industries including drinks and food. The efficient separation of substances and the drilling process will determine the profit margin in the oil industry. The volume fraction of individual components in two or three phase oil combinations provides an indication for the drilling process to be stopped or continued. The complications in measuring the multiphase flow are significantly more than those for a single phase one.

Due to the increasing demand of petroleum in the world, there are continuous exploration and development of oil and gas reserves. Thus, the optimization and development of techniques for monitoring multiphase flow is required. As non invasive measurement techniques does not requires any change in the existing process, high interest has been developed for such methods for the measurement of multiphase flow. The capital cost of current multiphase flow meters is in the range of 100 thousand to 1 million USD [1].

To maximize the amount of oil that can be retrieved, water and gas might be injected at various points into the well. As oil is removed, the injected water is used to maintain the pressure within the well and gas might be used to reduce the viscosity of oil. To optimize the process for both operation and transportation, measuring and monitoring the produced mixture fractions (oil, water and gas) are very important requirements.

Three ways to measure multiphase flows were summarized in [2]. The first method is the separation of each phase using 3-phase gravity separator. Liquid and gas will separate due to lower density of gas than the liquid. The oil and water will separate due to their difference in densities and viscosities. The second method is by using multiphase flow meters which include, differential pressure (DP) meter, cross-correlation meter, electrical properties meter, microwave method and gamma ray attenuation method. In microwave method, multiphase mixtures can be measured by resonance and absorption. The individual phase fractions of the mixture are determined by the difference in permittivity. In the gamma ray attenuation method, nuclear sources used are the Caesium 137, Barium 133 and Americium 241. The gas is a weak and water is a stronger absorber of gamma rays. So, single energy attenuation uses the high energy gamma ray to distinguish the liquid from the gas and DEGRA (dual-energy gamma ray attenuation) uses both the low and high energy gamma ray emitted to firstly distinguish the oil from the water and then gas from the liquid. The third method is the partial separation which is used when multiphase mixture has a high gas volume fraction ($> 95\%$). A single phase meter such as venturi tube can be used to measure the gas stream.

In [2], [3], difficulties in measuring multi-phase flows (MPFs) are discussed. In the conventional approach, the mixture is separated into individual components and then the measurement is done using single-phase flow (SPF) meters. For an acceptable accuracy, most meters deal with homogeneous flows but in reality MPFs are inhomogeneous. There are some problems with three-phase separators like, high installation cost, bulky equipment, considerable maintenance and more time required for the measurement . A current injection technique with voltage measurement circuits was used for electrical resistance tomography (ERT). An electromagnetic tomography (EMT) sensor consists of a set of excitation coils for producing a magnetic field and a set of detection coils to detect the changes in field due to the variation in conductivity and permeability. The image resolution of EMT is poor. Electrical capacitance tomography (ECT) is based on measuring the changes in capacitance due to the change in dielectric properties. A multi-electrode sensor (typically 8 or 12) is used for capacitance measurement. In ECT, electrode 1 is excited and 2-8 are the detectors. Then, electrode 2 is excited and 3-8 behave as detector, and so on, up to the excitation of electrode 7 and detection of electrode 8. Advantages of ECT includes, rapid response, no radiation, low cost, non-invasive, ability to withstand high pressure and temperature.

The techniques available for the multi-phase flow measurements are, conventional method, impedance technique, radiation attenuation method, resonant cavity method, pulse neutron activation, nuclear magnetic resonance (NMR), x- ray and microwave method [4-8]. These techniques have their own advantages and disadvantages. Many of them work for only two phase flows with a water fraction greater than 10%. Impedance techniques include ECT and ERT. For these techniques, there is a need to identify the flow pattern first before the measurements. These are sensitive to changes in the electrical properties due to temperature. Such techniques cannot be used over the full component fraction range like (0 to 100% of water). They are dependent upon the flow regime. ECT works only for continuous oil flows, up to the possibly 30% water, for higher water levels, the metering has to be switched to ERT. The radiation attenuation method is costly and have safety issues due to high radiation frequencies. It is difficult to implement in the field. Its probes disturb the flow field. It is limited to high water concentrations ($> 10\%$). In water continuous flows, the resonant cavity method cannot be used because, if the conductivity of the mixture is too high, the cavity will not resonate. The pulse neutron activation method is very expensive. But it can be used to determine the wide range of substance fractions. The NMR method uses complex and high-cost technology. The x-ray method is expensive and includes some health risks.

In this work, we will focus on the Microwave method in which measurements can be made without affecting the fluid flow. Previous works on microwave methods are limited to high water concentrations ($> 10\%$) and mostly can work for two or three phase combination only. We will focus on a non-invasive technique for measuring the volume fraction of two or three phase oil combinations. Our objective is to design a sensor array with very small size, low complexity and cost which will wrap around on the oil non-metallic pipe and estimate the dielectric constant inside the pipe. From the dielectric constant calculation, we can estimate the volume fraction of the individual substance of the two or three phase oil combinations.

1.3 Pulmonary Edema Monitoring

The traditional methods for non-invasive imaging of deep tissues within the human body are X-rays, Computed Tomography (CT) and Magnetic Resonance Imaging (MRI). But these techniques have many disadvantages such as unsuitability for continuous time monitoring, the patient must visit the hospital, expensive, difficult to carry due to large and heavy equipment and side effects if frequently used. Wearable and continuous health monitoring sensors are discussed in [9] and [10]. These are limited for monitoring breathing, heart rate and skin temperature. These sensors have advancements in data collection but they lack deep tissue monitoring.

Non-invasive imaging techniques include electrical impedance tomography (EIT), ultrasound impedance tomography and microwave imaging [11]. By measuring the voltages and currents on the periphery of the body, EIT [11-14] reconstructs the spatial conductivity and permittivity within it. Abnormalities can be detected by recording changes in measured voltages or potential difference in the body density. EIT was used to monitor the respiratory function in 1983. The applications of EIT include, real time imaging of ventilation, allows noninvasive repeated measurements of the changes in the lung volume and detection of collapsed lungs. This technique is limited to bed side applications due to the complex circuitry needed for the generation of the variable current patterns. Its accuracy is low due to tissue diversity and being able to reconstruct abnormal shapes. Ultrasound relies on the acoustic properties of tissues. The transmitted wave face reflection, transmission and diffraction through the tissues. Its operating frequency is low (1-20 MHz) to ensure deep tissue penetration. Ultrasound works based on the reflected signal amplitude and time delay. The ultrasound transducer generate and receive sound waves. The early received echoes are from close to surface structures and later ones are from the deep tissue [15]. The echoes are separated by the time delay of reception and the received signal strength. This technique is mostly suitable for soft tissues and not for bones. Its applications include, abdominal, cardiac, urological, fetal, pediatric and fluid detection measurements and analysis. The ultrasound device can be portable but not wearable. Its accuracy is limited due to increased attenuation at high frequencies which results in signal loss and dispersion.

Microwave imaging is used to recover exact electrical properties (permittivity and conductivity) from the frequency range of 300 MHz to 30 GHz. In this technique, an array of wide band antennas is placed around the body to collect the back scattered and bi-static data. The main issues for using this technique are, the high frequency of operation and small depth of penetration. This technique is applicable for near fields only. It is used for breast cancer detection and treatment response monitoring [16]. The portability and wearablity is not possible due to the complex circuitry for sending and receiving wide-band signals. The accuracy is effected due to the lossy characteristics of biological tissues at microwave frequencies and also deep tissue monitoring is not possible.

In short, EIT and ultrasound give a contrast image rather than actual values of electrical properties and microwave methods have high frequency of operation hence small depth of penetrations. There is no technique which combine compactness and accurate dielectric properties measurements within the same device.

The proposed on body monitoring system combines a wearable sensor with deep tissue monitoring such that the changes in the tissues reflect changes in the electrical properties. This is beneficial for patients at risk of having pulmonary edema disease (due to fluid accumulation in lungs) and emphysema (due to air accumulation in lungs). In our design, we propose an RF sensor operating at 60 MHz that is very small, low cost and of low complexity. The proposed sensor have many features. The substrate is a thin polyimide sheet which is flexible and can be integrated within wearable cloths (T-shirts). An Inkjet printer is used for sensor fabrication. The input power and operating frequency is low which reduces health risks. It is simple to implement and light weight. It is non-invasive and non-intrusive. Its size is $4 \times 89.4cm^2$. The chest model used for the measurements is elliptical and close to the average adult chest. An average error of less than 3.3% was measured for human (normal, edema, emphysema conditions) and porcine lungs with different stages of pulmonary edema. The sensor can monitor the inner tissues of the human body deep to 11.64 cm. The achieved dynamic range for low to high ϵ_r variation is 20 dB. It can detect the presence of water in the whole area of the human upper chest.

1.4 Theoretical Background

The materials with dominant bounded positive and negative charges are called dielectrics. These bounded charges are not free to travel. When an external field is applied to these bounded charges, their centroid shift in position slightly relative to each other, thus electric dipoles are created. These polarized dipoles provide the material the ability to store electric energy. The dielectric constant is the ability of a substance to store electrical energy in an electric field. The larger its value, the greater is the ability to store energy. It is a ratio between permittivity of a substance to the permittivity of the free space (8.85×10^{-12} farad per meter (F/m)) [17].

1.4.1 Scattering Parameters

The incident and reflected power of a two port network can be calculated using S-parameters [18]. The S-parameters are usually normalized to a particular impedance (50 ohms). The S_{11}, S_{21}, S_{12}, S_{22} are called the input reflection coefficient, the forward transmission coefficient, the reverse transmission coefficient and output reflection coefficient, respectively, for a two port network as shown in Fig. 1.1.

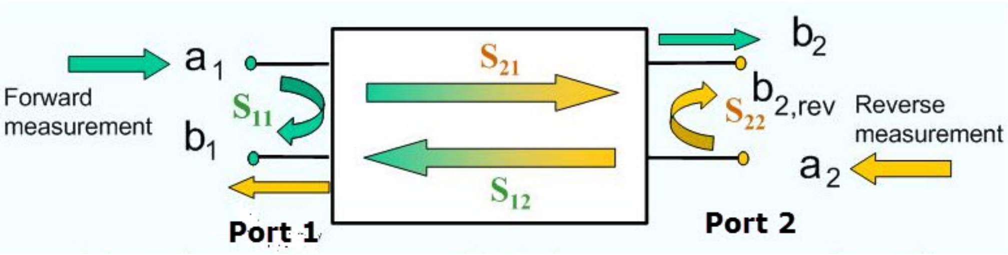

Figure 1.1: S-parameters of two port network

In this work, we have a multi port network and we will focus on the transmission coefficient S_{i1} where i is the port number. In a sensor array, the first port is active and the other ports received the radiated fields. The transmission coefficients are measured at each passive port for dielectric constant estimation. The setup of port read out is shown in Fig. 1.2.

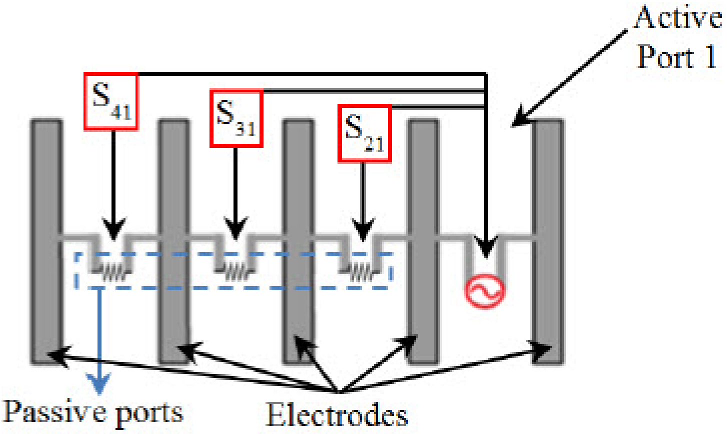

Figure 1.2: Setup of port read-outs [11]

1.4.2 Dielectric Constant Estimation

The effective dielectric constant (ϵ_r) of an oil, water and gas mixture was calculated for multiphase flow using (1.1) in [19], where d is the volume fraction of water, r is the volume of gas, $(1-d-r)$ is the volume of oil, ϵ_{water} is the dielectric constant of water with value of 81, ϵ_{oil} is the dielectric constant of diesel oil with value of 2.2 and ϵ_{gas} is the dielectric constant of gas with value of 1.

$$\sqrt{\epsilon_r} = d\sqrt{\epsilon_{water}} + (1-d-r)\sqrt{\epsilon_{oil}} + r\sqrt{\epsilon_{gas}} \tag{1.1}$$

The dielectric constant can be estimated for both 2-phase/3-phase oil combinations and pulmonary edema monitoring sensors using Equation (1.2) [20] where w_{i-1} are the weight coefficients which can be determined using the Least Squares (LS) method, S_{i1} are the transmission coefficients and i is the port number. In RF sensor array, we excite the first port and the scattered field is collected by the other ports. The signal received (S_{i1}) at farthest electrode have more dependence on the deep layer tissues properties as shown in Fig. 1.3. Each port can sense different depths. The sensor array can provide accurate ϵ_r estimation as a function of depth by applying proper calibration. We are interested in overall signal level S_{i1} which should be large and vary from port to port. By changing the inner layer ϵ_r from low to high values, the dynamic range can be seen from active port to the farthest one as shown in Fig. 1.4. To precisely detect the minor changes of ϵ_r, the dynamic range should be large.

$$\epsilon_r = \sum_{i=2}^{28} w_{i-1} S_{i1} \tag{1.2}$$

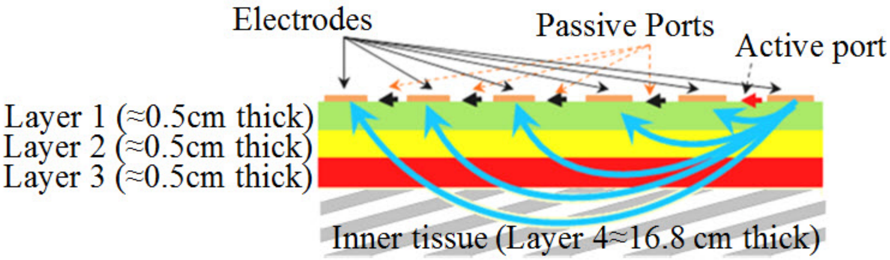

Figure 1.3: Illustration of signal propogation through different layers [11]

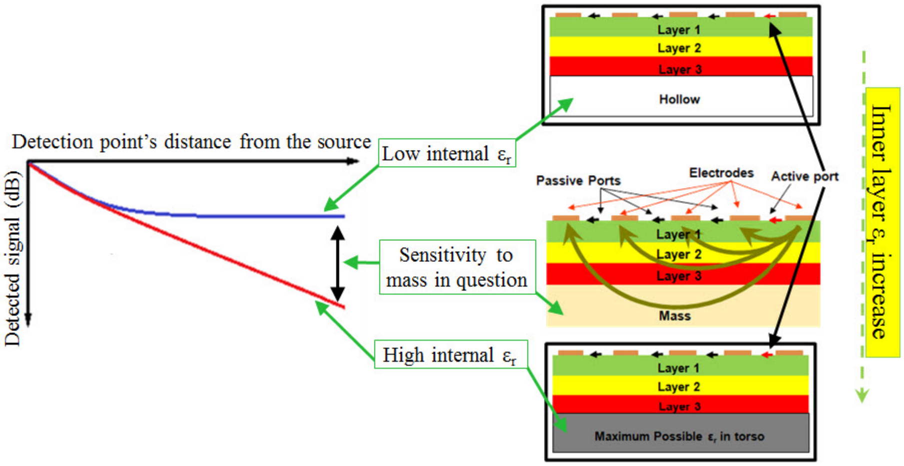

Figure 1.4: Port read-outs and dynamic range in [11]

1.4.3 Least Squares Method

The LS method is used to approximate the solution of overdetermined system. This method can be used, when the number of equations are more than the number of unknowns. The overall solution of LS method minimizes the sum of squares of errors made in result of each equation solution. In (1.3), A is the overdetermined matrix which we are going to solve using LS method, x are the number of unknown which we need to determine and b is the solution matrix of each equation. We need to find x that makes $A.x$ as close to b as possible. In our case, multiple simulations are conducted in HFSS for various dielectric constant values to obtain the weight coefficients using collected transmission coefficient values of multiple port sensor. The equation (1.5) and (1.6) is th LS method formula to obtain the weight coefficients [21]. The pseudo-inverse ($pinv(C)$) or left inverse of C can be found using (1.7).

$$Ax = b \tag{1.3}$$

multiply both sides with A^T

$$A^T Ax = A^T b \tag{1.4}$$

$$x = inv(A^T A)A^T b \tag{1.5}$$

For singular or non square matrix,

$$x = pinv(A^T A)A^T b \tag{1.6}$$

Let $C = A^T A$, where,

$$pinv(C) = (C^T C)^{-1} C^T \tag{1.7}$$

1.4.4 Specific Absorption Rate (SAR)

The SAR measurement evaluate the safety limits of a wireless medical device or antenna. Power absorbed by tissues surrounding the antenna/sensor is a critical parameter. Hence, SAR analysis is required to evaluate the antenna/sensor performance. The SAR is defined in [22] as,

$$SAR = \int_{sample} \frac{\sigma(r)|E(r)|^2}{\rho(r)} dr \tag{1.8}$$

where $|E(r)|^2$ is the root mean square electric field strength, σ is conductivity and ρ is the mass density of the tissue sample. The unit of SAR is watt per kilogram (W/Kg). The SAR can be averaged over a small volume or over the whole body. According to IEEE standard, 10 grams averaged SAR value is limited to 2 W/Kg. The Federal Communication Commission (FCC) limits 1 gram average SAR to 1.6 W/Kg. According to IEEE and FCC, the whole body SAR value is limited to 0.08 W/Kg. The effective radiated power (ERP) of the devices outside the human body is limited to 25 uW by FCC.

1.5 Thesis Objectives

The objectives of this work include the following,

1. Design of a Radio Frequency (RF) sensor array for dielectric constant estimation of multiphase oil flow in pipelines with low cost, low complexity and small in size (wrapped around on oil pipe), operating below 300 MHz, works for

2-phase and 3-phase, static and dynamic cases with average error less than 10%.

2. Design of a Radio Frequency (RF) sensor array for pulmonary edema monitoring that is low cost, low complexity and small in size, operating below 100 MHz with average error should be less than 10% and can be installed on clothes for complete portability.

3. Characterize and assess the performance of the two sensor arrays in a laboratory environment.

CHAPTER 2

LITERATURE SURVEY

This chapter presents the literature review for 2-phase/3-phase oil combination and biomedical sensors.

2.1 2-Phase/3-Phase Oil Combination Sensors

There are seven different types of available sensors for measuring the single phase in a 2-phase/3-phase oil combination in literature. These are:

- Gamma ray
- Capacitance sensor
- Microwave sensor
- Resonant cavity sensor
- X-ray
- Dual modality sensor
- Electrical impedance tomography (EIT) sensor

2.1.1 Gamma Ray

Gamma ray measurements were applied to estimate the volume fraction of multiphase flow in [1]. The root mean square error percentage (RMSEP) for the half test data of oil, water and gas was 39.2%, 6.3%, 37.4% respectively. After application of average linear scaling, the RMSEP for oil, water and gas was 8.9%, 4.4% and 6.5% respectively. The gamma ray attenuation measurement technique in [1] is shown in Fig. 2.1. Three different vertical positions (-36, 0, 36) were marked on the cross section of the pipe. The distance between each position was 2 mm. The intensity of the detected gamma ray was measured at that positions.

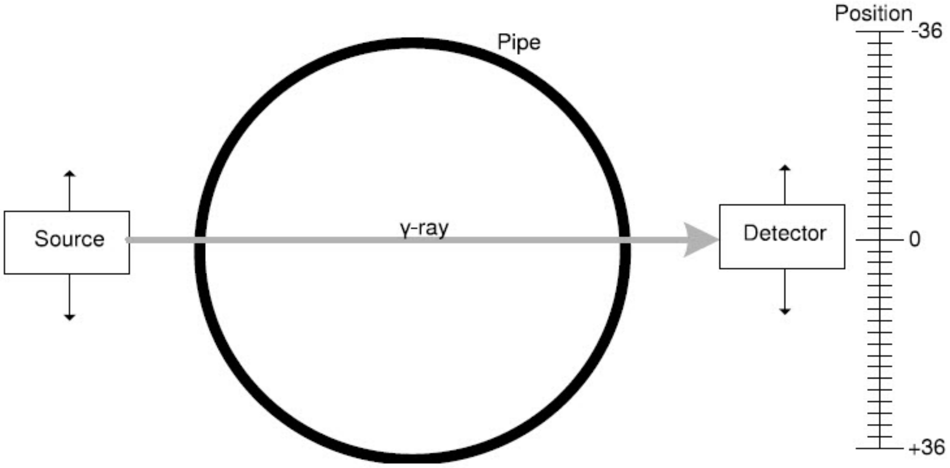

Figure 2.1: Gamma ray attenuation measurement technique [1]

2.1.2 Capacitance Sensor

In [23], a capacitance sensor was discussed for two phase combination of oil-water. The sensor length was 50 cm with an outer diameter of 5.6 cm. The measured capacitance was dependant upon the phase distribution. The same flow pattern was needed for the measurements. This technique was not suitable for water contents greater than 30%. Capacitance sensors were practical for continuous and low conductivity flows.

Experiments were performed using gas-oil two-phase flow in [24] to determine the signal to noise ratio, sensitivity, and time response of the capacitance sensors. Ring type and concave type capacitance electrodes were discussed. The equivalent capacitance circuit for the stratified flow, annular flow, slug flow and bubbly flow were designed. The results showed that the concave-type sensors are less sensitive to the void-fraction signal than the ring type. As the separation distance between the electrodes decreased, the sensitivity of ring type sensor increased. The predicted error was 15% of the experimental data.

A system using capacitance sensor for phase angle conversion was discussed in [25] for the two phase combination of oil-water. The water presence induced a capacitance change that in turn converted into a phase angle. A resolution of 50 ppm of water content was achieved. The diameter of the tube was 1.2 cm with length of 10 cm. The length of each of the two electrode was 9 cm and the minimum spacing between them was 0.4 cm. Water was gradually added in an oil filled pipe through a syringe. For precise control of water, a micro syringe of 50 ppm was used. The 50 ppm of water was translated to a 4.7 fF change in capacitance value. The maximum error between simulation and measurements was 33%. The proposed capacitance sensor details are given in Fig. 2.2.

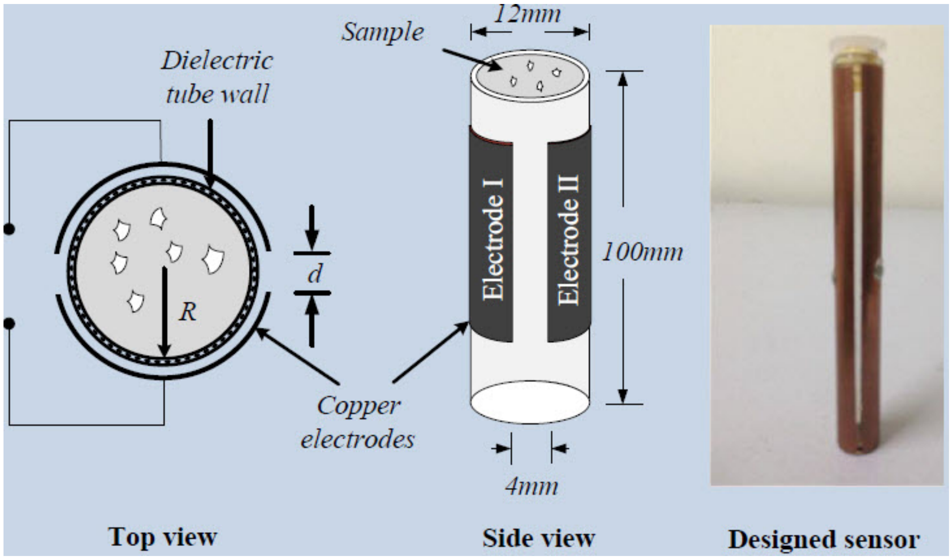

Figure 2.2: Capacitance Sensor [25]

A portable segmented electrical capacitance tomography (ECT) sensor was proposed in [26] which can be placed within any diameter insulating pipeline without the need of redesign. To make the sensor work independently, data acquisition (DAQ) system, microcontroller unit and USB devices were applied. It was based on measuring the dielectric properties inside the material of a closed pipe. This was used for only two phase flow measurements. A sixteen segmented sensor electrode were developed. Each electrode has 10 cm length and 1.9 cm width. The diameter of the acrylic pipe used was 11 cm with the wall thickness 0.5 cm, outer pipe radius 5.5 cm and inner pipe radius 5 cm. The pipeline thickness significantly influenced the reconstructed image and capacitance. The maximum error percentage of the two phase combination mixture of water and gas flow was 17%, palm oil and gas flow 125.9% and water and palm oil flow 33%. A repeatability test was conducted four times for the gas-water combination flow to study the variation and the results showed a consistency in the measurement system. The Portable ECT sensing module is shown in Fig. 2.3.

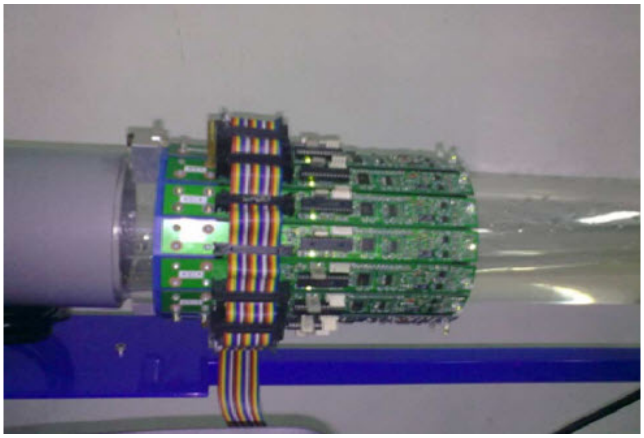

Figure 2.3: Portable ECT sensing module [26]

2.1.3 Microwave Sensor

In [27], a microwave technique was presented. The operating frequency was 10.5 GHz. Electromagnetic (EM) waves that passed through the water were phase shifted and attenuated, but in the case of gas and oil, phase shifted with minor attenuation. The water content of the core was determined by the attenuation of EM waves with an uncertainty less than 5 percent. The phase shift of the EM wave determines the gas and oil with 8 percent error. The experiments were done for both two and three phase oil combinations. This technique used complex and heavy measurement setup for determining the attenuation and phase shift of EM wave.

A microwave technique for detecting the two phase flow of air-water with small water contents was presented in [28]. The operating frequency was between 3.9

GHz to 4 GHz. Using coaxial probe, waveguide modes were excited and reflection response was measured. The length of circular aluminum waveguide was 43 cm with outer diameter of 4.3 cm. The air-water mixture was inhomogeneous during the experimentation. The error percentages were less than 1%. The fabricated microwave sensor is shown in Fig. 2.4.

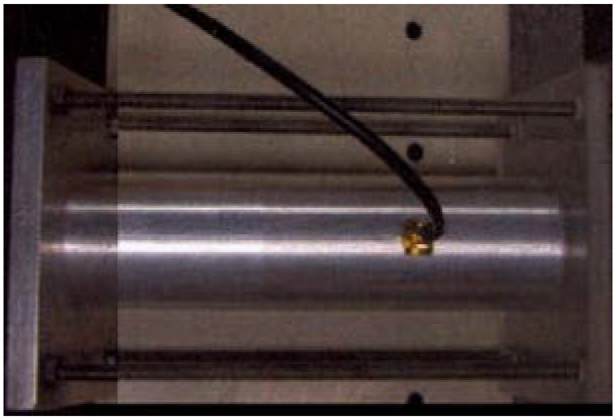

Figure 2.4: Fabricated Microwave sensor [28]

A microwave technique for monitoring fluid level in petroleum pipelines is discussed in [29]. Two patch antennas operating at 3 GHz and 3.3 GHz respectively were designed and integrated within the pipeline. The 3 GHz patch antenna, integrated in the shielded portion was used to measure the air-oil levels. By increasing the oil level in pipeline, the resonance response shift to lower frequencies. The patch antenna operating at 3.3 GHz, integrated in the non-shielded portion was used to measure the oil-water levels. The power level of reflected signal (S_{11}) was changed by changing the water level in pipeline. By increasing the water level in pipeline, the S_{11} increased (matching reduced). For different level of oil and water, look up tables were formulated. Once the contents level of oil and water are known the air level can be formulated easily in case of three phase combination. This technique did not detect water level more than 30% which was the main disadvantage. The pipeline model in HFSS with two integrated patch antennas in shielded and non shielded region is shown in Fig. 2.5. The complex measurement setup is shown in Fig. 2.6.

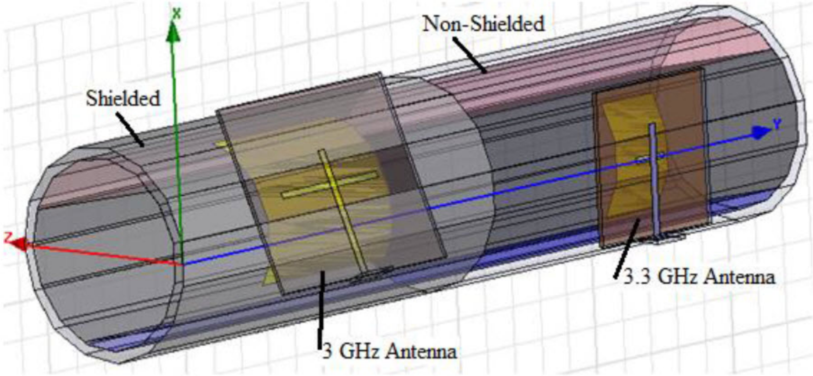

Figure 2.5: Pipeline model in HFSS with two integrated patch antennas in shielded and non shielded region [29]

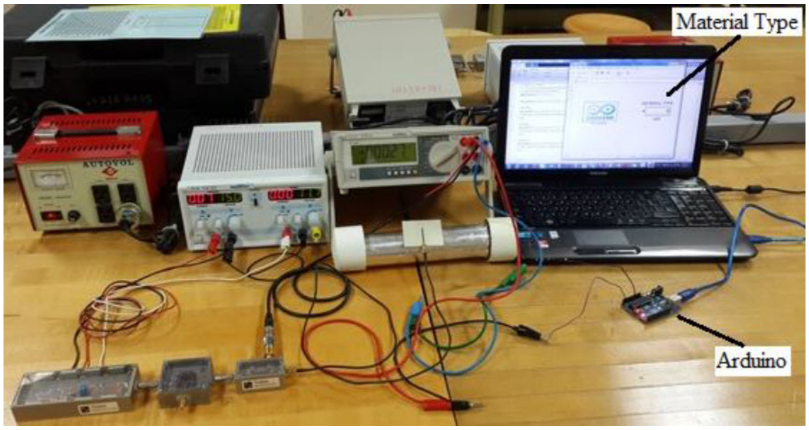

Figure 2.6: Measurement setup in [29]

An invasive microwave sensor was proposed in [30] for detecting water holdup of less than 5% for crude oil in a pipeline. The resonance behavior of hydrocarbon mixture was observed to determine water holdup in horizontal oil pipelines. Increasing the water level in a 2-phase oil-water combination increased the effective dielectric constant and reduce the cutoff response of the pipeline. The maximum error was 1.5%. The measurement unit is shown in Fig. 2.7.

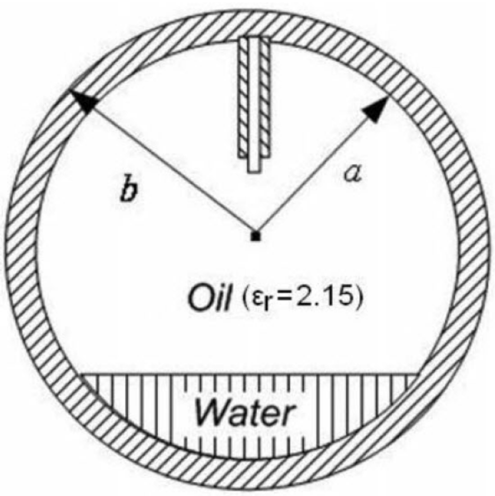

Figure 2.7: Measurement Unit in [30]

2.1.4 Resonant Cavity Sensor

Resonant cavity sensors were discussed in [31-34]. Due to the large difference between permittivity of the water and other fluids, resonant cavity was used in fluid containing water. The frequency shift of the first resonant peak determines the water fraction in a non-intrusive way. In [31], the sensor operating frequency was between 100 MHz to 400 MHz with 1 mW input power. The sensor was designed to resonate at 300 MHz for the TE_{111} resonant mode. The injected electromagnetic signal was received from the sensor through 50 ohm coaxial cables. As a result of increasing the water fraction, the first resonant peak was shifted to a lower frequency and the signal magnitude was improved. The accuracy of the measurements was not discussed. The fabricated resonant cavity sensor with its sketch are shown in Fig. 2.8.

A non-intrusive sensor based on EM cavity for three phase oil combination was discussed in [32]. Using the resonant frequencies shifts, it determines the percentage volumes of each phase of three phases (oil, gas, and water). The dimensions of the cavity were optimized using HFSS. The cavity had an outer radius = 5 cm and depth = 30 cm and a PVC pipeline with an outer radius = 2.5 cm. By increasing the water or oil fraction, the first resonant peak was shifted to lower frequencies and signal magnitude was improved. But in case of oil fraction increment, the frequency shift and increase in signal amplitude were slower than the water fraction case.

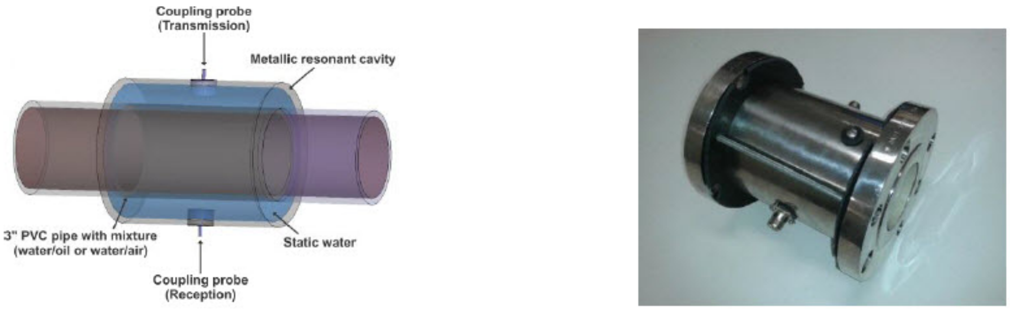

Figure 2.8: Fabricated Resonant Cavity sensor with sketch [31]

A non-intrusive and low input power (10 mW) radio frequencies (RF) sensor operating in the range of 100-350 MHz was discussed in [33]. By increasing the water or oil fraction, the first resonant peak was shifted to a lower frequency. The 0.7 MHz frequency shift was seen for 1% water volume increment. The proposed resonant cavity sensor setup is shown in Fig. 2.9.

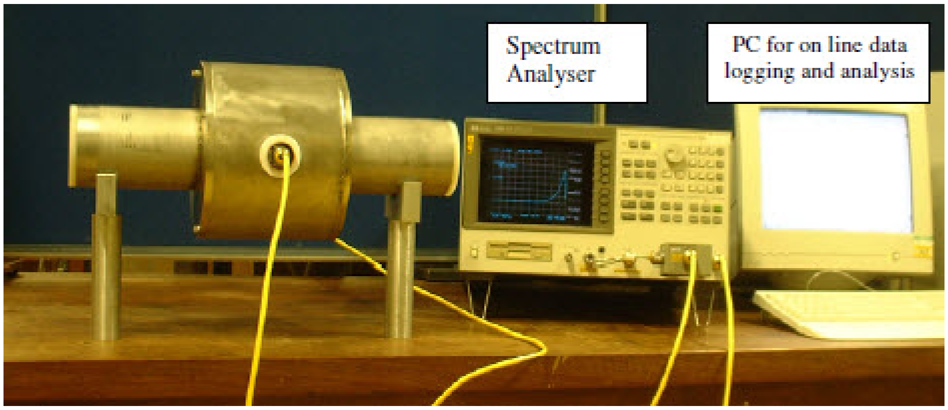

Figure 2.9: Resonant Cavity sensor setup [33]

The operating frequency of resonant cavity sensor in [34] was between 200 MHz to 300 MHz. The size of cavity was $30 \times 10cm^2$. For oil-water combination, 32 MHz shift in frequency was observed by varying water from 0% to 100%. Similarly, for oil-gas, 3.5 MHz frequency shift was seen by varying oil from 0% to 100%. For low ϵ_r values, HFSS simulations had high error percentages.

The electromagnetic signal attenuation by decreasing the water content was the main disadvantage of the RF resonant cavity [35]. This undesirable behavior can be eliminated by using the impedance matching circuit at transmitter and receiver modules. Impedance matching networks based on lumped capacitor and inductor were built for a 100%, 50% and 0% water. The operating frequency range of the cavity was from 150 MHz to 300 MHz. The sensor was built using a 3 inches PVC pipe inside another 5 inches metallic pipe, both of them with 5.9 inches in length. The cavity resonated at 300 MHz for the TE_{111} resonant mode. The detection of first resonant peak was improved using the impedance matching method which contributes to develop more reliable water-cut meters.

2.1.5 X-ray

In [36], an X-ray transmission technique which has its own limitations regarding the number of distinguished substances in relation to the achieved accuracy of the measured attenuation was discussed. This is a non-invasive technique which was done by measuring the attenuation in a pipe with suitable photon energies. As steel pipe walls absorb most of the x-rays, high energy x-ray is required for large penetration. But oil and water has a large difference in absorption which require a low energy x-ray. In oil industry, the energy of x-ray is between 30-60 KeV. The measurement uncertainty includes the statistical error which are due to the counting of the statistics and systematic errors, the x-ray spectrum shape and system response function. To measure the three phase oil volume fraction, two x-ray energies are needed. Thus, raising the system complexity and cost.

The optimum energy for two and three energy sets of x-rays was mentioned in [37] for different oil, gas and water combination. The dual energy gamma ray absorption (DEGRA) and x-ray are the well known techniques in the oil industry for measuring the multiphase flow [38-40]. The conventional single energy x-ray determine the concentration of one material in a certain plane with high accuracy by using long acquisition time. Using two different x-ray energy, we can reconstruct two different tomographies from which the third phase can be calculated [41]. In dual energy x-ray absorption (DEXA), the radiation can be obtained using x-ray generator or a radio nuclear source. By using x-ray generator, we can choose the optimum energy to get good accuracy but in case of radio nuclear source, the energy is restricted by nature. Strict licensing is required for the devices having energy greater than 100 KeV and for the transportation of these radio nuclide sources. The experimentation was done using 4 cm diameter steel pipe. The maximum error percentage was 4.1% for the two phase oil-water combination. The high energy x-ray is not suitable to distinguish between component of the mixture. With the increase in absorption of the mixture, the error at the optimum energy combinations increases.

2.1.6 Dual modality Sensor

In [42], a non-invasive dual-modality sensor was presented by integrating an ECT and ERT sensors. Eight capacitance and eight resistance copper electrodes each with length 10 cm were used. Only simulations were carried out using COMSOL. The ECT mode was active for oil-continuous distribution (water $< 40\%$) and for water-continuous flows (water $> 40\%$), ERT mode was switched. The experiments were done for two and three phase static case only. The dual modality sensor is shown in Fig. 2.10.

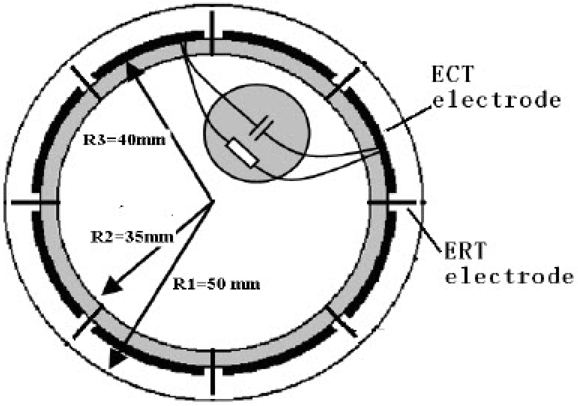

Figure 2.10: Dual modality sensor [42]

A dual modality tomograph (DMT), consisting of gamma-ray and capacitance sensors was developed in [43] for three phase oil combination consisting of oil, water and gas. The problems were the salinity dependence of gamma ray measurement and performance of capacitance sensor in water continuous phase. The capacitance sensor is sensitive to the electrical permittivity of the flow component so it was assume that the liquid contains the oil continuous flow. The gamma ray tomography distinguish the gas from liquid based on density differences in gas and liquid phases and different photon attenuation constants. The capacitance sensor has eight electrodes each with the length of 10 cm. The PVC pipe used was with inner diameter of 8 cm. The capacitance sensor and gamma ray source were at the same cross section of the pipe. The gamma ray source energy was 59.5 KeV. A total of 85 gamma ray detectors were used. There was some calibration issues for the capacitance sensor. The gamma ray and capacitance sensor error increased by changing the salinity of water. The recorded maximum error was 10%.

2.1.7 Electrical Impedance Tomography (EIT) Sensor

A non invasive technique for two or three phase oil combination was discussed in [44]. The prototype consisted of an electrical impedance tomography (EIT) sensor, flow-mixture density meter (FDM) and electromagnetic flow meter (EMF) in addition to pressure, temperature and online water conductivity measurements. Three phase flow optimum performance was achieved within 0-45% gas volume fraction and 45-100% water in liquid ratio (WLR) which results in the estimated WLR within 10% error. For gas volume fraction (GVF) greater than 45%, the WLR error was doubled. For the oil continuous flow with 33% WLR, the obtained uncertainty of GVF was 65% and WLR 25%. So the EIT based system were limited to water continuous flow only. With increasing GVF, the error of oil flow rate increase up to 120%. The error for the two phase flow of oil-water was 5% for only water continuous flow regions. EIT has limited capacity in handling the high fraction of gas and oil phases. The used measurement setup was complex and bulky. The integrated EIT measurement system with its sketch is shown in Fig. 2.11.

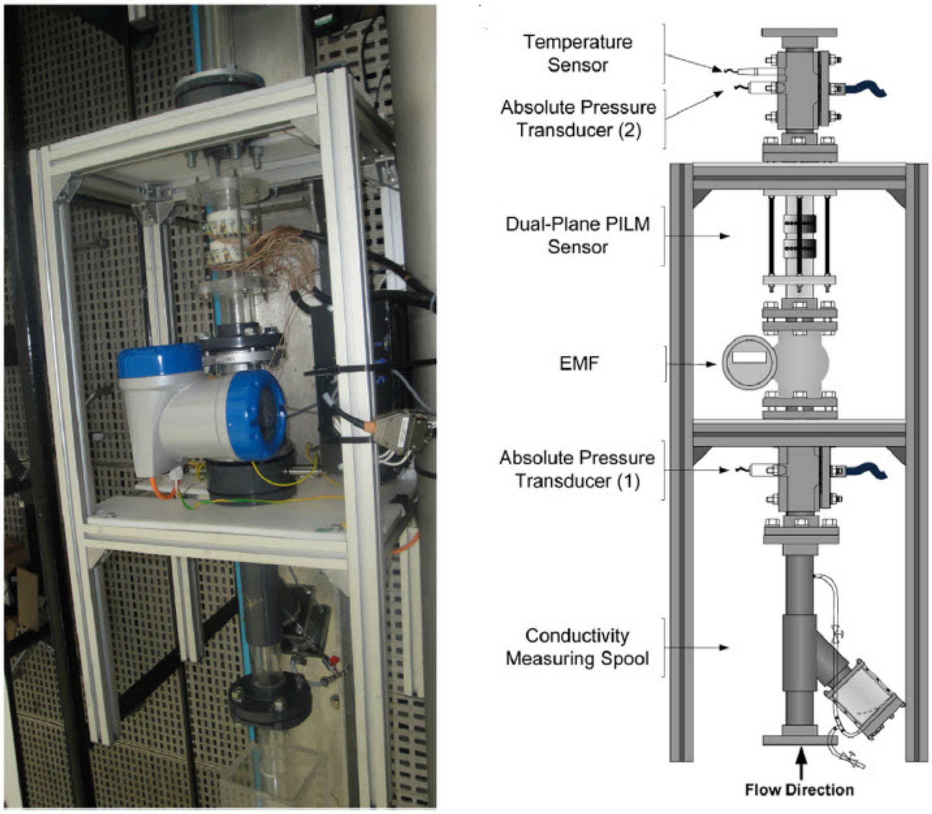

Figure 2.11: Integrated EIT measurement system with sketch [44]

2.1.8 Summary of Previous Multiphase Flow Techniques

The Gamma ray attenuation method in [1] is expensive, need calibration, difficult to implement, limited to high water concentration and have high error percentages without using average linear scaling methods. In [23], the capacitance sensor was discussed for continuous, same flow pattern and low conductivity two phase flows. This sensor was not applicable for water percentage greater than 30%. Only static case simulations were performed for the dual modality sensor in [24]. The length of the electrodes was 10 cm. No comparison was found for the error percentages. The microwave method proposed in [25] had complex and bulky measurement setup. ECT technique used in [26] was only for two phase combination of gas-oil with an error percentage of 15%. This technique cannot be applied for high water concentration mixtures. In [27-30], microwave sensors were discussed which are applicalble for low water contents only. In [31-35], resonant cavity sensors were discussed in which a shift in the first resonance peak gives the idea of the volume fraction of water or oil. Accuracy was not discussed in [31-35]. The resonant cavity first resonance peak is improved using impedance matching network for only three water cuts (0%, 50% and 100%) in [34].

A capacitance to phase angle conversion method was proposed in [35] for only two phase combination of oil-water. The maximum error percentage was 33%. The x-ray attenuation method was discussed in [36-41]. As steel pipes absorb x-rays, high energy x-ray is needed but to differentiate water from oil, low energy x-ray is needed to obtain high accuracy. Also, the radio nuclear source energy is restricted by nature so obtaining high accuracy is difficult. For high energy x-rays, licensing is required. A DMT technique is used in [42]. This technique had some limitations such as, more complexity, calibration issue and oil continuous flow issue for capacitance sensor and increase in error percentage by increasing the salinity of water.

Segmented ECT sensor was proposed in [43]. The measurements were performed for only two phase combinations. The electrode length was 10 cm. The accuracy was influenced by changing the pipe thickness. The maximum error percentages were high, for water-gas 17%, oil-gas 125.9% and for water-oil 33%.

An EIT sensor proposed in [44] was limited to water continuous flow and had the complex and bulky measurement setup. The measurements were restricted to water volume of 45-100% and gas 0-45% for error upto 10%. For 33% water concentration, the recorded error for gas volume fraction was 65% and for water 25%.

A brief comparison of literature survey is given in Table 2.1. A tree of multiphase flow measurement methods is presented in Fig. 2.12.

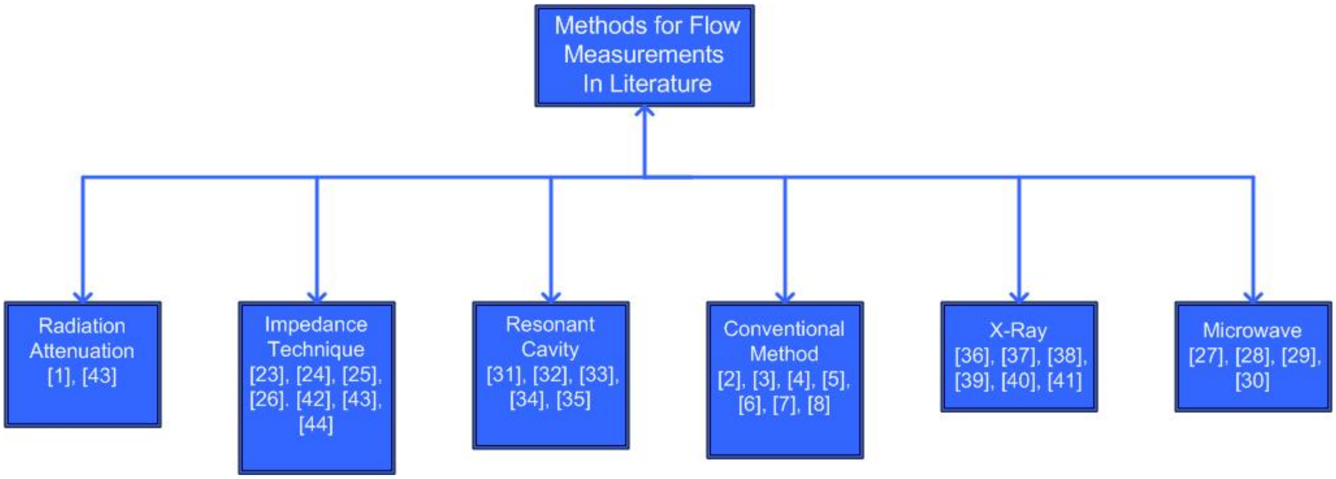

Figure 2.12: Tree of methods for multiphase flow measurements

Table 2.1: Comparision table for literature survey of oil sensor

Reference	Method	Frequency (MHz)	Length (cm)	Complexity	Error (%)	2-phase/ 3-phase	Static/ Dynamic	Cost	Limits
[1]	Gamma Ray	-	large	high	39.2	3-phase	dynamic	very high	difficult to implement, safety aspects, limited to high water concentration
[23]	Capacitance Sensor	-	50	low	-	2-phase	dynamic	low	applicable for continuous oil flows and low conductivity flows, works for water concentration less than 30%, flow regime dependent
[24]	Capacitance Sensor	-	1	low	15	2-phase	dynamic	low	flow regime dependent, not applicable for high water concentration, oil continuous flow needed
[25]	Capacitance Sensor	-	10	high	33	2-phase	static	low	flow regime dependent, not applicable for high water concentration, oil continuous flow needed
[26]	Portable ECT Sensor	-	10	high	33	2-phase	static	high	high accuracy is difficult, not applicable for high water concentration, flow regime dependent, oil continuous flow needed, pipeline material must be pure insulator
[27]	Microwave	10500	17	very high	8	2-phase and 3-phase	static	high	calibration needed, complex and bulky measurement setup
[28]	Microwave	3900-4000	43	high	1	2-phase	static	low	calibration needed, applicable for low water percentages only
[29]	Microwave	3000-3300	2	high	-	2-phase and 3-phase	static	high	applicable for low water percentages (less than 30%) only
[30]	Microwave	2680-2740	-	high	1.5	2-phase	static	low	applicable for low water percentages only, invasive technique
[31]	Resonant Cavity Sensor	100-400	15	high	-	2-phase	static	high	not used for water continuous flow, applicable for non-metallic pipes
[32]	Resonant Cavity Sensor	240-330	30	high	-	3-phase	static	high	not used for water continuous flow, applicable for non-metallic pipes
[33]	Resonant Cavity Sensor	100-350	large	very high	-	3-phase	static and dynamic	high	not used for water continuous flow
[34]	Resonant Cavity Sensor	200-300	30	high	high	2-phase	static	high	not used for water continuous flow, applicable for non-metallic pipes
[35]	Resonant Cavity Sensor	150-300	15	high	-	2-phase	static	high	not used for water continuous flow, applicable for non-metallic pipes
[36-41]	X-Ray	-	-	very high	-	2-phase and 3-phase	static and dynamic	very high	high accuracy is difficult, strict licensing required, health risks
[42]	Dual modality ECT and ERT	-	10	high	-	2-phase and 3-phase	static	high	flow regime dependent, need to switched the ERT mode for water concentration greater than 40%, oil continuous flow needed for ECT
[43]	Gamma Ray and Capacitance Sensor	-	10	very high	10	3-phase	dynamic	very high	calibration and oil continuous flow needed, increase in error with increase in salinity of water, flow regime dependent, applicable for non-metallic pipes
[44]	EIT Sensor	-	large	very high	10	2-phase and 3-phase	dynamic	very high	limited to water continuous flow, bulky measurement setup, limited capacity in handling high fraction of gas and oil, high error percentages for gas and oil (upto 65%), applicable for non-metallic pipes
Proposed	RF Sensor	250	6	low	<10	2-phase and 3-phase	static and dynamic	Low	applicable for non-metallic pipes

2.1.9 Proposed Design Features

Our proposed sensor is designed to operate at 250 MHz for dielectric constant estimation of two or three phase combinations of oil, water and gas which is the first of its kind to give low estimation errors for static and 3-phase flows. The proposed RF sensor has many features. The input power is low (1 mW) so no spectrum licensing is required. It is non-intrusive, non-invasive and compact in size. It is inexpensive and no calibration is required. The installation and maintenance cost is very low. It is simple to implement and install. The RF sensor measurements are taken without effecting the fluid flow. The sensor is robust and can be applicable to any concentration of oil, water and gas in the acrylic pipe. The measurement setup is simple, light and very small in size. It can be used for two or three phase combinations in static or shaked condition. This is applicable for both homogeneous and non-homogeneous flow. There is no need to identify the flow pattern before measurement.

2.2 Biomedical Applications

There are three different types of sensors/antennas for biomedical applications in literature. These are categorized as,

- RF Sensors
- Biomedical Antennas
- E-Fiber Sensors

2.2.1 RF Sensors

For the diagnosis of pulmonary edema, a wearable health monitoring sensor integrated with a body area network was presented in [45]. The sensor consisting of 17 electrodes with 16 ports (planner geometry) was placed on the human chest to measure the effective dielectric permittivity of lungs and detect irregularities. The RF signal of 40 MHz was applied to the active port and scattering parameters are measured on each passive port. The dielectric constant of the lung was expressed as the weighted sum of the measured S-parameters. The permittivity of the lung was calculated with less than 11% error from the exact value. The mobile sensing body area network (MS-BAN) was employed for wireless data transfer and continuous remote sensing. To test the robustness of the sensor, the volumetric percentages of blood, air and tissues were taken for normal, edema and emphysema conditions of the lungs. The effective dielectric constant, conductivity and loss tangent were calculated in each case. The error remained below 10% between exact and calculated dielectric constant values for all cases.

The use of tissue emulating gel was done to better emulate the human tissue. The semi solid gel based phantom was chosen for the measurements due to ease in fabrication and low cost. Skin and muscle gel was created using the formula in [46-47]. The S_{i1} parameters were measured on each port sequentially. The data collection procedure was repeated twice for good accuracy. To detect pulmonary edema stages, hollow plastic balls filled with distilled water were inserted inside a swine lung. The process was repeated with increments of six water balls which were placed in the strongest fringing field area. The measured error was maintained below 11%. The proposed RF sensor in [45] is shown in Fig. 2.13.

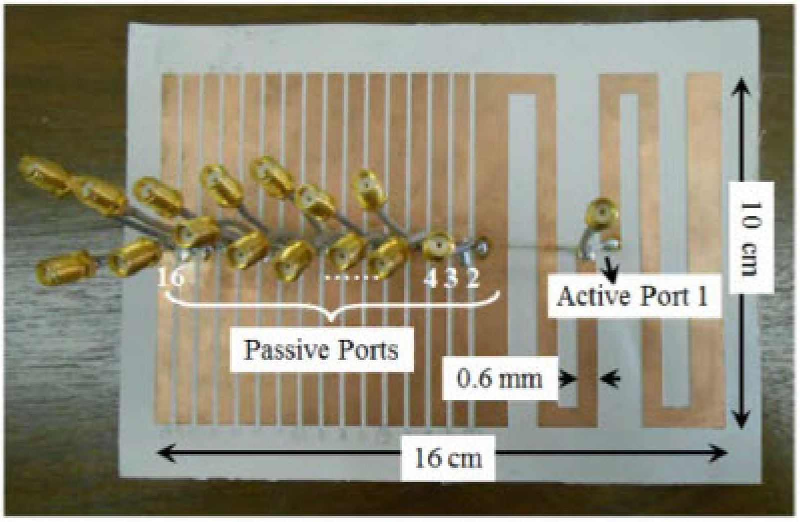

Figure 2.13: Proposed RF sensor in [45]

Edema and emphysema diseases were characterized by the modified permittivity and conductivity of lung tissue due to the change in the total lung water content in [48]. To detect the radio graphic changes using conventional chest x-ray, doubling the lung water is necessary. But the microwave method provides more absorbed energy when increasing the water content. Both reflection and transmission coefficients through the lungs are sensitive to the change in water content. The lung is composed of tissue, air and blood volume. The blood volume will decrease with emphysema and increase with edema. The tissue volume of lungs was 500 ml in normal case, 250 ml in emphysema and 1000 ml in edema case. The normal residual volume was 1630 ml which will decrease to 1130 ml in edema and double in case of emphysema. The operating frequency was 915 MHz. In the frequency range of 0.1 to 3 GHz, the equations for electrical properties of blood muscles and fat were provided. The error percentages were not discussed.

Breathing, heart rate and changes in lung water contents were monitored using a single transmission coefficient using short time Fourier transform based digital signal processing method in [49]. The sensor operating frequency was 915 MHz which is the unlicensed band for medical applications. FEKO simulation software was used to optimize the design. An air pump connected with balloon was used to simulate breathing. Two sponge layers were placed on both sides of the balloon. To emulate changes in lung water contents, water was injected in the sponge layer through a syringe. Breathing has an effect of 4 degree peak to peak change in the measured microwave phase and 46 degree with the addition of 10cc water. The microwave applicator with its fabricated prototype in [49] are shown in Fig. 2.14.

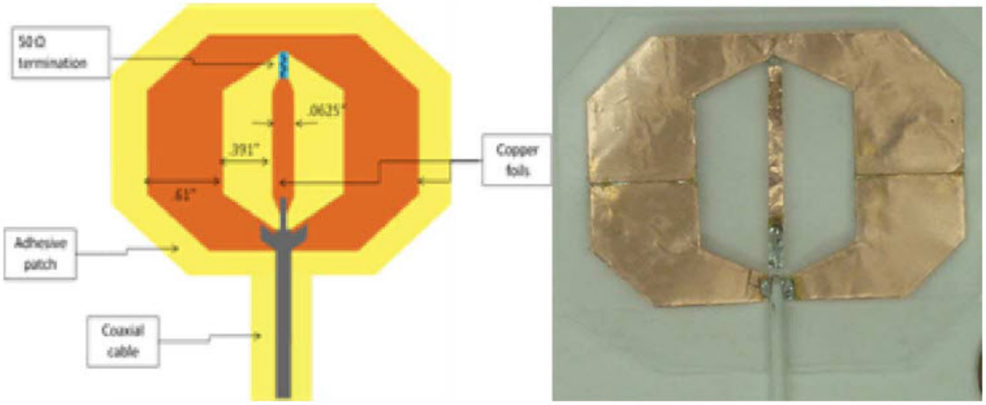

Figure 2.14: Microwave applicator with fabricated prototype in [49]

A mobile wearable health sensor was proposed in [50] for early detection of cancer and pulmonary edema. The operating frequency of the sensor was in 10 to 40 MHz range. This was a wrapped around chest sensor with errors less than 8%. The subgrouping of sensor ports makes post processing of the data difficult.

Edema can be detected with single sensor at 915 MHz using reflection and transmission phases in [51]. The size of sensor was $3.2 \times 3.4 cm^2$. It is not flexible and wearable. The accuracy was not discussed.

The RF sensor in [52] was a wrap around belt worn under the clothing. The operating frequency was 40 MHz. The error percentage was below 11%. The sensor served as a precursor to congestive heart failure (CHF).

A sensor operating at 40 MHz was used to provide pixel by pixel imaging for deep tissues in [53]. A 16-pixel image was retrieved with an errors better than 6%. This is an alternative to the conventional imaging techniques, use for cardiovascular diseases and tumor growth monitoring. This method is not affected by fat, skin or muscle thickness. The human torso was modeled as a two layer cylinder of 18 cm radius with 15 cm radius of the enclosing one. For simplicity, fat, skin, muscles and bones were modeled as a single outer layer. The imaging domain was divided into K=16 pixels with uniform square grid $7.5 \times 7.5 cm^2$ in size. The input power at the source was 1mW. According to IEEE and FCC safety exposure guideline, the 1g of tissue SAR limit should not exceed 1.6 W/kg. ANSYS HFSS was used for the simulations. The sensor had 24 probes and 400 different combination of tissues during training phase. The probes of sensors were dipole like with 5.3 cm in length and all were matched with 50 ohms. The electrical properties of human tissues were also given. The cross sectional view of the torso after pixelization in [53] is shown in Fig. 2.15.

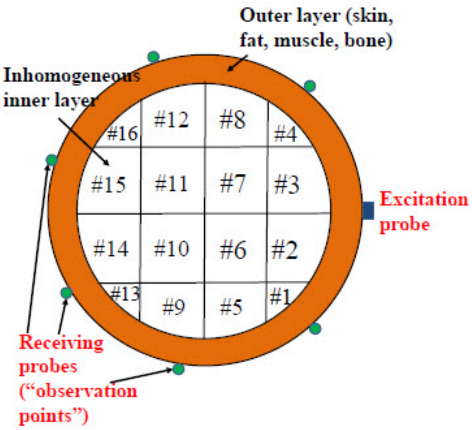

Figure 2.15: Cross sectional view of the torso after pixelization in [53]

The proposed wrapped around sensor in [54] was operated at 40 MHz and provided 16 pixel images with an error better than 5%. This can be used for tumor growth monitoring and prevention of cardiovascular diseases. From the body surroundings, the 16 probes collect the scattered electric field.

The diseases of cancer and pulmonary edema has unique permittivity for the organs of interest. The wrapped around sensor in [55] can detect the early stages of pulmonary edema. One port was selectively excited with 10 to 40 MHz RF signal and other receive the fringing fields. A transmission coefficient of -50 dB was considered above noise level and compatible with regular signal transmission. The measured error was less than 8%. The sensor allow high resolution images of organs of interest which provides another way to study the organs of interest.

The traditional X-ray method locate the tumor location. It cannot verify whether the tumor is malignant or benign. To determine the masses in human body, the sensor first port was excited with 10 MHz in [56]. The 16 port difference level of 14 dB between high and low dielectric constant gave a good resolution in extracting the dielectric constant. The length of the electrodes were important but their width did not effect the performance. The spacing and size of the active electrode was also important. Each electrode was 10 cm long and 0.5 cm wide. As the matching improved, the sensitivity was improved from 14 dB to 22 dB.

The pixel by pixel image of the internal organs dielectric properties was obtained using an RF sensor operating at 40 MHz with errors as high as 6.75% in [57]. The sensor can penetrate deep up to 10 cm and the theoretical error was less than 2%. The body cross section was divided into pixels. For each pixel , a linear equation was used to estimate each pixel permittivity based on the collected S-parameters measurements. To retrieve the image on a user cell phone, a body area network was designed.

In [58], the proposed RF sensor consisted of N electrodes (antennas) fed by (N-1) ports. The first port was excited by 40MHz RF signal (at industrial, scientific and medical (ISM) radio band). The remaining (N-1) passive ports receive radiated fringing field propagated through tissues. The amplitude of S-parameters was measured between sensor ports. The proposed RF sensor had 16 cm width and 10 cm length. As the number of probes within the size increase, the dynamic range increased but port S-parameter value decreased which was undesirable. So, the suitable choice was the 17 electrodes. The field was confined between first two electrodes including feeding due to impedance mismatch. To improve the matching, non-uniform spaced probes were presented. The design provides 22 dB dynamic range by varying dielectric constant from 1 to 180. The colleected S-parameters resultant equation was solved using LS method. Then, an equation was designed to estimate the dielectric constant. The measurements were applied to mannequin filled with dielectric to emulate the human body. At the beginning, the data was collected with nine electrode sensor using empty mannequin and then filled with liquid having 56 dielectric constant. The maximum error between the calculated and exact values of dielectric constant remained 6.8%. In the second step, the 17 probe lung sensor was used. The dielectric constant was extracted in the presence of outer layers (ground beef or steak) and considering the inner layers (distilled water, ground beef, ground beef with air bubbles) with the goal to accurately extract the dielectric constant. A foam block was used to represent air volume within the lung. For different sizes of foam block the dielectric constant was calculated with maximum error of 7.62%.

A wearable wrapped around sensor was presented in [59]. The sensor was flexible and can monitor the inner tissues of human body deep up to 8 cm. The sensor had 66 electrodes and 65 ports. The size of sensor was $5 \times 83 cm^2$. The sensor was divided into six subgroups each with 11 ports. The dielectric constant of each subgroup was estimated using the LS method. The maximum error percentage was 13.5%. The RF sensor in [59] is shown in Fig 2.16.

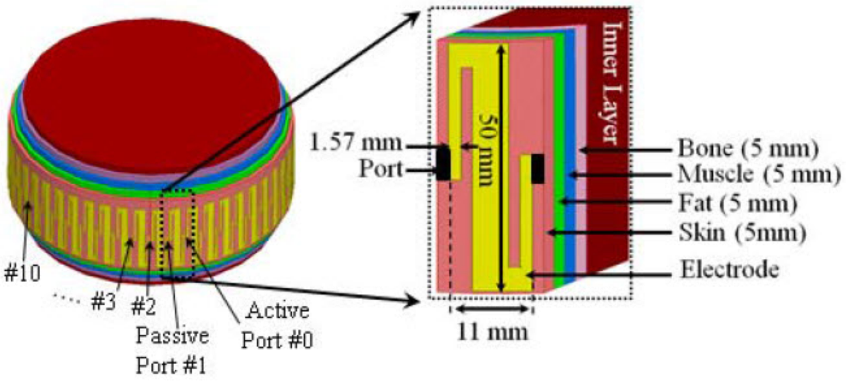

Figure 2.16: RF Sensor in [59]

A pathway to transfer sensor health informatics data to mobile device or remote database server was discussed in [60]. The sensor collect vital signal from body, digitize them using on board processor then transfer it to the wireless transceiver using Zigbee protocol. A bluetooth bridge was used between Wi-Fi and sensor transponder for wireless data link. An Android application was developed to present receive data into a user friendly formate. Then, the data was transfered to a PHP based cloud database via 3G/4G or Wi-Fi networks which was accessible to physicians to take appropriate action. The wireless communication system for remote medical monitoring in [60] is shown in Fig. 2.17.

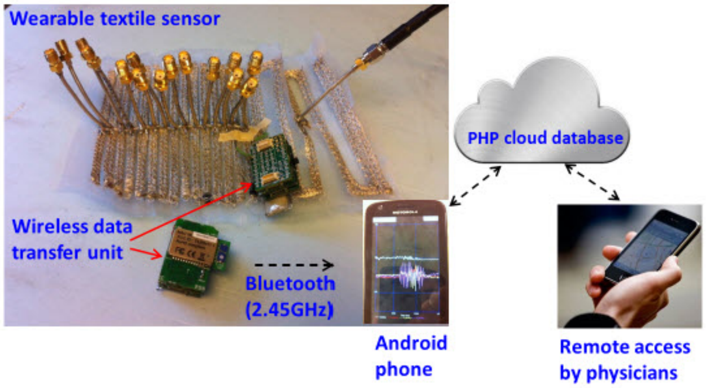

Figure 2.17: Wireless communication system for remote medical monitoring in [60]

The Medical Sensing Body Area Networks (MS-BAN) in [61] were attractive for aged people to reduce health care cost and enable independent living. Their integration with health monitoring applications is the main challenge. The RF signal was converted into DC using LT5537 chip and then send to low power processing unit for digitization. The digital signal was transmitted through low power Class 2 Bluetooth radio for communication with laptop or mobile devices using Android application. The LT5537 chip can detect RF power level as low as -80 dBm. The lung sensor was used to provide carefree and reliable communication even if a person is sleeping or exercising.

2.2.2 Biomedical Antennas

The antenna in [62] was used to detect fluid accumulation in lungs which is the indication of heart failure. The operating frequency was 900 MHz with dimensions of $9.7 \times 5.8cm^2$. It is not flexible or wearable. The accuracy is not discussed.

The main symptom of CHF is the fluid accumulation inside the lungs which is known as cardiac pulmonary edema. The collected data from the scanning of wide band folded antenna was visualized in time domain using the inverse Fourier transform in [63]. These images showed the reflected signal intensity from different parts of the torso. The pressure of blood vessels near the lungs increases when heart fails to supply enough blood. This phenomena results in the leakage of blood into the air sacs of the lungs. The lungs capillaries pressure increases due to accumulation of blood which results in the leakage of fluid inside the lung. This is known as cardiac pulmonary edema. The frequency of operation was 0.77 to 1 GHz. The antenna dimensions were $14 \times 14 \times 0.08 cm^3$. The used phantom had chest circumference of 94 cm with the dimension $43 \times 40 \times 48 cm^3$. It includes ribs, fat, lungs, abdomen and heart. The bones and soft tissue were fabricated using epoxy resin and polyurethane respectively. The SAR was calculated using HFSS. The lowest possible detected water inside the lungs was 4 ml using this system which was the early stage of CHF. The designed heart failure detection system in [63] is shown in Fig. 2.18.

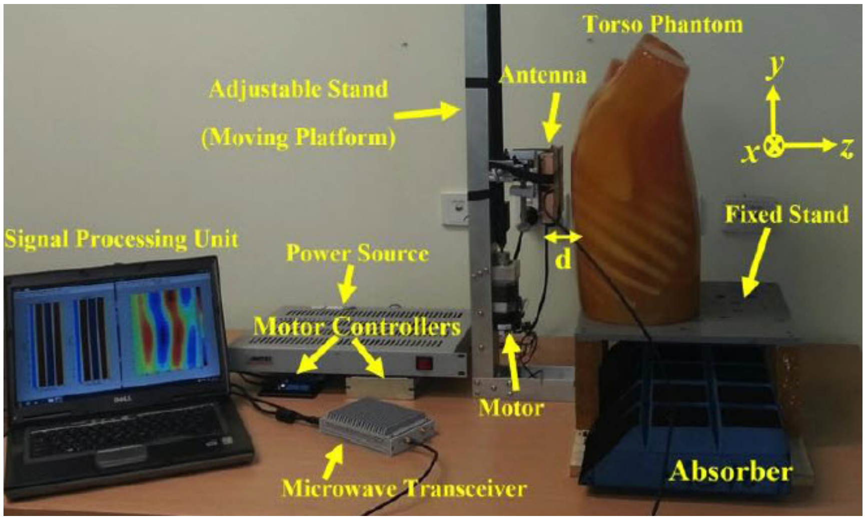

Figure 2.18: Designed heart failure detection system in [63]

Antennas can directly be stitched to garments or integrated into personal accessories like glasses, shoes, helmet and button as discussed in [64]. The moisture absorption and mechanical deformation results in performance degradation of textile antennas. A reflector can be used in antenna topology to reduce SAR and increase the antenna gain. The design of flexible, light weight and conformable body worn antennas is challenging in lower frequency range. The human body have high dielectric permittivity and behaves as inhomogeneous lossy antenna platform.

An implantable PIFA was designed with an operating medical implant communication service (MICS) band of 402-405 MHz in [22]. The high frequency structural simulator (HFSS) based on finite element method (FEM) with ANSYS optimetrics and high-performance computing (HPC) features was used for simulation. The implantable antennas require low power, small size and impedance matching. The ANSYS human body model is very large which makes the simulation very complex and time consuming. The dimension of antenna was $2.0 \times 2.4cm^2$.

Miniaturization techniques of biomedical antennas were discussed in [65]. CMOS technology enable the miniaturization of implantable device to operate at low frequencies. A high permittivity substrate shifts the resonance frequency to lower frequencies. Using the PIFA structure, the antenna size will be reduced. Using meandered line will increase the current path of radiator and reduce the antenna size. Inductive or capacitive loading can be used for impedance matching. High operating frequency will reduce the antenna size but have some health aspects.

The sensor was a balanced antipodal Vivaldi antenna working in the frequency range of 1.5 to 6.5 GHz for lung water monitoring in [66]. The lung water volume was varied from 0 to 900ml. Reflected signals were used to estimate the lung water level. The relative error was less than 6%. The simulations were performed in full wave electromagnetic numerical simulator SEMCAD X. The considered lung water volume were 0, 250, 520, 600 and 900 ml. The time delay between water free and water inserted lung signal was calculated. The sensor can also measure the respiration and heart beat parameters using the Doppler effect.

A flexible inkjet printed on fabric antenna was proposed in [67] with an operating frequency of 2.45 GHz. Due to less surface roughness, high polyester fabric (85% polyester and 15% cotton), "Luminex 310" was used in experimentations. The size of the antenna was $3 \times 3cm^2$. The substrate thickness was 1 mm (0.5 mm fabric and 0.5 mm interface layer). The dielectric properties of the substrate were calculated using an Agilent impedance analyzer. The permittivity of the substrate was 2.58 with loss tangent 0.048 at 1 GHz. As the substrate was non-dispersive, the same electrical properties can be applied at 2.45 GHz. No significant degradation was observed by using the antenna original shape after multiple bends. The bending of the antenna printed on fabric in [67] is shown in Fig. 2.19.

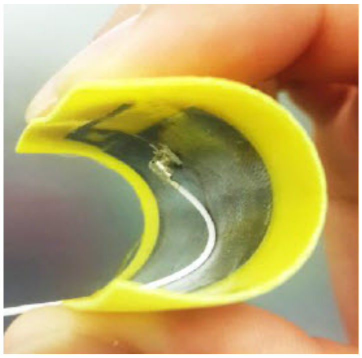

Figure 2.19: Bending of antenna printed on fabric in [67]

Wearable antennas raises the question of health hazard effects on the wearer body. The ratio between transfered power and the mass of body where the SAR values are evaluated is called the Specific Absorption Rate (SAR). The SAR values of dipole antenna is higher due to no ground plane structure as discussed in [68]. The presences of ground plane introduces additional shielding between the antenna and human body which reduces the EM radiation inside the human tissues and therefore reduce the SAR.

A non- invasive portable system was proposed for pulmonary edema monitoring in [69]. The impedance of the internal tissues was measured by applying a small amplitude of currents into the body and receiving the developed electrical potential.

An ultra wide band antenna was proposed on jeans substrate (99% cotton) for medical wearable applications in [70] with a bandwidth of 13.08 GHz. As the textile materials had low dielectric constant, antenna surface wave loss reduced and impedance bandwidth improved. The conductive part was a copper fabric. The size of the antenna was $6 \times 6 \times 0.3cm^3$. The operating frequency was 8.86 GHz to 21.94 GHz. The medical monitoring was done at 9.7 GHz. As the antenna was directional, it was a good option for military wearable applications. The proposed antenna in [70] is shown in Fig. 2.20.

(a)Front Face (b) Back Face

Figure 2.20: Proposed antenna on textile substrat in [70]

A wearable textile antenna was proposed in [71] covering 2G, 3G and 4G system with a bandwidth of 2.7 GHz. The resonance frequency is 2.12 GHz with the impedance bandwidth of 1.8 to 3.2 GHz. A low cost jeans textile substrate was used with permittivity of 2.14 and loss tangent 0.082. The size of antenna was $7 \times 5 \times 0.12cm^3$. By placing the antenna on hand, 13.68% difference in resonance frequency was observed and placing on head, 72.96% difference in bandwidth was observed. The proposed antenna in [71] is shown in Fig. 2.21.

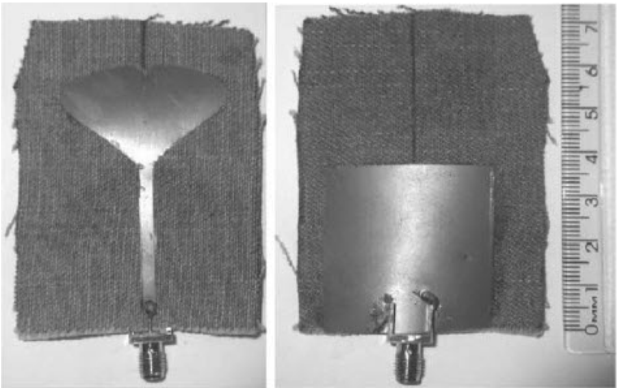

Figure 2.21: Proposed antenna on textile substrat in [71]

2.2.3 E-Fiber sensors

Pulmonary edema is linked with kidney disease and CHF. So early detection of lungs abnormalities is a key aspect. The sensor in [72] was fabricated using conductive textile to integrate it on daily garments. The 16 port sensor operating frequency was 40 MHz. The water balls were inserted to emulate the stages of edema. Pig's lung was used for testing within two hours of slaughter. Tissue emulating gel were also used to mimic skin and muscle layers. The Zig-bee protocol was used to transfer sensor data to transponder which was displayed in android application. The data was then transfered to a cloud server via 3G/4G or Wi-Fi networks for doctor access. A wireless system was individually connected to each output port. A DC converting circuit was also used for RF to DC conversion. This sensor can be used to monitor the permittivity of a single organ of interest only.

The e-fiber is composite of flexible and high strength polymers. The proposed e-fiber were each of 15 um grouped together to improve their conductivity in

[73]. E-fiber has both electrical and mechanical advantages. It is more durable and robust than printed antennas. Computerized embroidery process was used to sew the e-fibers on textiles. The proposed sensor designs were translated into embroidery software. The sewing machine carries out each digitized stitch so that the e-fiber is precisely placed on the textile. The physical discontinuities and gaps were eliminated by double layer embroidery which also improve the surface conductivity. A low loss polydimethylsiloxane (PDMS) substrate was used with dielectric constant of 3 and loss tangent$<$0.01. The designed antenna maintained its performance after 20 times flexing and several times washing. The continuous monitoring of patient in rest, active and sleep state was done using RF e-fiber sensor operating at 40 MHz. It can be integrated as parts of garments. The sensor with large surface area can penetrate deep. The sensor had 16 ports of 10cm in length and 1 cm in width. With the comparison of copper sensor some discrepancies were observed due to inaccuracies in the fabricated textile sensor. The e-fiber version had an insertion loss of 0.07 dB/cm at 1 GHz and 0.15 dB/cm at 2 GHz while copper version had an insertion loss of 0.02 dB/cm at 1 GHz and 0.05 dB/cm at 2 GHz. The textile sensor in [73] is shown in Fig. 2.22.

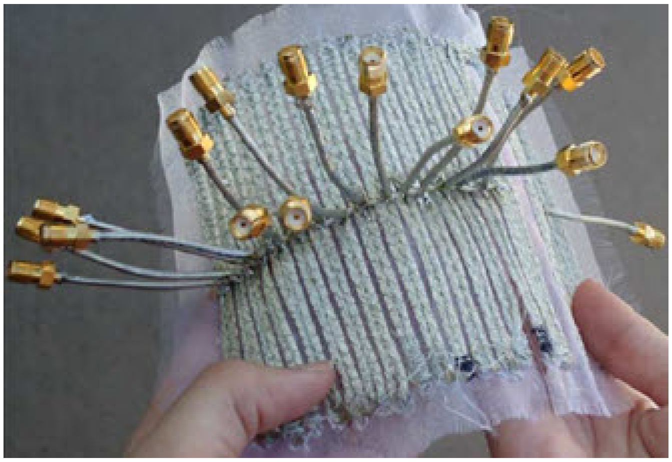

Figure 2.22: Textile sensor in [73]

The designed colorful textile antennas can be embroidered into different shapes and logos. The colorful shape can be generated on the front side of garments. Copper made logo antennas are not suitable for body worn applications. The proposed technology in [74] can build flexible, colorful, low conductor loss, light weight, mechanically robust textile antennas with a precision accuracy of 0.1 mm. The antenna design was completed in four steps, antenna design, digitization, embroidery of conductive part and embroidery of non conductive part. The non-conductive threads were employed to secure the e-threads on fabric. The non-conductive threads were acting like free space and did not effect the antenna performance. The antenna conductive part should not touch the skin directly as it is also conductive which will short circuit the antenna. These textile antennas are lightweight, flexible and mechanically robust and withstand the repetitive washing/drying and daily wear.

Conformal flexible structure including metallic composite as conductor, fabrics and elastic polymer as substrate were discussed in [75]. The reported conductive materials in literature have high material loss and mostly suitable for low frequency applications. Composite metal coated fibers are preferred at microwave frequencies due to their high mechanical strength and low material losses. The double stitching was used to improve conductivity. To avoid shortening between the electrodes, the embroidery should be carefully done. E-fibers are preferred in forming inter connectors in 3D circuits due to their flexibility and continuity. Current challenges includes the integration of standard circuit components with e-fiber, high density e-fiber fabrication onto the daily garments and their adaption into established industry manufacturing process.

By employing very thin 7-filament Elektrisola E-thread, the authors of [76] achieved 24 time low fabrication cost, three times high geometrical precision, good RF performance and 50% less fabrication time compared to latest embroidery approach. The CAD file of design was exported to a Brother embroidery software tool-set. The file is then converted into digitized stitching patterns. Using programmable sewing machine, the automated embroidery process was done. 7-filament silver plated copper Elektrisola E-threads of 0.12 mm in diameter was realized as conductive textile surfaces. The PDMS substrate of thickness 1.5 mm, dielectric constant 3 and loss tangent$<$0.01 was used.

Colorful wearable antennas can be integrated into logos and aesthetic shapes as discussed in [77]. Due to high mechanical strength and low losses, e-threads are preferred for RF applications. The employed e-threads consist of 7 to 664 metal coated polymer filaments each of 15 um thick. The geometrical precision was 0.1 mm. The PDMS substrate with dielectric constant 3 and loss tangent<0.02 was used. The colorful shape of the antenna appears in the front side of garments. The freely available RF energy was harvested in an office environment using 2.45 GHz WLAN band which was converted into usable power. This system eliminate the inconvenience of repetitive charging and extend the battery life. The textile sensor in [77] is shown in Fig. 2.23.

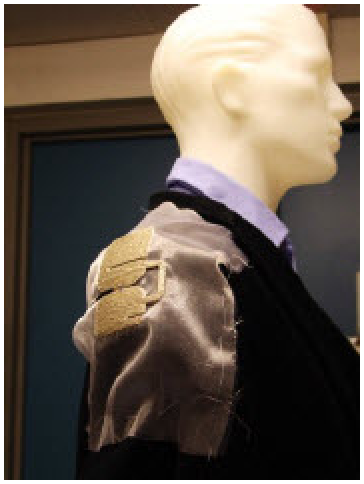

Figure 2.23: Textile sensor in [77]

A microwave textile Electromagnetic (EM) coupler was proposed in [78] for monitoring changes in lungs water content and vital signs. For the EM wave coupler design, three types of conductive textile materials, including woven copper fabric, 2-ply steel thread and knitted silver-plated fabric were used to see which one was the best among them. The EM coupler consisted of two sensors and the operating frequency was 915 MHz. The size of EM coupler was $4 \times 24cm^2$. The measured S_{21} range was -54 dB to -55 dB for normal lung and -56 dB to -58 dB for edema lung. A 1.6^o change in phase of S_{21} was observed for the change of 1% in lung water contents. The proposed antenna with different conductive textile materials is shown in Fig. 2.24. The heart beat and respiration waveforms were extracted as shown in Fig. 2.25. During the breathing, the amplitude of S_{21} vary from 10^o to 15^o and during the breath hold, the heartbeat waveform vary from 1^o to 3^o. The steel thread textile EM coupler provided the high sensitivity to detect vital signs with a 1% change in lung water content.

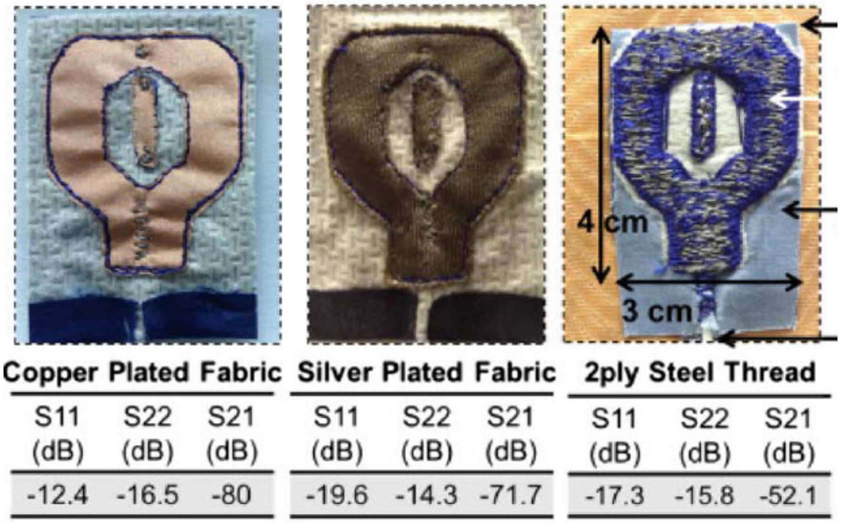

Copper Plated Fabric			Silver Plated Fabric			2ply Steel Thread		
S11 (dB)	S22 (dB)	S21 (dB)	S11 (dB)	S22 (dB)	S21 (dB)	S11 (dB)	S22 (dB)	S21 (dB)
-12.4	-16.5	-80	-19.6	-14.3	-71.7	-17.3	-15.8	-52.1

Figure 2.24: Proposed antenna with different conductive textile materials in [78]

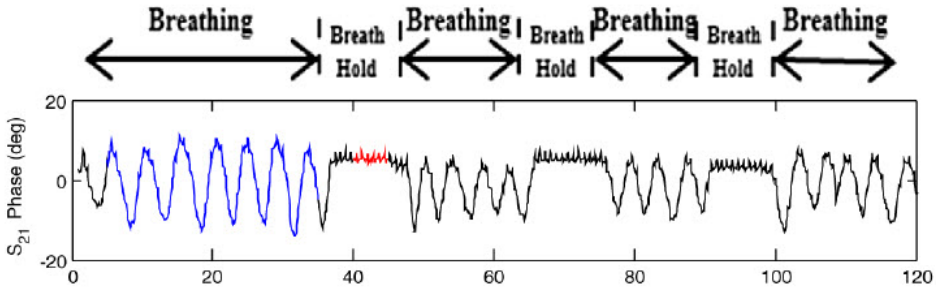

Figure 2.25: Heart beat and respiration waveforms in [78]

A brief literature survey comparison table is shown in Table 2.2 and Table 2.3 highlighting the features of prior works and our proposed one. A tree of literature survey on biomedical sensor and antennas is shown in Fig. 2.26.

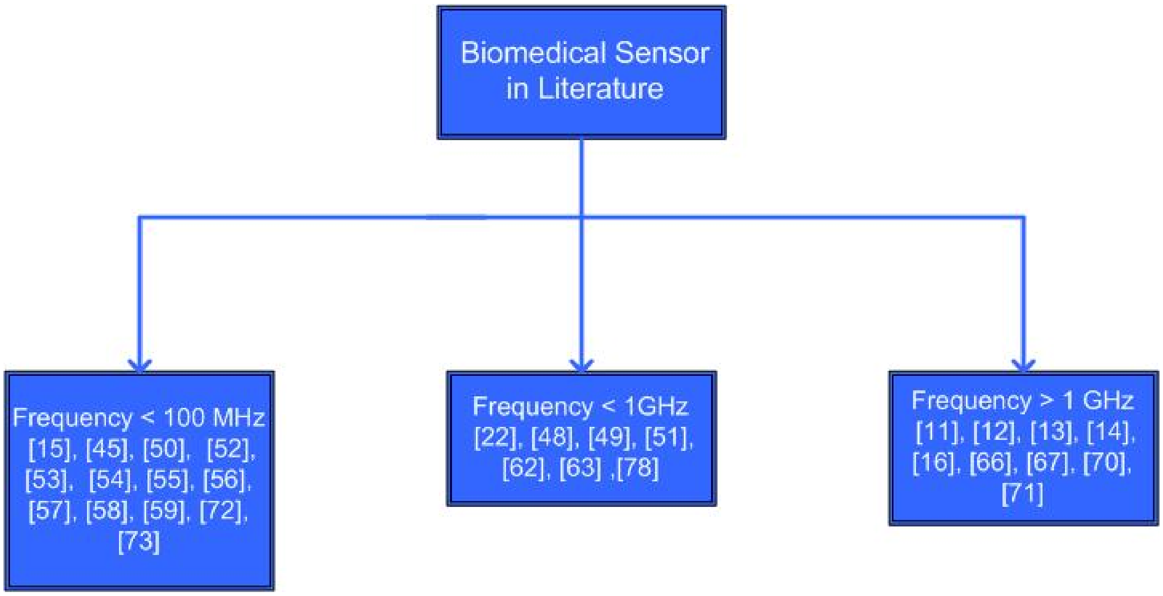

Figure 2.26: A tree of literature survey on biomedical sensors

2.2.4 Proposed Biomedical Design Features

Compared to literature in Table 2.2 and 2.3, our proposed biomedical RF sensor has many features. The input power is low (1 mW) so no spectrum licensing is required. It is non-intrusive, non-invasive and compact in size. It is inexpensive and simple to implement. The sensor is wrapped on an elliptical chest model in its modeling and during measurements which represents an actual scenario unlike all other that use cylinders. The sensor is robust and can be integrated within clothes/T-shirts. It can estimate different lung diseases with the lowest measured error percentages compared to all previous works. It can monitor the inner tissues deep upto 11.64 cm. A single sensor array covers the whole area of an average adult chest, no sensor subgrouping is required. The length of the electrodes is the smallest in its frequency range (4 cm at 60 MHz) and used to cover 18.29 cm of height. The achieved dynamic range between low and high ϵ_r values is 20 dB. The real time ϵ_r measurements are used for the experiments using dielectric assessment kit. Both homogeneous and non-homogeneous experimental cases are discussed unlike most previous works. The drawback of the proposed sensor is the mechanical deformation of the sensor after washing the T-shirt/clothes.

Table 2.2: Comparision table for literature survey of biomedical sensor

Reference	Category	Application	Frequency (MHz)	Size (cm)	Complexity	Error (%)	Cost	Limits
[10]	fabric sensor using advance signal precessing techniques	cardiovascular diseases	-	large	high	-	very high	limited for monitoring breathing, heart rate and skin temperature, advance in data collection but lack in deep tissue monitoring
[11-14]	EIT	real time imaging of ventilation,detection of collapsed lung	1 to 20000	very large	high	high	very High	limited to bed side application due to complex circuitry for generation of variable current patterns
[15]	Ultrasound impedance tomography	abdominal, cardiac, urological, fetal, pediatric and fluid detection measurement and analysis	(1-20)	very large	high	high	very high	portable but not wearable
[16]	Microwave imaging	breast cancer detection and treatment response monitoring	300 to 30000	small	high	high	low	small depth of penetration, portability and wearablity is not possible due to complex circuitry
[45]	RF Sensor	pulmonary edema monitoring	40	10×16	low	11	low	monitor the permittivity of a single organ only
[48]	Microwave reflection and transmission measurements	pulmonary diagnosis and monitoring	915	very large	very high	-	high	health risks due to high frequency operation, not wearable
[49]	Microwave sensor	breathing, heart rate and changes in lungs water contents	915	-	very high	-	low	health risks due to high frequency operation, not wearable, short time Fourier transform based digital signal processing makes it more complex
[50]	RF sensor	early detection of cancer and pulmonary edema	10-40	-	high	8	low	subgrouping of the sensor makes post processing of the data difficult
[51]	Microwave sensor	pulmonary edema detection	915	3.2×3.4	low	-	low	not flexible, health risks due to high frequency operation, not wearable, accuracy was not discussed
[52]	RF sensor	served as a precursor to congestive heart failure	40	-	high	11	low	subgrouping of the sensor makes post processing of the data difficult
[53]	RF Sensor with pixel by pixel imaging	cardiovascular diseases and tumor growth monitoring	40	5.3 × 113	high	6	low	experimental verification was not done
[54]	RF Sensor with 16 pixel imaging	tumor growth monitoring and prevention of cardiovascular diseases	40	-	high	5	low	experimental verification was not done
[55]	RF Sensor	cancer and pulmonary edema	10 to 40	-	high	8	low	experimental verification was not done
[56]	RF Sensor	to determining the Relative Permittivity of Masses in the human body	10	10 × 16.1	low	-	low	experimental verification was not done, monitor the permittivity of a single organ only
[57]	RF Sensor with pixel by pixel imaging	wearable real-time monitoring system	40	-	high	6.75	low	subgrouping of the sensor makes post processing of the data difficult
[58]	RF sensor	lungs dielectric properties	40	10×16	low	8	low	monitor the permittivity of a single organ only
[59]	Flexible RF sensor	monitoring deep tissues electrical properties	40	5 × 83	high	13.5	low	subgrouping of the sensor makes post processing of the data difficult
[22]	Implantable PIFA	biomedical telemetry	402-405	2.0 × 2.4 × 0.128	low	-	low	not flexible, health risks due to high frequency of operation, not wearable only implantable
[62]	Antenna	detection of fluid accumulation in lungs	900	9.7×5.8	low	-	low	not flexible, health risks due to high frequency operation, not wearable
[63]	Antenna with inverse Fourier transform method	congestive heart failure	770 to 1000	14 × 14 × 0.08	very high	25	high	not flexible, health risks due to high frequency of operation, not wearable
[66]	Balanced antipodal Vivaldi antenna	lung water monitoring	1500-6500	-	low	6	low	not flexible, health risks due to high frequency of operation, not wearable
[67]	Flexible inkjet printed on fabric antenna	wearable applications	2450	3 × 3	low	-	low	health risks due to high frequency of operation
[70]	Flexible antenna	wearable applications	8860-21940	6×6×0.3	low	-	low	health risks due to high frequency of operation
[71]	Flexible antenna	wearable applications	1800-3200	7 × 5 × 0.12	low	-	low	health risks due to high frequency of operation

Table 2.3: Comparision table for literature survey of biomedical sensor

Reference	Category	Application	Frequency (MHz)	Size (cm)	Complexity	Error (%)	Cost	Limits
[72]	Conductive textile sensor	pulmonary edema detection	40	10×16	low	<10	low	monitor the permittivity of a single organ only, complex sewing mechanism, high insertion loss than copper, integration of circuit components with e-fiber is difficult
[73]	E-Fiber Sensor	Body-Worn Applications	40	10×16	low	-	low	monitor the permittivity of a single organ only, complex sewing mechanism, high insertion loss than copper, integration of circuit components with e-fiber is difficult
[78]	Microwave textile sensor	Heart rate, breathing and edema monitoring	915	4 × 24	low	-	low	health risks due to high frequency of operation
Proposed	Flexible RF Sensor	Pulmonary edema and emphysema monitoring	60	4 × 89.4	low	4.83	low	-

CHAPTER 3

RESULTS FOR 2-PHASE/3-PHASE OIL RF SENSOR

The proposed sensor is flexible and capable of measuring the volume fraction of the individual phase in a two or three phase combinations of oil, water and gas with no restrictions, small size, low cost and low complexity. The RF sensor consists of 29 electrodes and 28 ports. The first port is excited with 250 MHz RF signal and the remaining 27 ports were terminated with 50 Ω except for the port where the measurement is taken [20]. A flexible substrate (AP9131) is used with a thickness of 0.01016 cm. The planner sensor was designed in high frequency structure simulator (HFSS) software. The simulations are conducted for the frequency range of 200 MHz to 300 MHz with a solution frequency of 250 MHz. The length of each electrode is 5 cm. The substrate dimensions are

$6cm \times 27.93cm$. The first two electrodes were designed to operate at 250 MHz under the best possible matching conditions to perform as the signal exciter. The remaining 27 electrodes receive the radiated fringing field, one active at a time. The width of each electrode is 0.6 cm. The gap between the electrodes was optimized to 0.22 cm. The proposed design of the planner RF sensor with detailed dimensions is shown in Fig. 3.1.

The sensor was wrapped around an acrylic pipe. The length of the acrylic pipe was 62 cm. The outer diameter, outer layer thickness and inner radius of the pipe was 8.89 cm, 0.635 cm and 4.13 cm respectively. The circumference of the pipe was 27.93 cm which was also the substrate length of the RF sensor. The wrap around design of the proposed RF sensor is shown in Fig. 3.2. The electrical properties of the substrate, outer layer and inner layer of the acrylic pipe are given in Table 3.1.

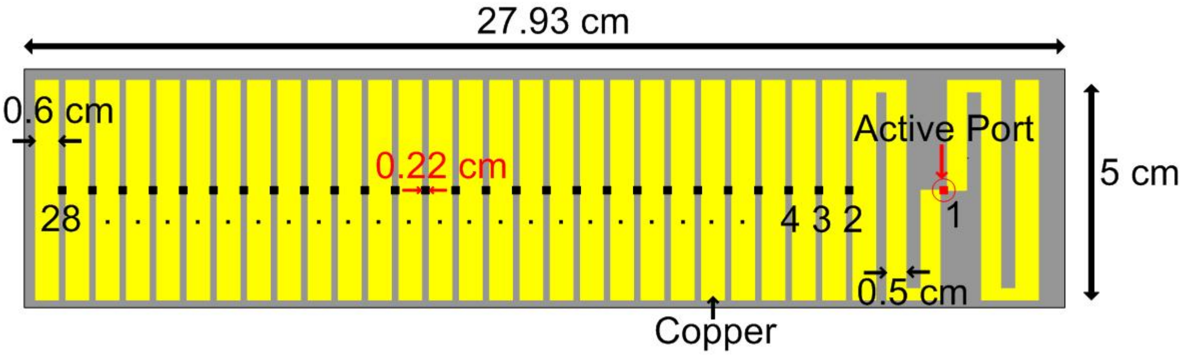

Figure 3.1: Proposed design of planner RF sensor

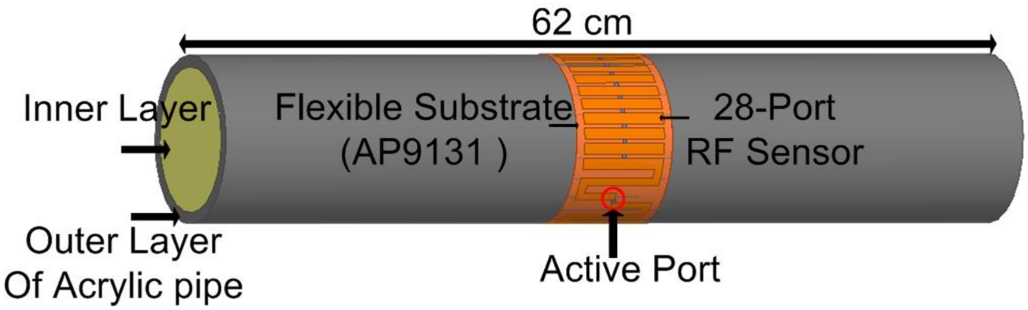

Figure 3.2: Wrap around design of the proposed RF sensor on an acrylic pipe

Table 3.1: Electrical properties of different material used for the design of RF sensor

Material	Thickness (cm)	Permittivity	Loss Tangent	Conductivity	Reference
AP9131	0.01016	3.4	0.002	-	[79]
Outer Layer	0.635	2.5	0.08	-	[80]
Inner Layer	4.13	1-81	0.0182	0.0167	[19]

The dielectric constant (ϵ_r) values for gas, diesel oil and water were 1, 2.2 and 81 respectively. The dielectric constant of the inner layer was varied from 1 to 81. An ϵ_r value of 1 (low ϵ_r) shows that the pipe is filled with 100% gas (air) and 81 (high ϵ_r) shows that the pipe is filled with 100% water. The transmission coefficient (S_{i1}) was obtained for low and high ϵ_r values inside the pipe where i is the port number. The comparison between S_{i1} of low and high ϵ_r values is shown in Fig. 3.3. The maximum achieved dynamic range between low and high ϵ_r was 12 dB at port number 18 while the achieved dynamic range in [20], [81], using ϵ_r values from 1 to 180 was 22 dB for planner and semi planner sensor design. Our proposed design has the dynamic range of 12 dB for ϵ_r variations from 1 to 81. The size of the proposed sensor is smaller than [20] as its operating at 250 MHz. In addition, its features were optimized for the problem requirements and materials used. As the transmission coefficients values were optimized up to -40 dB for all ports of the proposed sensor, there is no need of the RF sensor subgrouping which was done in [81]. The subgrouping of sensor in [81] makes the data collection and post processing difficult. The fabricated RF sensor without coaxial probes is shown in Fig. 3.4 (a), the flexibility of RF sensor is shown in Fig. 3.4 (b), the scaled RF sensor is shown in Fig. 3.4 (c) and Fig. 3.4 (d) shows the fabricated RF sensor with 50Ω coaxial probes.

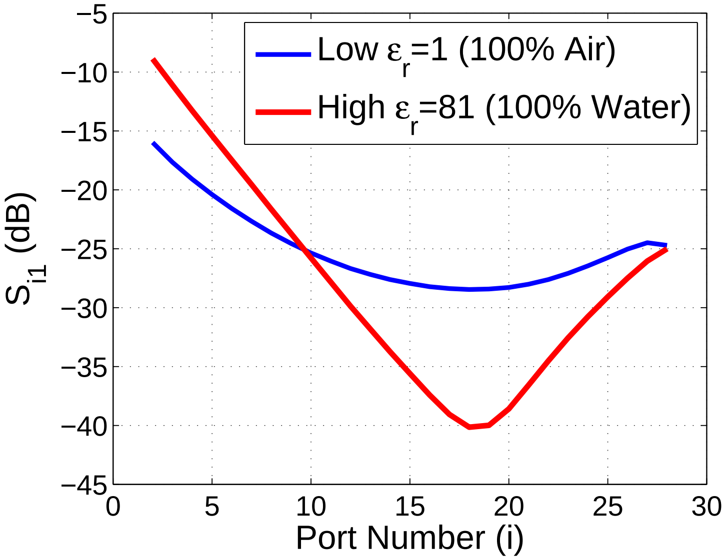

Figure 3.3: Comparison between S_{i1} of low and high ϵ_r

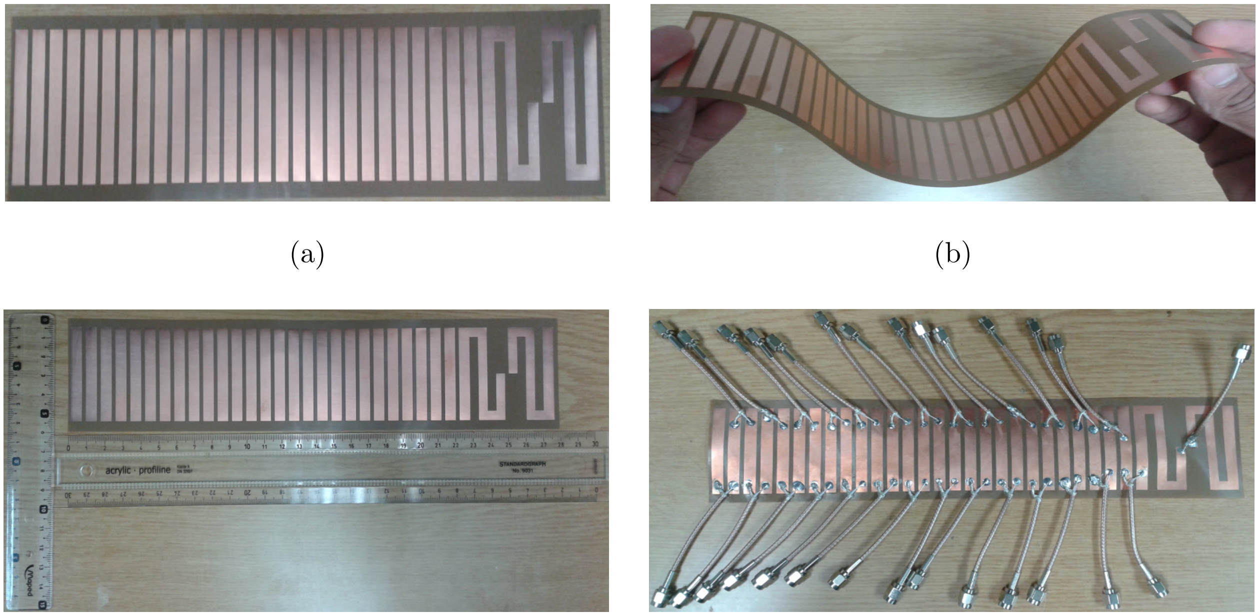

(a) (b)

(c) (d)

Figure 3.4: Fabricated RF sensor (a) RF sensor without coaxial probes (b) Flexibility of RF sensor (c) Scaled RF sensor (d) RF sensor with 50Ω coaxial probes.

3.1 Dielectric Constant Estimation

The S_{i1} curves were collected using HFSS by varying the ϵ_r inside the acrylic pipe from 1 to 100 with the step of 1 for different two/three phase combinations of oil, water and gas. The resultant overdetermined matrix consisting of 100 rows and 27 columns as shown in (3.1) was solved using the least square (LS) method to obtain the weight coefficients. Equation (3.2) was used to get the effective ϵ_r for both simulated and average measured S_{i1} values.

$$\begin{bmatrix} S_{2,1} & S_{3,1} & S_{4,1} & \dots & S_{28,1} \\ S_{2,1} & S_{3,1} & S_{4,1} & \dots & S_{28,1} \\ \vdots & \vdots & \vdots & \ddots & \vdots \\ S_{2,1} & S_{3,1} & S_{4,1} & \dots & S_{28,1} \end{bmatrix} \cdot \begin{bmatrix} w_1 \\ w_2 \\ \vdots \\ w_{27} \end{bmatrix} = \begin{bmatrix} \epsilon_{r1} \\ \epsilon_{r2} \\ \vdots \\ \epsilon_{r100} \end{bmatrix} \tag{3.1}$$

$$\begin{aligned} \epsilon_r = {} & 3.36S_{2,1} + 30.3S_{3,1} + 14.52S_{4,1} - 7.35S_{5,1} + 39.21S_{6,1} - 152.16S_{7,1} + 22.22S_{8,1} \\ & + 126.12S_{9,1} - 35.65S_{10,1} - 17.74S_{11,1} + 89.78S_{12,1} - 82.73S_{13,1} - 64.48S_{14,1} \\ & - 8.32S_{15,1} + 48.22S_{16,1} + 115.96S_{17,1} - 200.6S_{18,1} - 11.09S_{19,1} + 129.77S_{20,1} \\ & + 49.93S_{21,1} - 59.04S_{22,1} - 10.38S_{23,1} + 76.92S_{24,1} - 63.39S_{25,1} - 8.16S_{26,1} \\ & - 17.82S_{27,1} + 2.23S_{28,1} \end{aligned} \tag{3.2}$$

3.2 Experimental Results for the Static Two and Three Phase Combinations

The multiphase flow have the four different combinations of oil, water and gas (oil-water, gas-water, gas-oil and gas-oil-water). We compare the simulated and average measured transmission coefficients S_{i1} using a Vector Network Analyzer (VNA) (Agilent N9918A) and the 28 port RF sensor wrapped around the acrylic pipe for static multiphase oil combinations. We calculate the percentage error in extracting the dielectric constant (ϵ_r) for both average measured and simulated S_{i1}.

3.2.1 Oil-Water Combination

Four cases of oil-water percentages were examined. The sensor was wrapped around at the middle of oil-water filled acrylic pipe. VNA port 1 was connected with the sensor first port which remains the active port and port 2 was stepped between other ports to measure S_{i1}. Each port S_{i1} was measured three times and the average was taken as the final S_{i1} for that port.

The acrylic pipe was filled with the oil volume of 65% and water volume of 35%. The measurement setup for this case is shown in Fig. 3.5(a). Similarly, the measurement setup for 35% oil and 65% water filled pipe is shown in Fig. 3.5(b), for 20% oil and 80% water in Fig. 3.5(c) and for 10% oil and 90% water in Fig. 3.5(d). The comparison between average measured and simulated S_{i1} for the RF sensor wrap around on 65% oil and 35% water filled acrylic pipe is given in Fig.

3.6(a), for 35% oil and 65% water in Fig. 3.6(b), for 20% oil and 80% water in Fig. 3.6(c) and for 10% oil and 90% water in Fig. 3.6(d).

We have observed that the variation in measurements 1, 2 and 3 starts reducing as the water volume inside the pipe increases. By increasing the (ϵ_r) inside the pipe, the measurements get closer to the simulation. The average measured and simulated S_{i1} are in good agreement. The thick blue lines shows the simulated S_{i1} and the average measured S_{i1} are shown as solid red lines in all graphs. The average S_{i1} curves are close to the simulated ones for all cases.

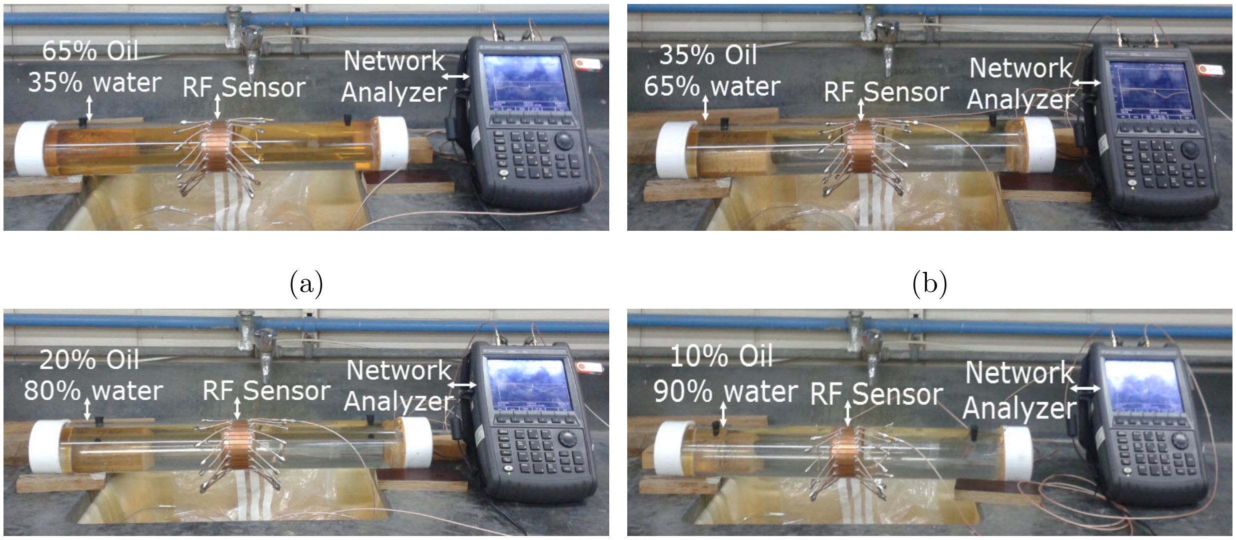

(a) (b)

(c) (d)

Figure 3.5: Experimental setup for oil-water combination filled acrylic pipe (a) 65% oil and 35% water (b) 35% oil and 65% water (c) 20% oil and 80% water (d) 10% oil and 90% water.

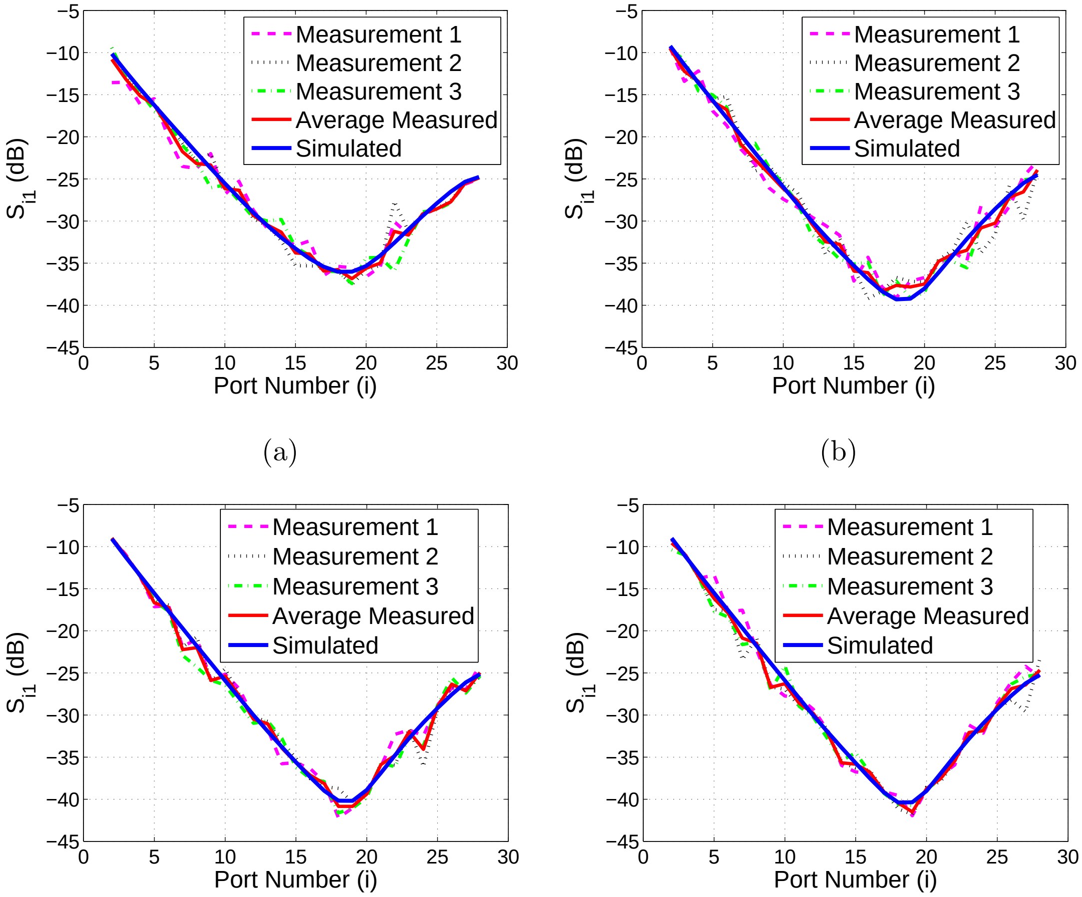

(a) (b)

(c) (d)

Figure 3.6: Comparison of measured, average measured and simulated S_{i1} for oil-water combination filled acrylic pipe (a) 65% oil and 35%water (b) 35% oil and 65%water (c) 20% oil and 80%water (d) 10% oil and 90%water.

By using average measured S_{i1} values in (3.1), we have calculated the average measured ϵ_r for the oil-water combination. Table 3.2 shows the comparison between theoretical verses simulated and average measured effective ϵ_r for the diesel oil-water filled acrylic pipe. The simulated error was due to the weight coefficient prediction using the LS method. We have observed that as the water volume inside the pipe increases the measured error starts decreasing. The average measured error for all four cases is 5.5%. The highest error percentage remained below 10%.

Table 3.2: Comparison of theoretical vs simulated and average measured effective ϵ_r

Sr. No.	Water (%)	Oil (%)	Theoretical ϵ_r	Simulated ϵ_r	Measured ϵ_r	Simulated Error (%)	Measured Error (%)
1	35	65	17	17.2	15.4	1.2	9.2
2	65	35	41	40.7	44.6	0.8	8.8
3	80	20	56	55.1	57.4	1.7	2.5
4	90	10	68	66.2	66.8	2.6	1.8

3.2.2 Gas-Water Combination

Five different cases of gas and water volumes were selected for the experiment. The acrylic pipe was filled with the gas volume of 100%. The measurement setup for this case is shown in Fig. 3.7(a). Similarly, The measurement setup for 25% water and 75% gas filled pipe is shown in Fig. 3.7(b), for 50% water and 50% gas in Fig. 3.7(c), for 75% water and 25% gas in Fig. 3.7(d) and for 100% water in Fig. 3.7(e). The comparison between measured and simulated S_{i1} for the RF sensor wrap around on 100% gas filled acrylic pipe is given in Fig. 3.8(a), for 25% water and 75% gas in Fig. 3.8(b), for 50% water and 50% gas in Fig. 3.8(c), for 75% water and 25% gas in Fig. 3.8(d) and for 100% water in Fig. 3.8(e).

More fluctuations in measurements were observed for high gas volumes inside the pipe. By increasing the ϵ_r inside the pipe, the measurements get closer to simulations. The average measured and simulated S_{i1} are in good agreement as well. The thick blue lines shows the simulated S_{i1} and average measured S_{i1} are shown as solid red lines in all graphs.

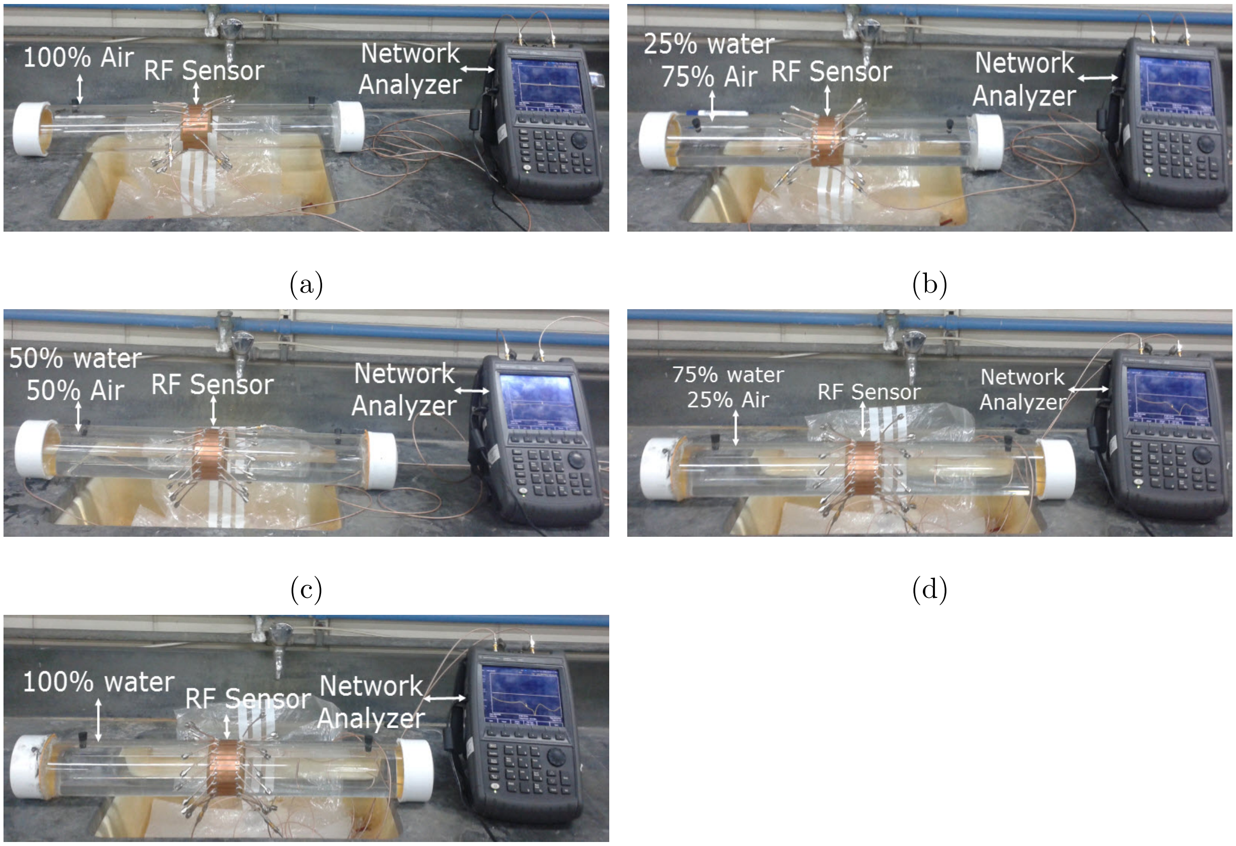

(a) (b) (c) (d) (e)

Figure 3.7: Experimental setup for gas-water combination filled acrylic pipe (a) 100% gas (b) 75% gas and 25% water (c) 50% gas and 50% water (d) 25% gas and 75% water(e) 100% water.

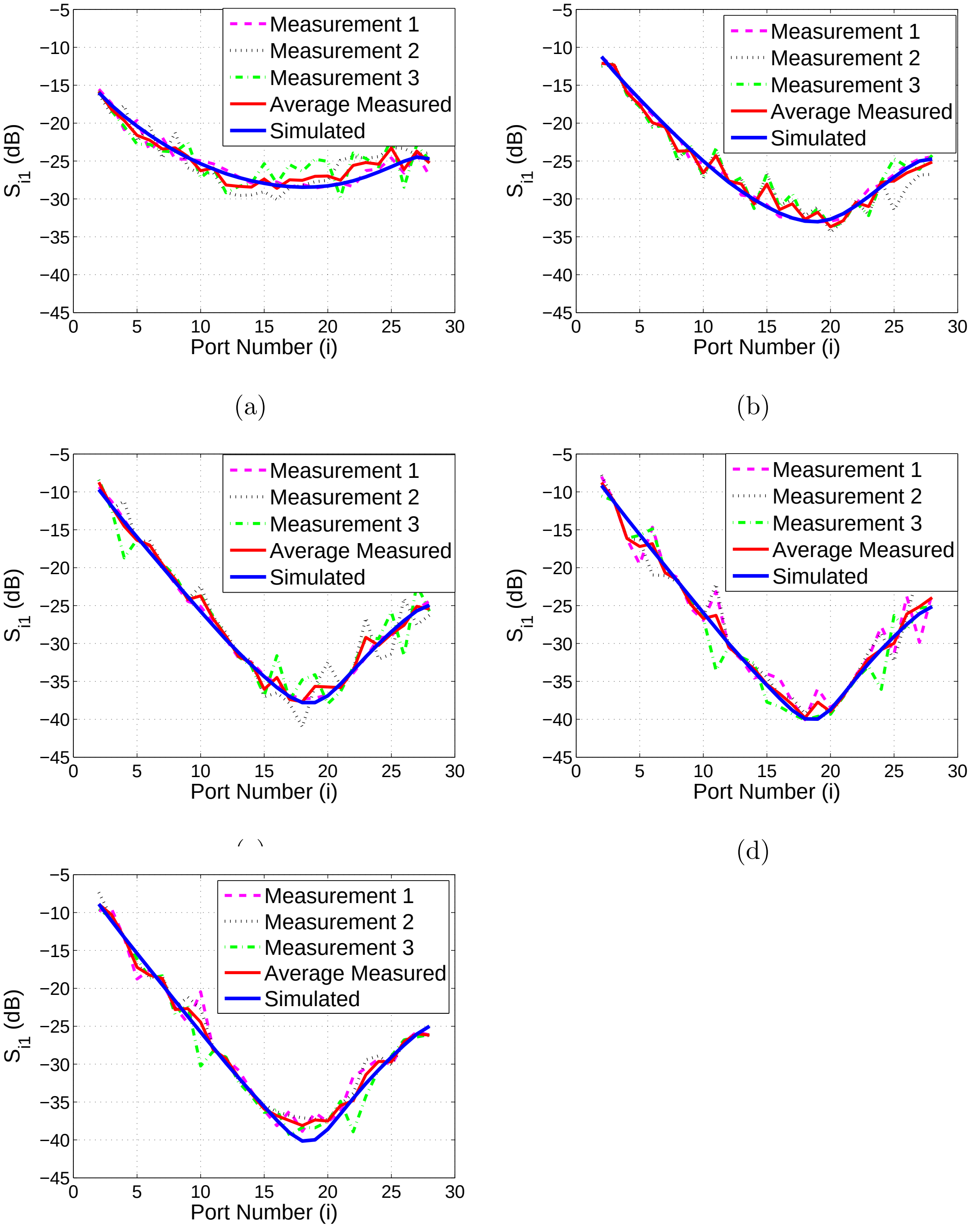

(a)

(b)

( )

(d)

(e)

Figure 3.8: Comparison of measured, average measured and simulated S_{i1} for gas-water combination filled acrylic pipe (a) 100% gas (b) 75% gas and 25% water (c) 50% gas and 50% water (d) 25% gas and 75% water(e) 100% water.

Table 3.3 shows the comparison between theoretical verses simulated and average measured effective ϵ_r for gas-water filled acrylic pipe. Similar behavior was observed as in oil-water combination. As the water volume inside the pipe increases (ϵ_r increases), the measured error starts decreasing. The average measured error for all five cases is 17.7% and excluding 100% gas case 14%. For smaller ϵ_r values, small changes in the measured values results in a large error percentages but still we have measured values closer to the theoretical.

Table 3.3: Comparison of theoretical vs simulated and average measured effective ϵ_r for gas-water combination

Sr. No.	Water (%)	Gas (%)	Theoretical ϵ_r	Simulated ϵ_r	Measured ϵ_r	Simulated Error (%)	Measured Error (%)
1	0	100	1	0.52	1.3	48	30
2	25	75	9	7.52	10.8	16.4	19.7
3	50	50	25	26.6	20.7	6.6	17.4
4	75	25	49	50.37	53.1	2.8	8.3
5	100	0	81	80.9	90	0.1	11.1

3.2.3 Gas-Oil Combination

Four different cases of gas and oil volume were selected for the experiment. The acrylic pipe was filled with the diesel oil volume of 25% and gas 75%. The measurement setup for this case is shown in Fig. 3.9(a). Similarly, the measurement setup for 50% oil and 50% gas filled pipe is shown in Fig. 3.9(b), for 75% oil and 25% gas in Fig. 3.9(c) and for 100% oil in Fig. 3.9(d). The comparison between measured and simulated S_{i1} for the RF sensor wrap around on 25% oil and 75%

gas filled acrylic pipe is shown in Fig. 3.10(a), for 50% oil and 50% gas in Fig. 3.10(b), for 75% gas and 25% gas in Fig. 3.10(c) and for 100% oil in Fig. 3.10(d).

As both oil and gas has low ϵ_r values, the average ϵ_r is low inside the pipe for this experiment. Large variations in the three measurements have been observed but the average measured curves are close to the simulated curves for all cases. The thick blue lines shows the simulated S_{i1} and average measured S_{i1} are shown as solid red line in all graphs.

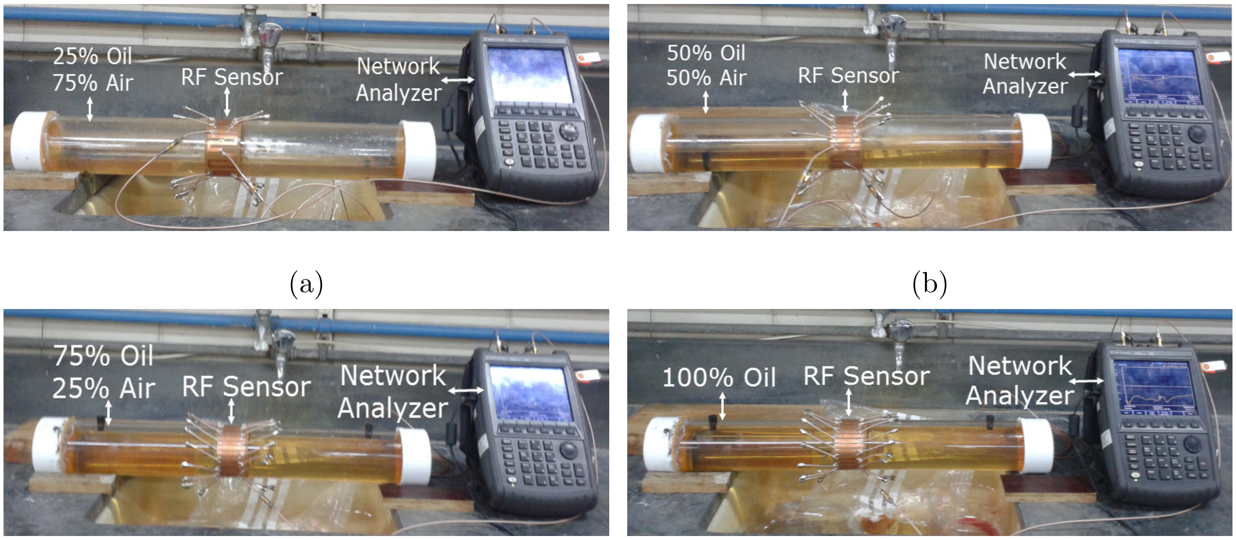

(a) (b)

(c) (d)

Figure 3.9: Experimental setup for gas-oil combination filled acrylic pipe (a) 75% gas and 25% oil (b) 50% gas and 50% oil (c) 25% gas and 75% oil (d) 100% oil.

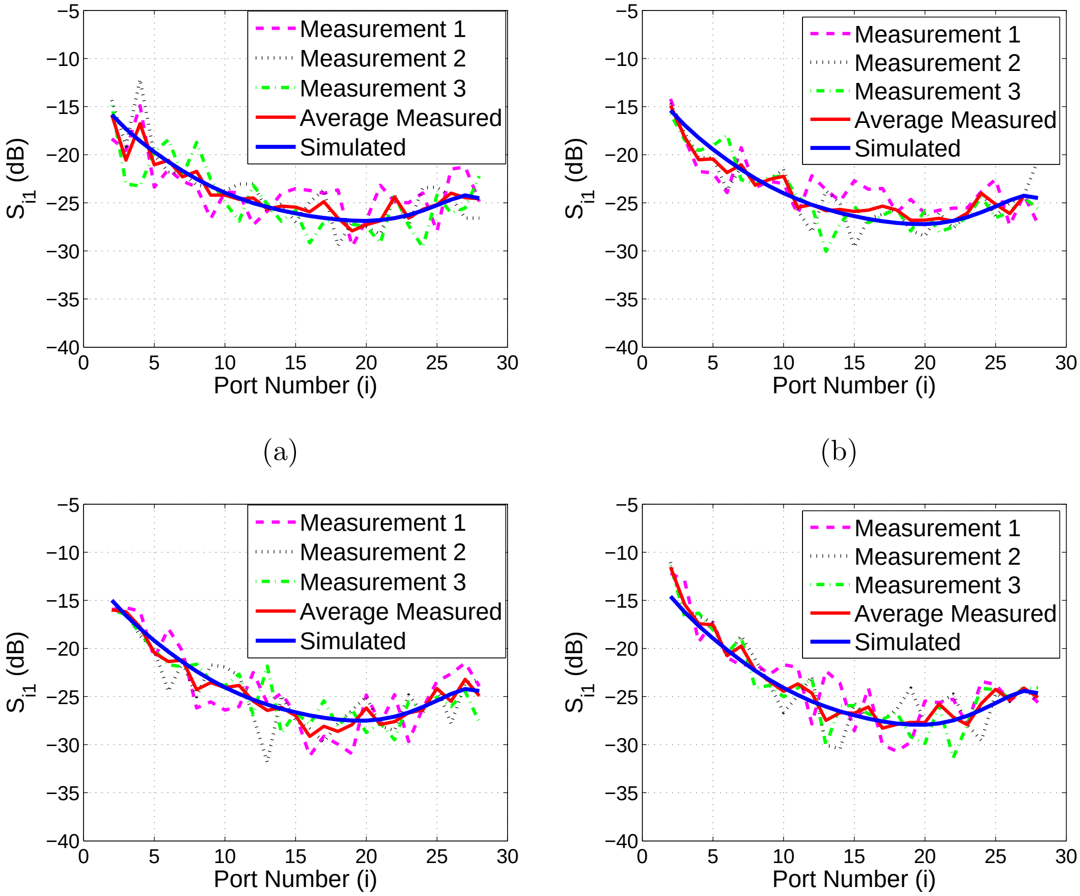

(a) (b)

(c) (d)

Figure 3.10: Comparison of measured, average measured and simulated S_{i1} for gas-oil combination filled acrylic pipe (a) 75% gas and 25% oil (b) 50% gas and 50% oil (c) 25% gas and 75% oil (d) 100% oil.

Table 3.4 shows the comparison between theoretical verses simulated and average measured effective ϵ_r for gas-oil filled acrylic pipe. The simulated error was due to the weight estimation using least square method which was high due to low average ϵ_r values. The average measured error for all four cases is 16%. For smaller ϵ_r values, minor change in measured values results in a large error percentages but still we got measured values close to the theoretical one.

Table 3.4: Comparison of theoretical vs simulated and average measured effective ϵ_r for gas-oil combination

Sr. No.	Oil (%)	Gas (%)	Theoretical ϵ_r	Simulated ϵ_r	Measured ϵ_r	Simulated Error (%)	Measured Error (%)
1	25	75	1.26	0.7	1.4	42.1	8
2	50	50	1.54	1.9	1.1	26	28.1
3	75	25	1.86	1.6	2.2	15.3	18.7
4	100	0	2.2	2.1	2.4	4.6	9.5

3.2.4 Three Phase Combination

Ten different cases of gas, water and oil volumes were selected for this experiment. The acrylic pipe was filled with the 20% volume of water 10% oil and 70% gas. The measurement setup for this case is shown in Fig. 3.11(a). Similarly, The measurement setup for 30% water 20% oil and 50% gas filled pipe is shown in Fig. 3.11(b), for 40% water 30% oil and 30% gas in Fig. 3.11(c), for 55% water 40% oil and 5% gas in Fig. 3.11(d), for 5% water 90% oil and 5% gas in Fig. 3.11(e), for 10% water 80% oil and 10% gas in Fig. 3.11(f), for 20% water 70% oil and 10% gas in Fig. 3.11(g), for 30% water 50% oil and 20% gas in Fig. 3.11(h), for 30% water 60% oil and 10% gas in Fig. 3.11(i) and for 40% water 50% oil and 10% gas in Fig. 3.11(j).

The comparison between average measured and simulated S_{i1} for the oil sensor wrap around on 20% water 10% oil and 70% gas filled acrylic pipe is displayed in Fig. 3.12(a), for 30% water 20% oil and 50% gas in Fig. 3.12(b), for 40% water 30% oil and 30% gas in Fig. 3.12(c), for 55% water 40% oil and 5% gas in Fig. 3.12(d), for 5% water 90% oil and 5% gas in Fig. 3.12(e), for 10% water 80% oil and 10% gas in Fig. 3.12(f), for 20% water 70% oil and 10% gas in Fig. 3.12(g), for 30% water 50% oil and 20% gas in Fig. 3.12(h), for 30% water 60% oil and 10% gas in Fig. 3.12(i) and for 40% water 50% oil and 10% gas in Fig. 3.12(j).

Large variations in the three measurements have been observed for low ϵ_r inside the pipe. By increasing the ϵ_r inside the pipe, the measurements get close to the simulation. The average measured and simulated S_{i1} are in good agreement. The thick blue lines shows the simulated S_{i1} and average measured S_{i1} are shown as solid red lines in all graphs.

Table 3.5 shows the comparison between theoretical verses simulated and average measured effective ϵ_r for water-oil-gas filled acrylic pipe. As water volume inside the pipe increases, the measured errors start decreasing. The average measured error for all cases is 6.2%. The highest error is less than 11%.

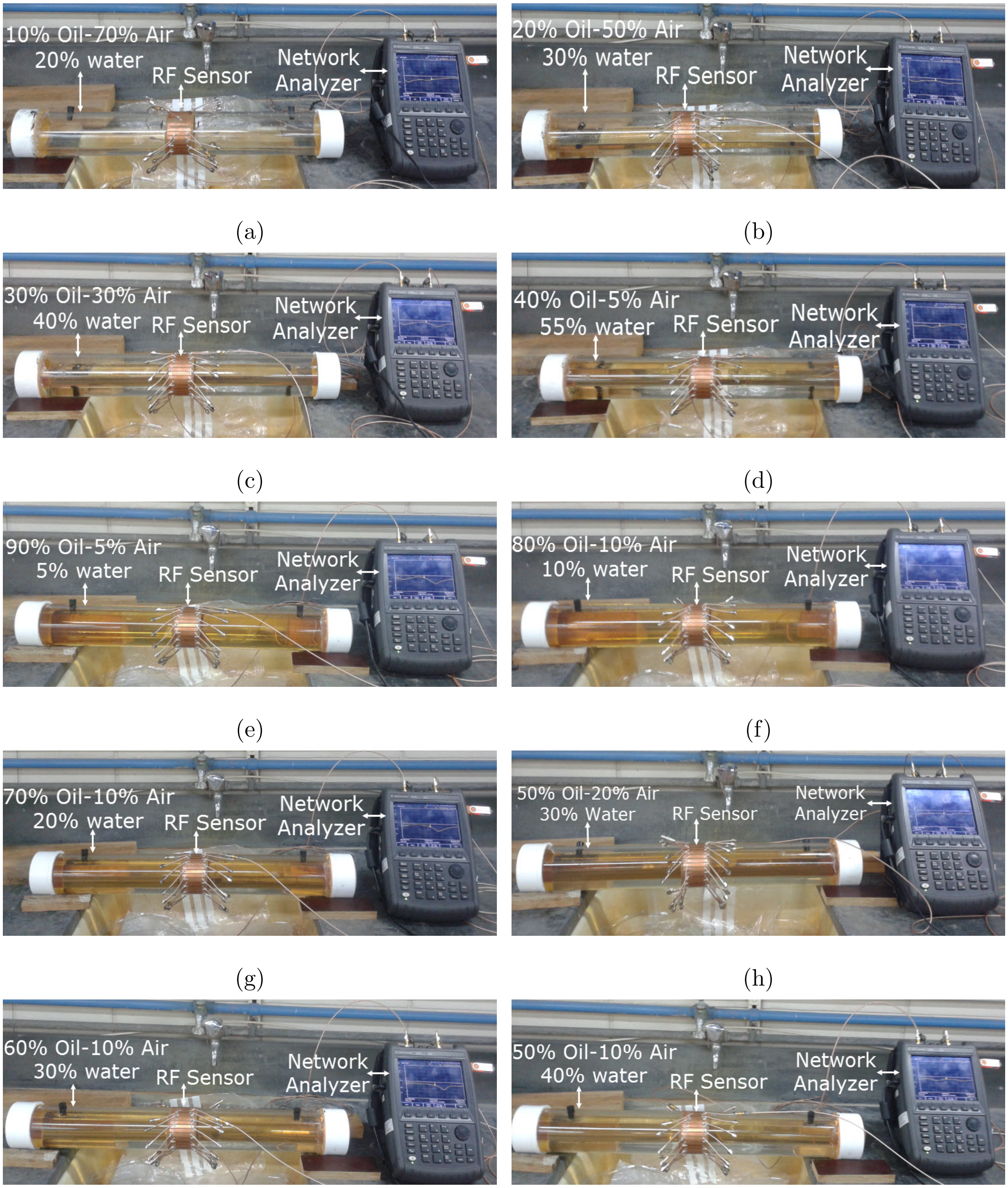

(a) (b)

(c) (d)

(e) (f)

(g) (h)

(i) (j)

Figure 3.11: Experimental setup for water-oil-gas combination filled acrylic pipe (a) 20% water, 10% oil and 70% gas (b) 30% water, 20% oil and 50% gas (c) 40% water, 30% oil and 30% gas (d) 55% water, 40% oil and 5% gas (e) 5% water, 90% oil and 5% gas (f) 10% water, 80% oil and 10% gas (g) 20% water, 70% oil and 10% gas (h) 30% water, 50% oil and 20% gas (i) 30% water, 60% oil and 10% gas (j) 40% water, 50% oil and 10% gas.

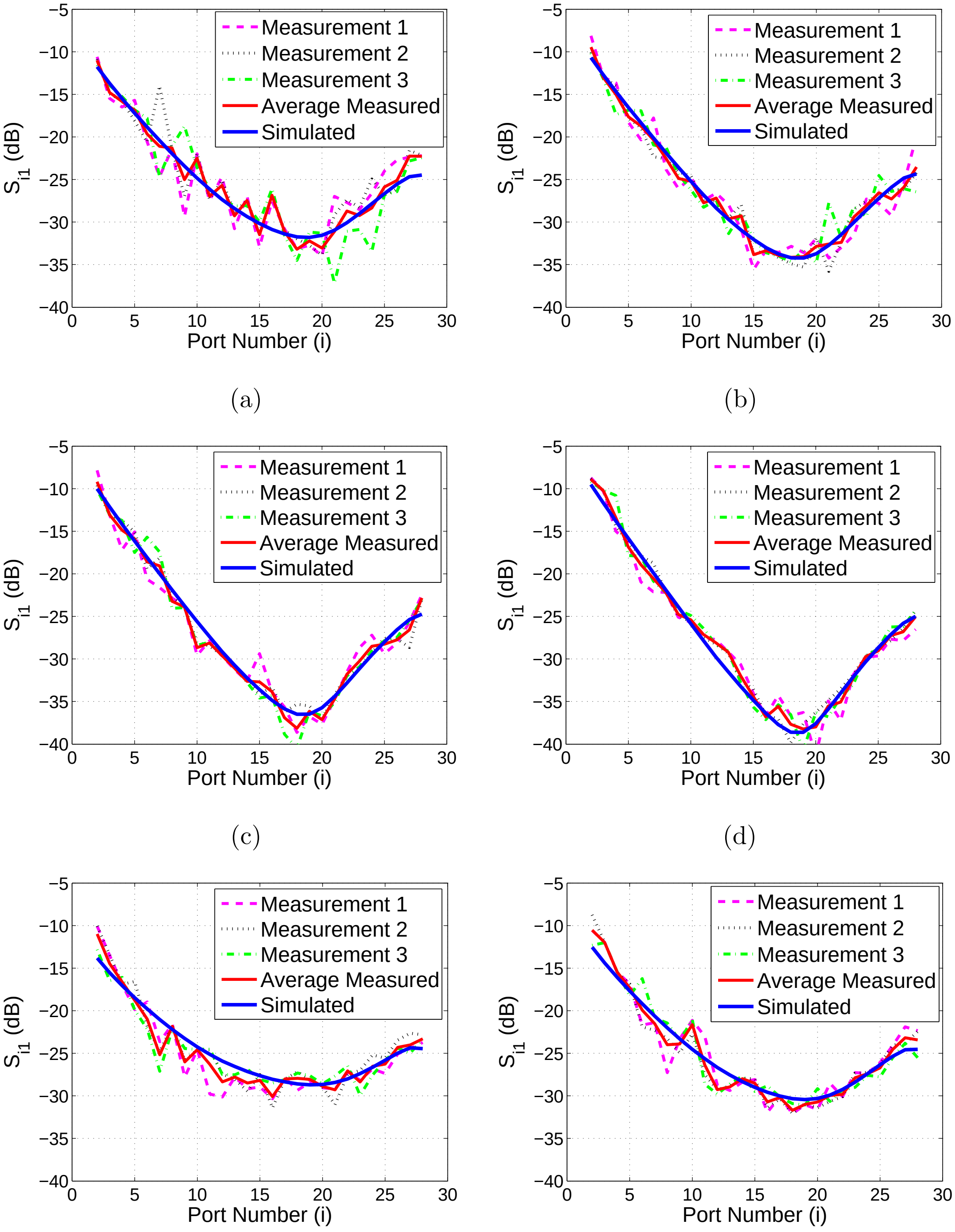
Measurement 1
Measurement 2
Measurement 3
Average Measured
Simulated
S$_{i1}$ (dB)
Port Number (i)
−5
−10
−15
−20
−25
−30
−35
−40
0
5
10
15
20
25
30

(a) (b)

(c) (d)

(e) (f)

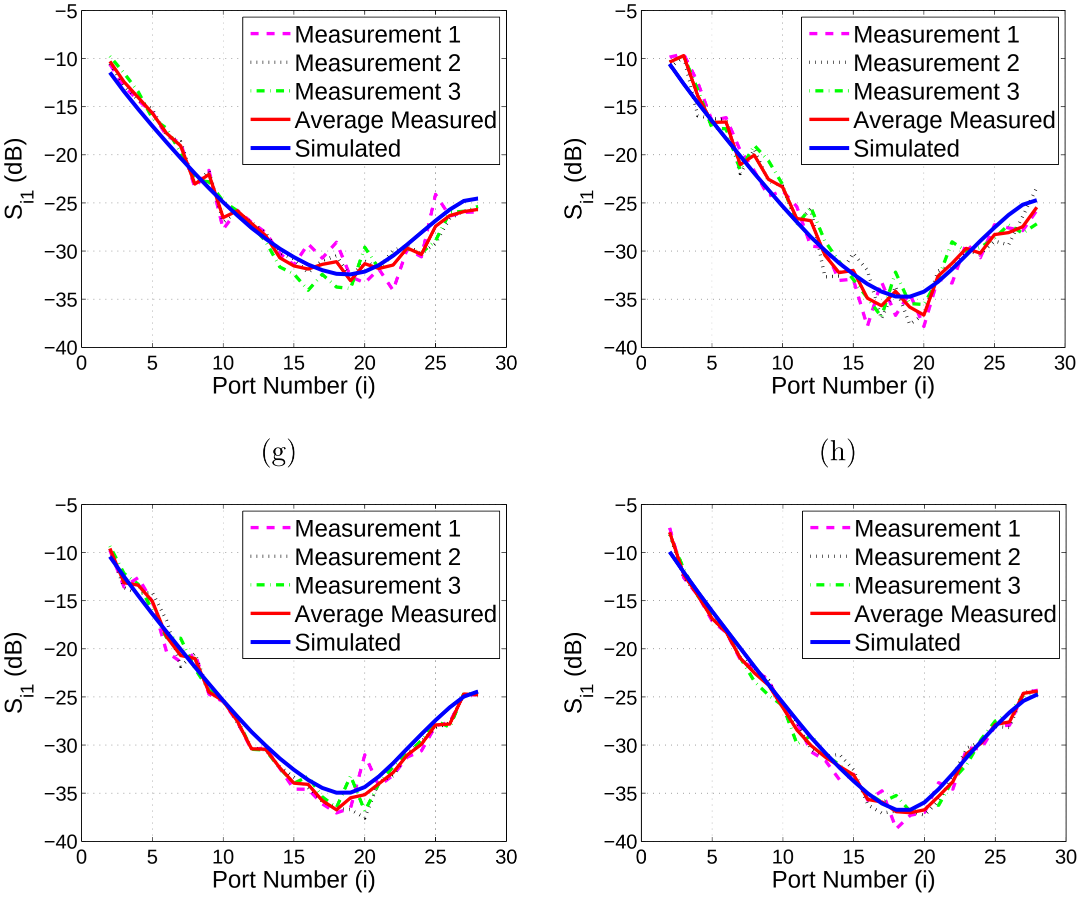

(g) (h)

(i) (j)

Figure 3.12: Comparison of measured, average measured and simulated S_{i1} for water-oil-gas combination filled acrylic pipe (a) 20% water, 10% oil and 70% gas (b) 30% water, 20% oil and 50% gas (c) 40% water, 30% oil and 30% gas (d) 55% water, 40% oil and 5% gas (e) 5% water, 90% oil and 5% gas (f) 10% water, 80% oil and 10% gas (g) 20% water, 70% oil and 10% gas (h) 30% water, 50% oil and 20% gas (i) 30% water, 60% oil and 10% gas (j) 40% water, 50% oil and 10% gas.

Three Phase Combination including Surfactant

One case (30% water, 50% oil and 20% air) of the three phase oil combination was selected for this experiment. A few drops of surfactant (for reducing the surface tension between oil and water) was added in the three phase combination and after

Table 3.5: Comparison of theoretical vs simulated and average measured effective ϵ_r for water-oil-gas combination

Sr. No.	Water (%)	Oil (%)	Gas (%)	Theoretical ϵ_r	Simulated ϵ_r	Measured ϵ_r	Simulated Error(%)	Measured Error(%)
1	20	10	70	7	6.6	7.8	5.5	10.6
2	30	20	50	12	11.1	11.4	9.1	6.4
3	40	30	30	19	20.7	17.1	9.6	9.4
4	55	40	5	31	30.8	31.8	1.5	1.7
5	5	90	5	3.4	3.7	3.4	10.3	1.9
6	10	80	10	5	6	5.1	19.9	2.2
7	20	70	10	8	7.5	8.8	6	9.4
8	30	50	20	13	13	14.2	0.1	9.1
9	30	60	10	14	14.1	13.1	1	6.3
10	40	50	10	20	20	21	0.1	5.1

shaking, the mixture become homogeneous. The experimental setup is shown in Fig. 3.13(a) and an enlarged view of the three phase homogeneous mixture is shown in Fig. 3.13(b). Each port measurement was taken three times and the average measurement was considered for the dielectric constant estimation. The comparison of S_{i1} between the measurements and simulations is displayed in Fig. 3.13(c). The average measured S_{i1} are in good agreement with the simulated one. In comparison to Fig. 3.12(h), we can see that variation in measurements reduce in Fig. 3.13(c) which was due to the fact that the mixture was homogeneous.

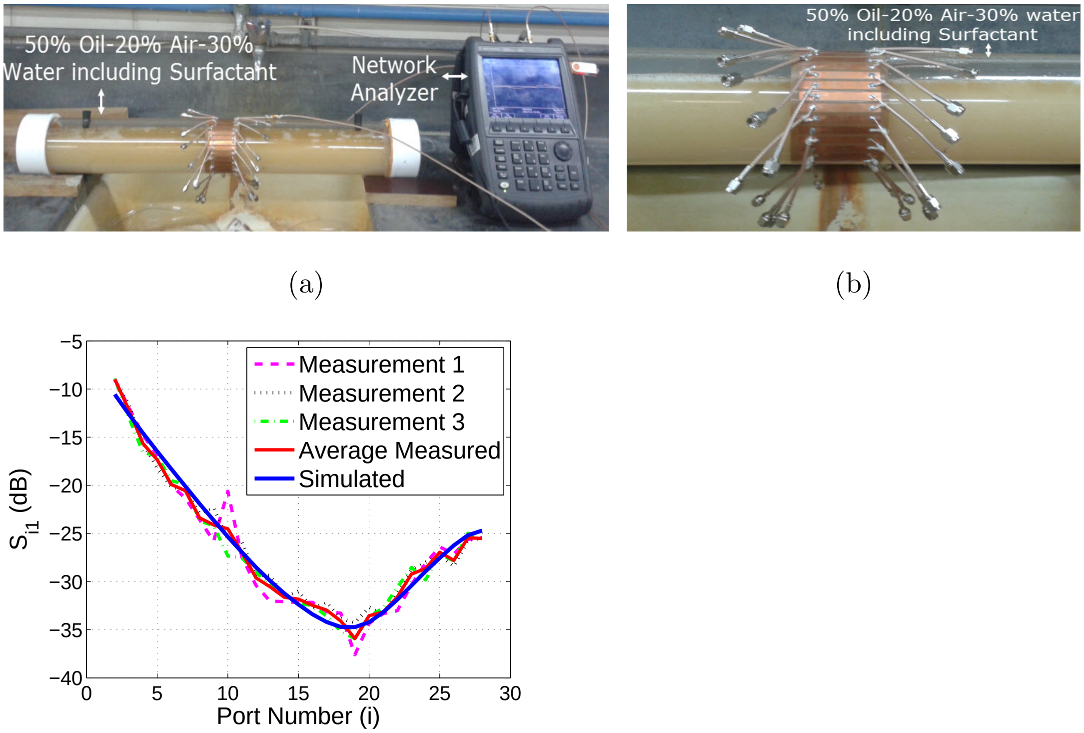

(a) (b)

(c)

Figure 3.13: Experimental setup by including surfactant in water-oil-gas combination (a) 30% water, 50% oil and 20% gas (b) Enlarge view for 30% water, 50% oil and 20% gas (c) Comparison of measured, average measured and simulated S_{i1}

Table 3.6 shows the comparison between theoretical verses simulated and average measured effective ϵ_r. The measured error is 4.3%. In comparison to non-homogeneous mixture in Table 3.5 Sr. No. 8, we have seen that the error percentage reduces in the homogeneous mixture.

Table 3.6: Comparison of theoretical vs simulated and average measured effective ϵ_r for the water-oil-gas combination including the surfactant

Sr. No.	Water (%)	Oil (%)	Gas (%)	Theoretical ϵ_r	Simulated ϵ_r	Measured ϵ_r	Simulated Error(%)	Measured Error(%)
1	30	50	20	13	13	12.4	0.1	4.3

100% Water Case at 80°C

The pipe was filled with 100% water at 80^oC. This temperature was reduced to 72^oC during last port S_{i1} measurement. Figure 3.14 shows a comparison of S_{i1} between average measurement at room temperature and at 80^oC for 100% water case. By increasing the temperature, the S_{i1} responses is totally different than previous average measurement results at room temperature. The measured ϵ_r is 140 for that case which is far away from the theoretical ϵ_r of 81. This experiment gave us different S-parameters which we did not consider in LS method weight estimation (as the temperature variations were not considered in simulations). The large deviation might be from the sensor array behavior. The metal conductors might get affected as their conductivity might change, and the impedances between them thus might get affected, changing the behavior of the sensor properties to some extent.

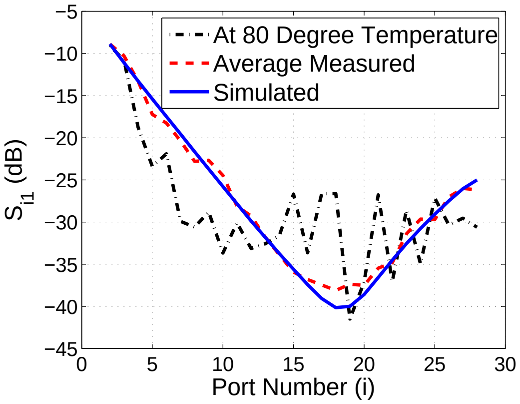

Figure 3.14: Comparison between S_{i1} of low and high ϵ_r

3.3 Experimental Results for the Shake Test of Three Phase Combination

Five different cases of oil, water and gas were selected for the experiment. The shaking of three phase combination inside the pipe was performed to make a bubbly and wavey flow pattern. Each port S_{i1} was measured three times and the average was taken as final S_{i1} for that port.

The acrylic pipe was filled with the 5% water, 90% oil and 5% gas . The measurement setup for this case is shown in Fig. 3.15(a). The enlarged view of three phase combination after shaking is shown in Fig. 3.15(b). Similarly, the measurement setup for 10% water 80% oil and 10% gas filled pipe is given in Fig. 3.15(c) and enlarged view of three phase combination after shaking is shown in Fig. 3.15(d). The measurement setup for 20% water 70% oil and 10% gas filled pipe is shown in Fig. 3.15(e) and enlarged view of three phase combination after shaking is shown in Fig. 3.15(f). The measurement setup for 30% water 60% oil and 10% gas filled pipe is given in Fig. 3.15(g) and enlarged view of three phase combination after shaking is shown in Fig. 3.15(h). The measurement setup for 40% water 50% oil and 10% gas filled pipe is shown in Fig. 3.15(i) and enlarged view of three phase combination after shaking is shown in Fig. 3.15(j). The comparison between average measured and simulated S_{i1} for the RF sensor wrap around on 5% water 90% oil and 5% gas filled acrylic pipe is given in Fig. 3.16(a), for 10% water 80% oil and 10% gas in Fig. 3.16(b), for 20% water 70% oil and 10% gas in Fig. 3.16(c), for 30% water 60% oil and 10% gas in Fig. 3.16(d) and for 40% water 50% oil and 10% gas in Fig. 3.16(e).

There is no noticeable effect on fluctuations in measurements by increasing the (ϵ_r) inside the pipe. This behavior is different from the previous static cases. This is due to the fact that shaking the pipe may result in high water concentration at a location in one point and high oil concentration in another during of the same time interval. The average measured and simulated S_{i1} are still in good agreement. The thick blue lines shows the simulated S_{i1} and average measured S_{i1} are shown as solid red lines in all graphs.

Table 3.7 shows the comparison between theoretical, simulated and average measured effective ϵ_r for the shake test of water-oil-gas. As water volumes inside the pipe increases, the measured error starts reducing in many cases. The average measured error for all cases is 9.3%. The highest error is less than 15% which was due to the shaking process.

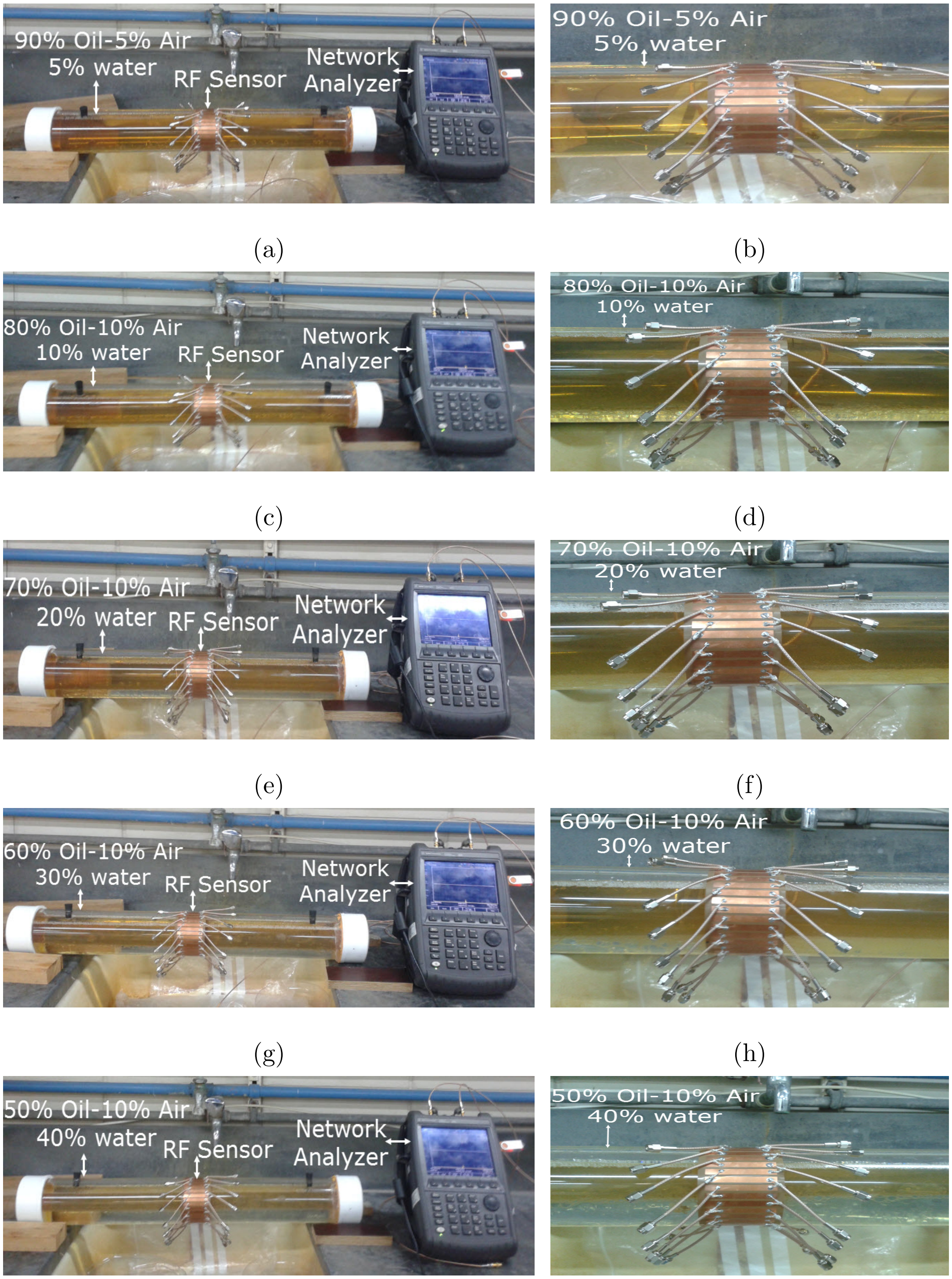

(a) (b)

(c) (d)

(e) (f)

(g) (h)

(i) (j)

Figure 3.15: Experimental setup for shake test of water-oil-gas combination filled acrylic pipe (a) 5% water, 90% oil and 5% gas (b) Enlarge view for 5% water, 90% oil and 5% gas (c) 10% water, 80% oil and 10% gas (d) Enlarge view for 10% water, 80% oil and 10% gas (e) 20% water, 70% oil and 10% gas (f) Enlarge view for 20% water, 70% oil and 10% gas (g) 30% water, 60% oil and 10% gas (h) Enlarge view for 30% water, 60% oil and 10% gas(i) 40% water, 50% oil and 10% gas (j) Enlarge view for 40% water, 50% oil and 10% gas.

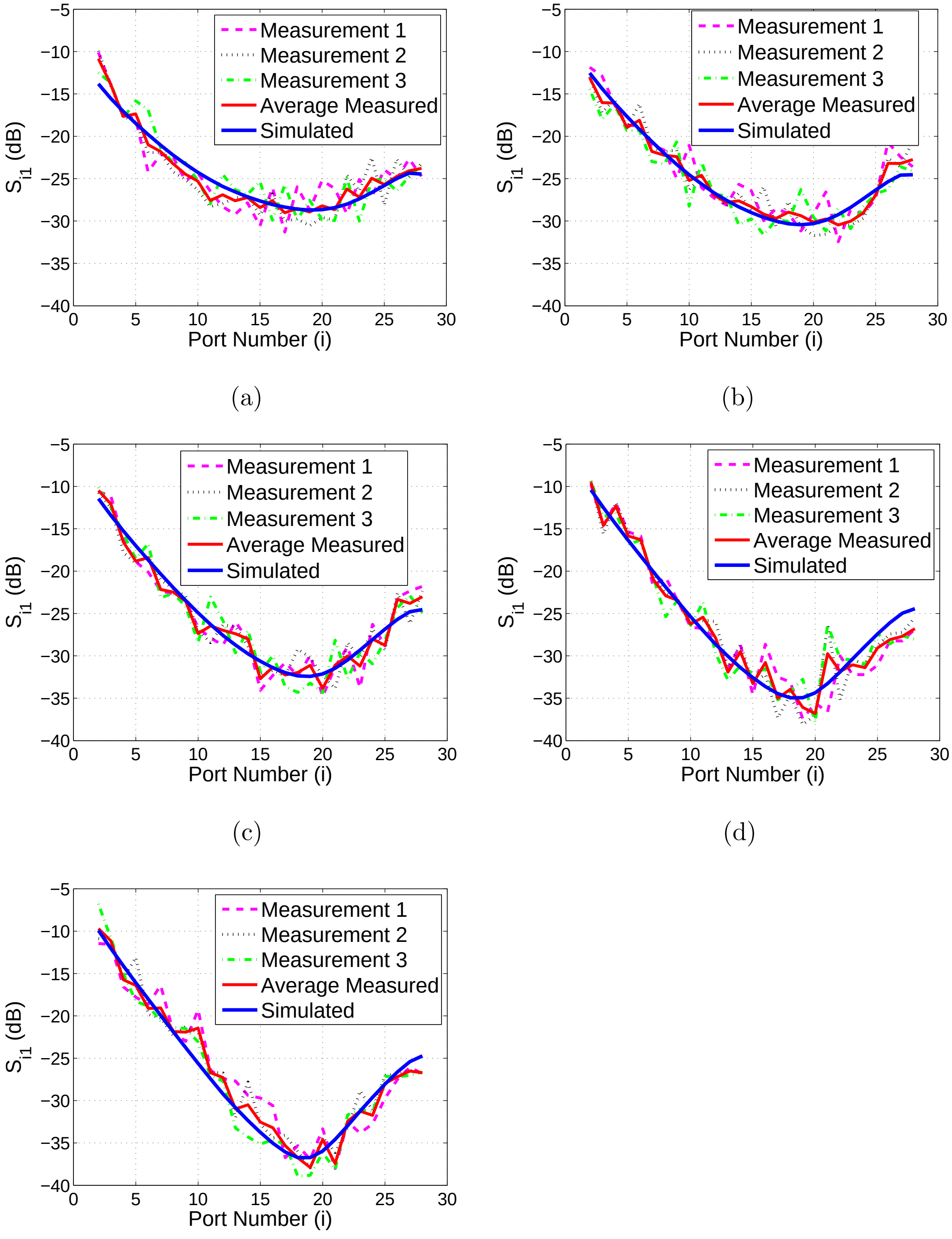

(a)

(b)

(c)

(d)

(e)

Figure 3.16: Comparison of measured, average measured and simulated S_{i1} for shake test of water-oil-gas combination filled acrylic pipe (a) 5% water, 90% oil and 5% gas (b) 10% water, 80% oil and 10% gas (c) 20% water, 70% oil and 10% gas (d) 30% water, 60% oil and 10% gas (e) 40% water, 50% oil and 10% gas.

Table 3.7: Comparison of theoretical vs simulated and average measured effective ϵ_r for the shake test of water-oil-gas combination

Sr. No.	Water (%)	Oil (%)	Gas (%)	Theoretical ϵ_r	Simulated ϵ_r	Measured ϵ_r	Simulated Error(%)	Measured Error(%)
1	5	90	5	3.4	3.7	3.7	9.2	8.8
2	10	80	10	5	6	5.7	19.9	14.7
3	20	70	10	8	7.5	8.8	6	10
4	30	60	10	14	14.1	13.1	1	6.4
5	40	50	10	20	20	21.4	0.1	6.9

The Dantec speedsense camera 9040 with maximum exposure time of $2us$ was used to see the bubbly and wavey flow pattern during shaked up condition. The speedsense camara images for 30% water, 50% oil and 20% gas combination are shown in Fig. 3.17. Fig. 3.17(a) shows the static case of 3-phase combination with water at bottom, oil in middle and gas at top of the acrylic pipe. Fig. 3.17(b) shows the shaked up case of 3-phase combination which has the clear wavey and bubbly pattern. By adding the surfactant in 3- phase combination, the mixture is looking like a single phase as shown in Fig. 3.17(c).

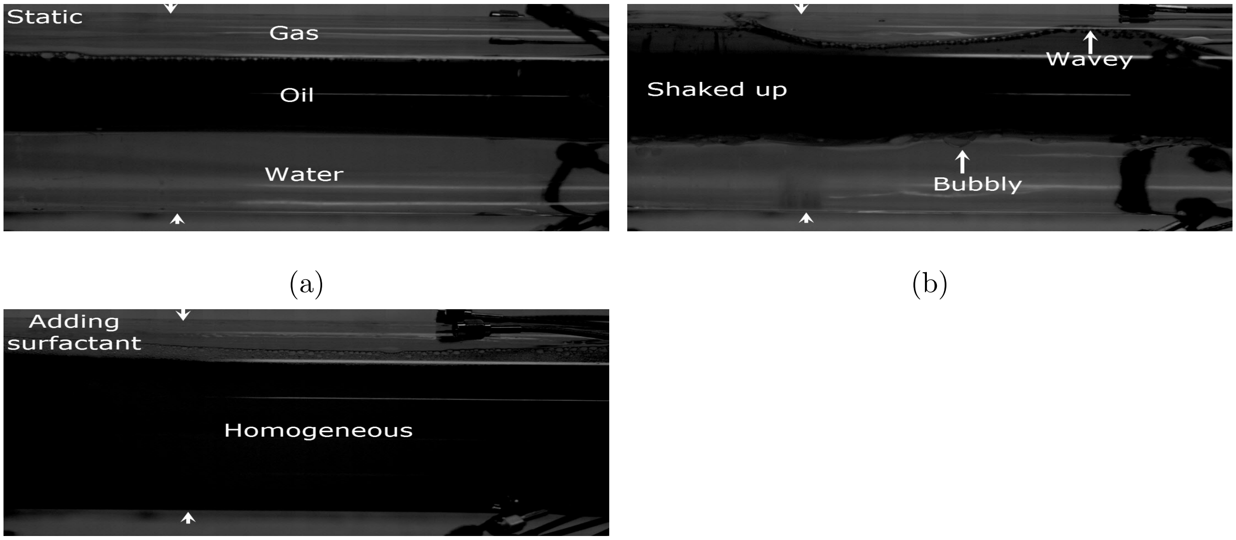

(a)

(b)

(c)

Figure 3.17: Speedsense camara images for 30% water, 50% oil and 20% gas combination(a) Static (b) Shaked (c) Adding surfactant.

3.4 Conclusions

A 28-port RF based low cost, low complexity and non-invasive sensor for average ϵ_r estimation is presented for two/three phase oil flow measurements. The sensor was build on a AP9131 flexible substrate of $6 \times 27.93 \times 0.01016 cm^3$ size. 2-phase and 3-phase static and dynamic tests were conducted. It was found that the sensor can achieve 9.8% in measured ϵ_r estimation errors with more accurate estimate for high ϵ_r combinations. The shake test for the 3-phase combinations of oil-water-gas showed average measured errors of 9.3%. This is the first low cost, low complexity sensor that provide accurate ϵ_r estimation with less than 10% average errors across its dynamic range and works (was tested for) with 2-phase, 3-phase static cases and 3-phase shaked up (dynamic) scenarios.

CHAPTER 4

RESULTS FOR BIOMEDICAL RF SENSOR

In this chapter, the RF sensor design on a fabric substrate is discussed. The details of the RF sensor design on a thin polyimide substrate is provided. Detailed experimental results of the proposed RF sensor on polyimide substrate using silver organo complex (SOC) ink are presented along with experimental results of the final fabricated RF sensor using advanced nano products (ANP) silver ink. The modeling of the human upper torso is presented and errors obtained in the estimated ϵ_r values are analyzed.

4.1 RF Sensor on Fabric Substrate

The designed RF sensor consists of 38 electrodes and 37 ports. The first port is excited with a 60 MHz RF signal and the remaining 36 ports are terminated with 50 Ω except for the port where the measurement is taken. A textile substrate is initially used with a thickness of 0.8 mm. The first two electrodes were designed to operate at 60 MHz under the best possible matching conditions to perform as the signal exciter. The remaining 36 electrodes receive the radiated fringing field, one active at a time. The width of the proposed sensor is 4 cm which is 60% smaller than [45], [58] and 20% smaller than [59]. The length of the RF sensor is 89.4 cm which represents the circumference of an average adult human chest. The proposed design of the textile RF sensor with detailed dimensions is shown in Fig. 4.1 (a). The sensor is wrapped around an elliptical model representing an average upper torso (adult human chest) in simulation for the first time (all privious works dealt with cylindrical models). The wrap around design of the proposed RF sensor is shown in Fig. 4.1 (b). The skin, fat, muscles and bones are modeled as an outer layer with an average thickness of 1.5 cm as reported in [45] and [58]. The inner layer of an average human adult is modeled with a thickness of 31.62 cm. The electrical properties of the inner and outer layers of the chest model are given in Table 4.1.

Table 4.1: Electrical properties of different meterials used for the design of the RF sensor

Material	Thickness (cm)	Permittivity	Loss Tangent	Conductivity	Reference
Textile substrate	0.08	2.57	0.019	-	[67]
Outer Layer	1.5	40.6	2.33	0.38	[45], [58]
Inner Layer	31.62	1-120	2-3	0.3-0.5	[58]

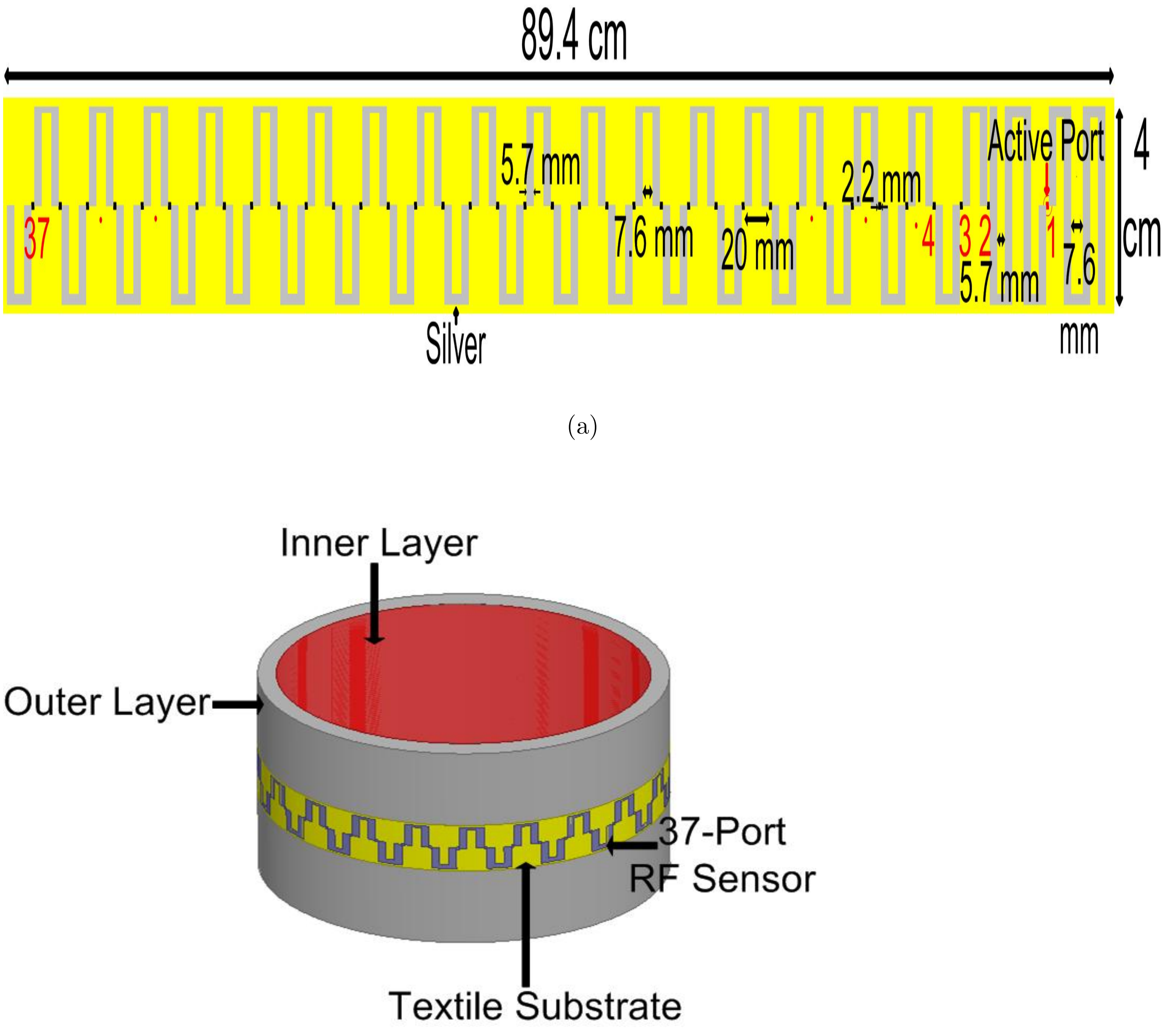

(a)

(b)

Figure 4.1: RF sensor dimentions (a) planner Design (b) wrap around design on human chest model.

The dielectric constant inside the inner layer of the chest model is varied from 1 to 120 to see the dynamic range of the proposed sensor. The S_{i1} curves for different dielectric constant values (1, 30, 60, 90, 120) in the inner layer are shown in Figure 4.2 with the maximum dynamic range of 25 dB at port 18. The second highest dynamic range is observed at port 32. The graph shows the S_{i1} values with respect to the port number. The shift in S_{i1} curves by changing the dielectric constant in the inner layer is good for ϵ_r estimation using the LS method.

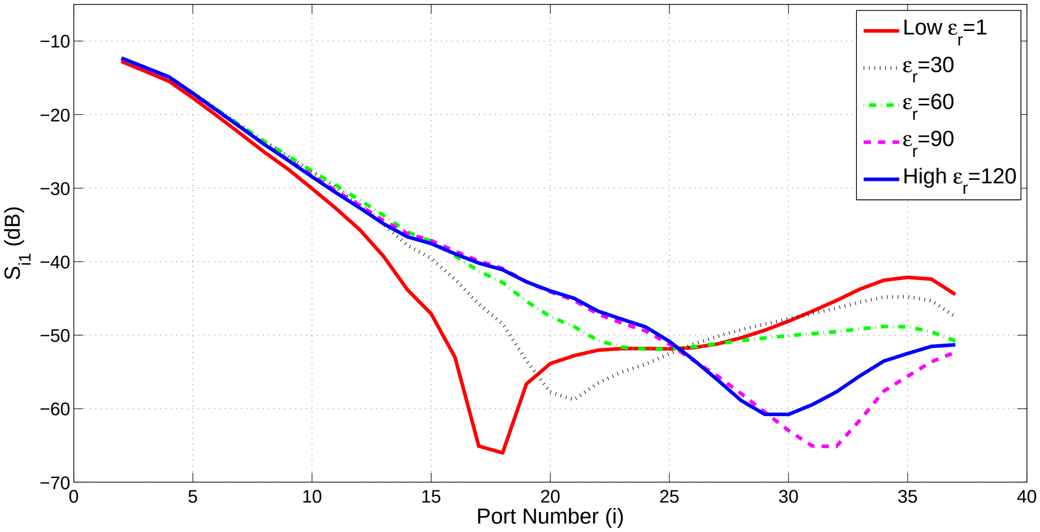

Figure 4.2: Comparison between S_{i1} for different inner layer ϵ_r values

4.1.1 Dielectric Constant Estimation Using LS Method

The dielectric constant can be estimated using Equation (4.1) where w_{i-1} are the weight coefficients, S_{i1} are the transmission coefficients and i is the port number [58]. S_{i1} curves were collected from the simulation model crated in HFSS by varying the ϵ_r inside the inner layer of the chest model from 1 to 120, conductivity from 0.3 to 0.5 and loss tangent from 2 to 3. The resulting data was post processed and a single excel file was made containing all the required information. MATLAB was used to extract the data at 60 MHz only to form a matrix. The resultant overdetermined matrix consisting of 480 rows and 36 columns was solved using the

LS method to obtain the weight coefficients as was done in [59]. Equation (4.2) is then used to get the average ϵ_r from the obtained S_{i1} values via simulations.

$$\epsilon_r = \sum_{i=2}^{37} w_{i-1} S_{i1} \tag{4.1}$$

$$\begin{aligned}\epsilon_r = {} & 6.75S_{2,1} + 12.9S_{3,1} + 16.28S_{4,1} - 16.1S_{5,1} + 6.44S_{6,1} + 16.44S_{7,1} + 5.18S_{8,1} + 17.23S_{9,1} \\ & - 19.34S_{10,1} - 25.78S_{11,1} + 19.72S_{12,1} + 2.31S_{13,1} - 16.64S_{14,1} - 5.04S_{15,1} + 7.02S_{16,1} \\ & - 3.4S_{17,1} + 8.24S_{18,1} + 0.86S_{19,1} + 2.42S_{20,1} - 5.58S_{21,1} + 16S_{22,1} - 22.63S_{23,1} \\ & + 10S_{24,1} + 0.35S_{25,1} + 1.43S_{26,1} - 8.06S_{27,1} - 4.87S_{28,1} + 2.78S_{29,1} - 0.09S_{30,1} \\ & - 0.1S_{31,1} + 0.53S_{32,1} - 1.18S_{33,1} + 8.63S_{34,1} - 8.86S_{35,1} + 4.49S_{36,1} - 1.07S_{37,1}\end{aligned} \tag{4.2}$$

4.1.2 Simulation Results

The ϵ_r values for the normal lung, emphysema and edema conditions are 34.2, 16.9 and 51.2 as stated in [45]. The simulated S_{i1} for normal lung, edema and emphysema conditions are used in (4.2) for ϵ_r estimation. Table 4.2 shows a comparison between exact and simulated ϵ_r values obtained using our RF sensor and human chest model. The maximum simulation error is 1.3% with an average error of 0.57%. This error is due to the weight estimation error using the LS method.

Table 4.2: Comparison of Exact vs simulated ϵ_r for normal human lung and with different diseases.

Category	Exact ϵ_r	Simulated ϵ_r	Simulated Error (%)
Normal Lung	34.2	34.13	0.2
Emphysema	16.9	17.12	1.3
Edema	51.2	51.1	0.2

4.1.3 Textile Substrate Design

The Materials used for the textile substrate design were UV-curable dielectric ink and 85%-15% polyester/cotton textile. The dielectric interface layer is printed by manual screen printing using PET stencil and doctor blade. A dielectric ink thickness of 0.3mm was employed on the textile substrate using PET stencil of 0.3 mm thickness. PET film stencils can be easily and quickly altered using laser-cutting or simple manual carving, thus allowing flexibility during screen printing. The PET stencil is placed on top of the fabric textile as shown in Figure 4.3 and CM116-20 dielectric paste is poured onto the stencil. A squeegee is used to drag the dielectric paste across the stencil. Application force and angles should always be constant. In order to achieve better surface roughness, the same procedure should be performed again but in the opposite direction.

The stencil is removed after the application of the dielectric ink on the textile and the substrate is UV cured for 5 min at $1000 mJ/cm^2$. The textile substrate is placed in an oven for 1 hour at 130°C. The interface layer on textile is dried at room temperature for 1 hour. The available Inkjet printer can print A4 size only, thus the sensor was divided into five parts. One substrate sample of the sensor out of five samples with its dielectric interface is shown in Figure 4.4.

Figure 4.3: PET stencil on textile

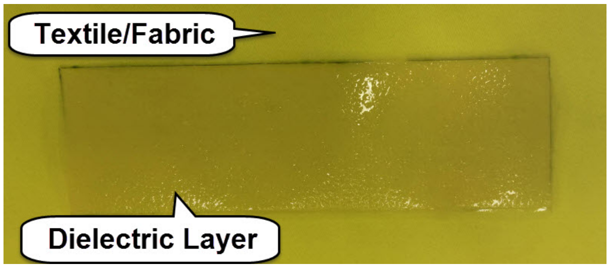

Figure 4.4: Textile substrate sample with dielectric interface

4.1.4 Inkjet Printing

An Inkjet printer is used to print sliver nanoparticle based ink on the textile substrate. The silver organo complex (SOC) ink is used for the printing. Six-conductive layers of the ink are optimal for a conductivity of 1.85×10^6 S/m. The drop spacing of 20 microns was optimized for providing sharp line edges and almost no side overspills. After printing the two layers, heating for 20 minutes at 130°C was applied in a thermal oven.

A small piece of fabric substrate was designed as shown in Figure 4.5, to see the feasibility of Inkjet printing using SOC ink. Six layers printing of a small box model was performed on the designed substrate to see the conductivity of sliver. After every 2 layer printing, 130°C heating was applied for sliver ink curing on the substrate. No conductivity was found after six layer printing due to the rough surface of the designed fabric substrate. The surface roughness is due to the use of available expired dielectric ink for dielectric interface on fabric substrate. Thus an alternate material was examined.

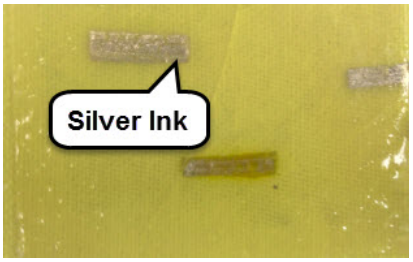

Figure 4.5: Silver SOC ink printing on substrate

4.2 RF Sensor on Polyimide Substrate

The RF sensor consists of 38 electrodes and 37 ports. The first port is excited with 60 MHz RF signal and the remaining 37 ports were terminated with 50 Ω except for the port where the measurement is taken [58]. Biological tissues show significant variation of ϵ_r below 100 MHz [58] so the operating frequency was optimized to 60 MHz. A flexible substrate (polyimide sheet) is used with a thickness of 0.005 cm. The planar sensor was designed using HFSS. The simulations were conducted for the frequency range 1 MHz to 100 MHz with a solution frequency of 60 MHz. The width of first two electrodes is 4 cm and other electrodes have a width of 2 cm. The substrate dimensions were $4.4 \times 89.4 \times 0.005 cm^3$. The size of the sensor is 60% smaller when compared to [45], [58] and 20% smaller than [59]. The first two electrodes were designed to operate at 60 MHz under the best possible matching conditions to perform as the signal exciter. The remaining 36 electrodes receive the radiated fringing fields. The gap between the electrodes was optimized to 0.22

cm. The proposed design of the planner RF sensor with detailed dimensions is shown in Fig. 4.6.

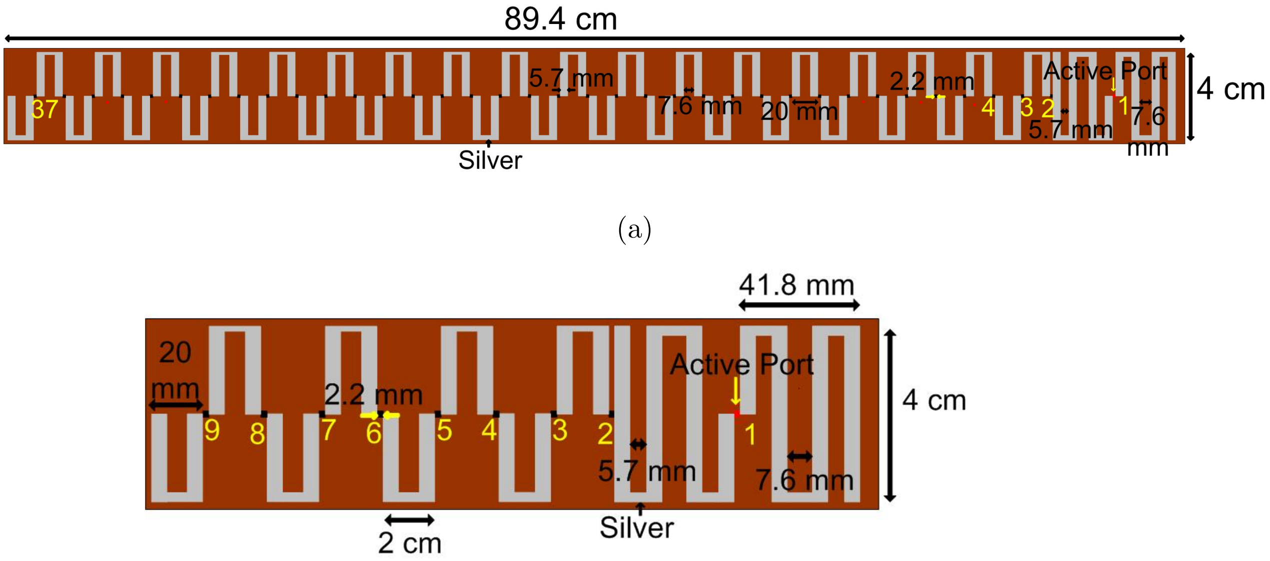

(a)

(b)

Figure 4.6: Proposed design of planner RF sensor (a) complete (b) enlarged view of first ten electrodes.

The sensor was wrapped around an elliptical average adult human chest upper torso model. The upper torso of the human body has a length of 18.29 cm [82]. The perimeter of an average human chest is 89.4 cm (which is also the substrate width of the RF sensor) having an elliptical shape with major radius 16.6 cm and minor radius 11.64 cm [83]. The average thickness of the outer chest layer (skin, fat, muscles and bones) is 1.5 cm [58]. The wrap around design of the proposed RF sensor is shown in Fig. 4.7 (a). The electrical properties of the substrate, FR-4 sheet, Plexiglas base, outer layer and inner layer of the chest model are given in Table 4.3. The dielectric constant, loss tangent and conductivity of the inner layer were varied from 1 to 120, 2 to 3 and 0.3 s/m to 0.5 s/m, respectively to solve the overdetermined system and come up with the weights to estimate the ϵ_r. The transmission coefficients (S_{i1}) were obtained for different ϵ_r values (1, 30, 60, 90, 120) inside the chest where i is the port number. The comparison between S_{i1} curves of different ϵ_r values is shown in Fig. 4.7 (b). The maximum achieved dynamic range between low and high ϵ_r values was 20 dB at port number 17, while the achieved dynamic range in [58] and [59], using ϵ_r values from 1 to 180 was 22 dB for planar or semi planar sensors. The size of the proposed sensor is smaller than [58-59]. There is no need for RF sensor subgrouping as done in [59] which makes the post possessing of the data much simpler. By changing the ϵ_r values, a shift in S_{i1} curves was observed which will improve its accuracy for ϵ_r estimation using the LS method.

Table 4.3: Electrical properties of different meterials used for the design of the RF sensor

Material	Thickness (cm)	Permittivity	Loss Tangent	Conductivity	Reference
Polyimide sheet	0.005	3.4	0.01	-	[84]
FR-4 sheet	0.07874	4.8	0.017	-	[85]
Plexiglas Base	1	2.5	0.08	-	[80]
Outer Layer	1.5	40.6	2.33	0.38	[53], [58]
Inner Layer	31.62	1-120	2-3	0.3-0.5	[58]

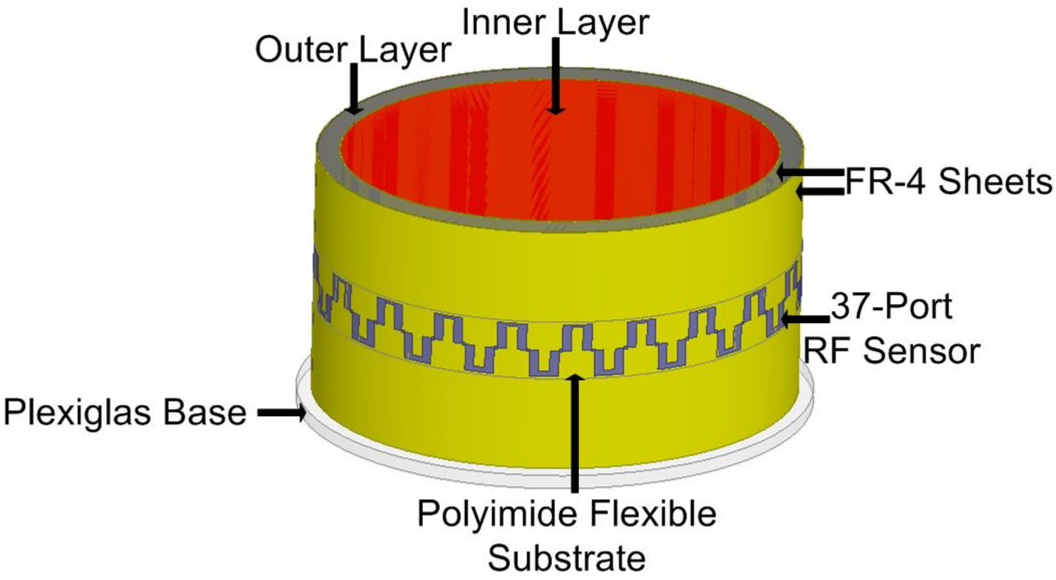

(a)

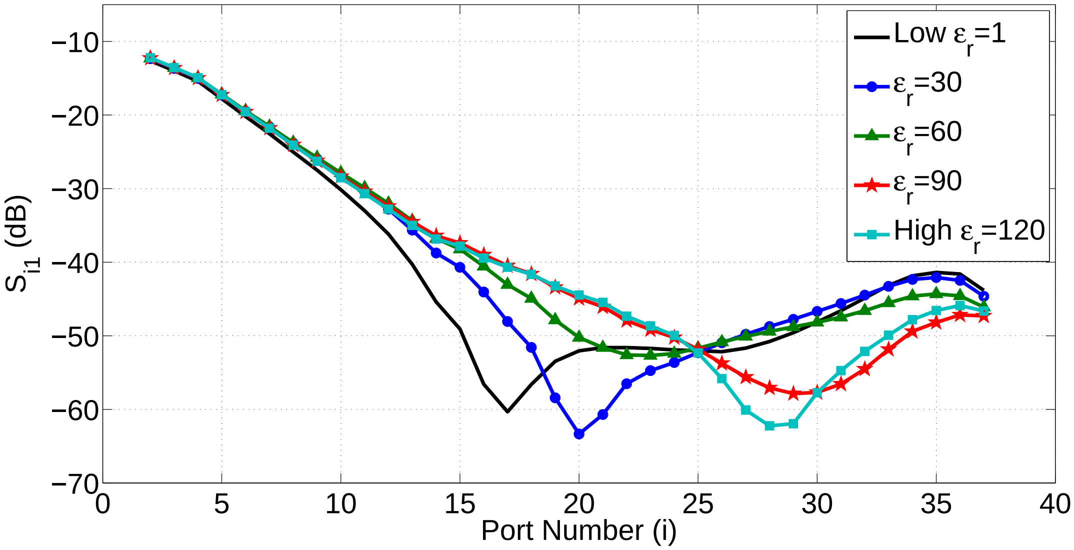

(b)

Figure 4.7: (a) Wrap around design of the proposed RF sensor on an average adult chest model (b) comparison between S_{i1} for different ϵ_r values.

4.2.1 Specific Absorption Rate (SAR)

SAR evaluates the safety limits of a wireless medical device or antenna. The power absorbed by tissues surrounding the antenna/sensor should not exceed standard limits as listed in section 1.4.4. The specific absorption rate of the designed RF sensor is calculated using HFSS. The SAR field for different ϵ_r values are given in Figure 4.8. The maximum value of SAR is always near the first port (source) for all of the cases of ϵ_r variation (1, 30, 60, 90, 108, 120) and the values are far away from FCC and IEEE standards as shown in Table 4.4.

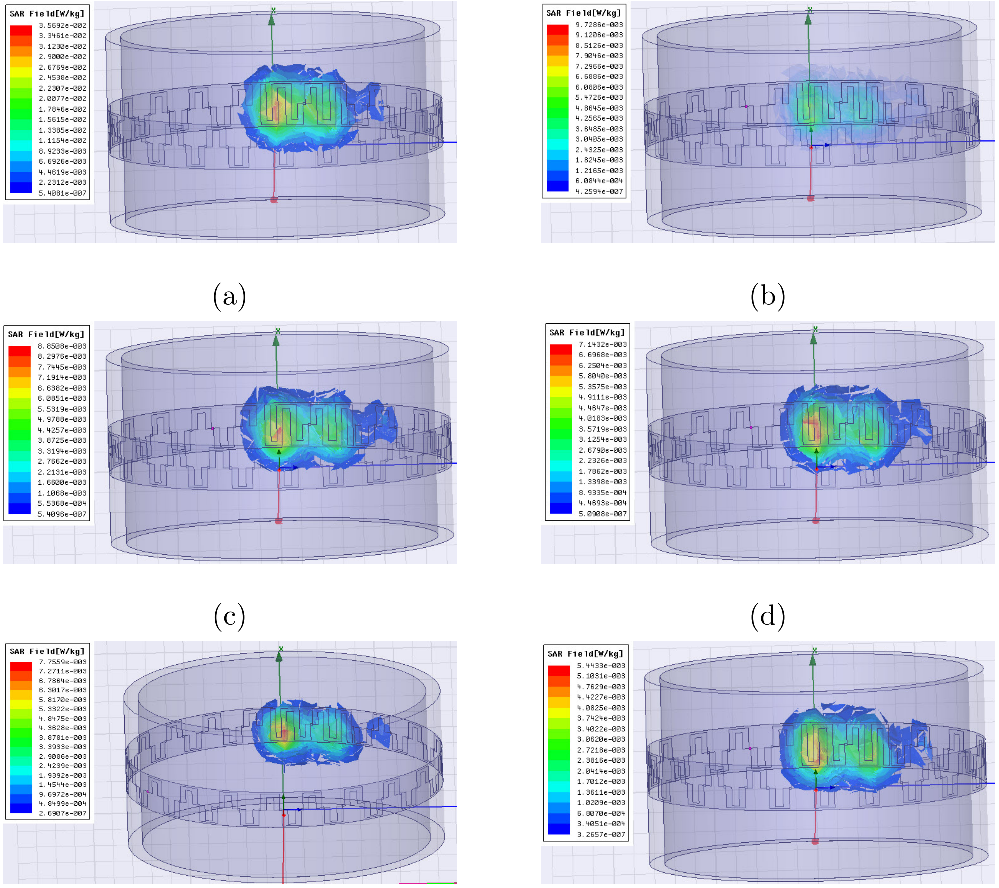

(a) (b)

(c) (d)

(e) (f)

Figure 4.8: SAR fields (a) $\epsilon_r = 1$ (b) $\epsilon_r = 30$ (c) $\epsilon_r = 60$ (d) $\epsilon_r = 90$ (e) $\epsilon_r = 108$ (f) $\epsilon_r = 120$

Table 4.4: SAR Measurements of the proposed design using HFSS

Inner layer ϵ_r	1	30	60	90	108	120
SAR (W/Kg)	0.035692	0.0097286	0.0088508	0.0071432	0.0077559	0.0054433

4.2.2 Sensor Fabrication Using an InkJet Printer

The sensor is fabricated using SOC silver ink in an Inkjet printer. The available printer in IMPACT lab, King Abdullah University of Science and Technology (KAUST), can print A4 size sheets. The sensor is divided into five parts. Figure 4.9 shows the fabrication steps. In the first step, the substrate was washed using Isopropyle Alcohol (IPA) as shown in Figure 4.9 (a). The next step was the drying of the substrate using nitrogen gas as given in Figure 4.9 (b). The UV light curing of the sensor was optimized to two minutes and 30 seconds for SOC ink and 1 minute for ANP ink as shown in Figure 4.9 (c). Increasing the UV time will increase the ink spreading on the substrate. The drop spacing of the SOC and ANP silver ink was optimized to 30 micron. After each of the six layer printing, IR bulb heating for five minutes was used to cure the silver ink on the substrate in case of SOC ink as shown in Figure 4.9 (d). Due to the large size of the substrate, we cannot provide uniform heating on the whole design. For ANP ink printing, three ANP sliver ink layers were printed to achieve good conductivity values. After each layer printing, 10 minute uniform heating is applied at 130°C and after the last layer printing, heating time is increased to 15 minute. The fabricated five parts of the sensor were joined using double sided tape. The fabricated sensor prototype is shown in Figure 4.10 (a). The sensor on a T-shirt is shown in Figure 4.10 (b) to see its flexibility. The final fabricated prototype of the sensor with coaxial probes is shown in Figures 4.10 (c) and (d).

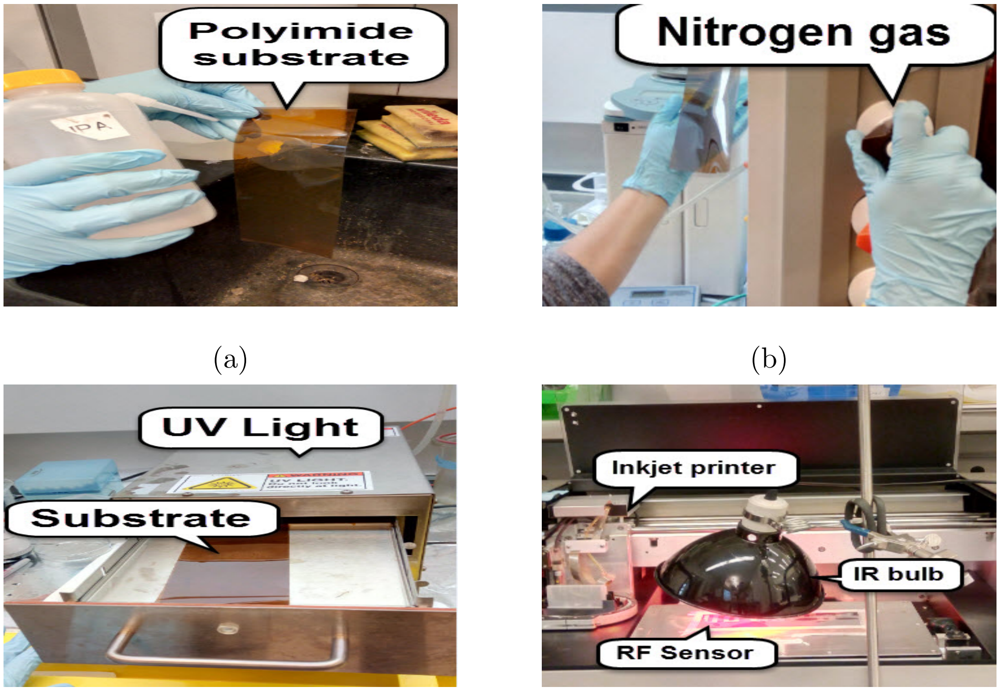

(a) (b)

(c) (d)

Figure 4.9: RF Sensor printing steps (a) Substarate washing with IPA (b) Drying with nitrogen gas(c) UV light curing (d) IR bulb ink curing

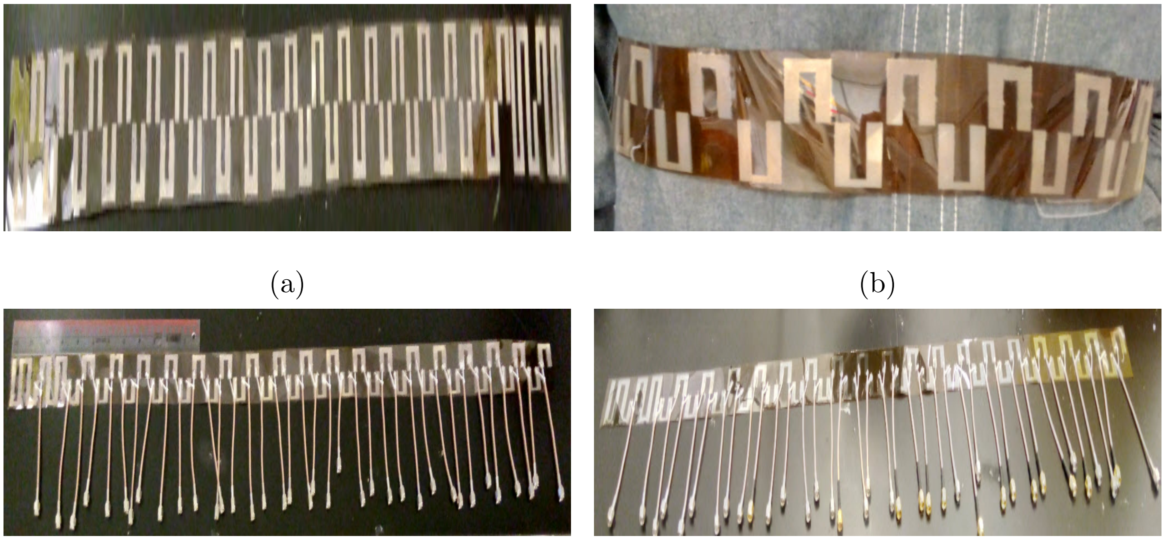

(a) (b)

(c) (d)

Figure 4.10: Fabricated RF sensor (a) without coaxial probes (b) Flexibility of RF sensor on a shirt (c) Scaled RF sensor with 30 cm scale (d) with coaxial probes.

4.2.3 Human Chest Upper Torso Design

The human upper chest torso model was designed in the Fablab at KFUPM, using a computer numerical control (CNC) machine. A Plexiglas sheet of 1 cm in thickness was used for the base. Two elliptical grooves for the outer and inner layers were modeled with 0.5 cm thickness to fix a flexible 0.078 cm FR-4 sheet in it. Super glue was used to join the FR-4 sheets and epoxy glue was used to fix the FR-4 sheets in the grooves. Figure 4.11 (a) shows the Plexiglas base design on the CNC machine with software commands running on the computer. Figure 4.11 (b), (c) and (d) shows the top, front and side views of the designed human upper chest elliptic torso, respectively.

4.2.4 Average Dielectric Constant Estimation

The dielectric constant can be estimated using a similar expression as Equation (4.1) in [58]. S_{i1} curves were collected using HFSS by varying the ϵ_r inside the inner layer of the chest model from 1 to 120, conductivity from 0.3 s/m to 0.5 s/m and loss tangent from 2 to 3. The resultant overdetermined matrix consisting of 480 rows and 37 columns was solved using the LS method to obtain the weight coefficients. Equation (4.3) was used to get the ϵ_r for both simulated and average measured S_{i1} values.

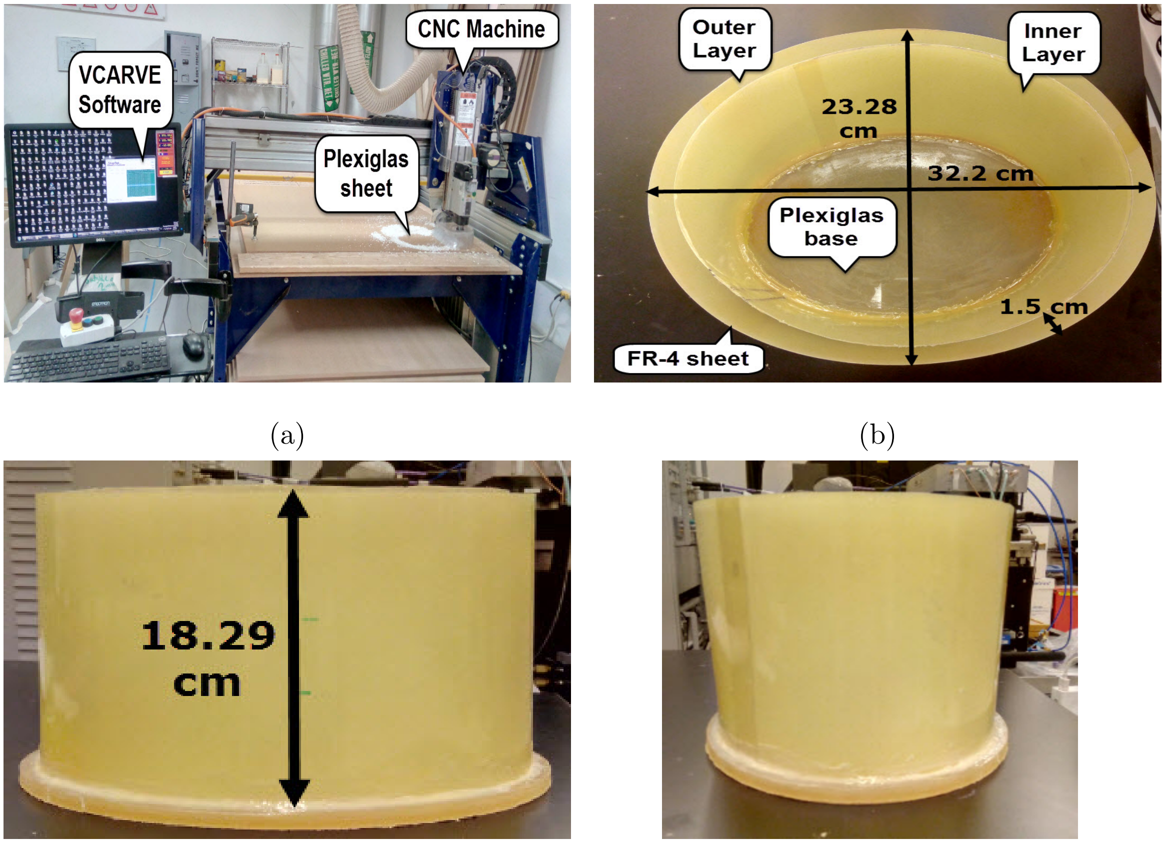

(a) (b)

(c) (d)

Figure 4.11: Human chest upper torso design (a) Plexiglas base design (b) Top view of the designed upper chest torso (c) front view (d) side view.

$$
\begin{aligned}
\epsilon_r = \; & 26.66S_{2,1} - 8.96S_{3,1} + 3.55S_{4,1} + 13.87S_{5,1} - 7.52S_{6,1} - 4.88S_{7,1} + 0.79S_{8,1} - 4.68S_{9,1} \\
& + 4.74S_{10,1} - 9.83S_{11,1} + 15.11S_{12,1} - 13.11S_{13,1} + 11.8S_{14,1} + 3.01S_{15,1} + 12S_{16,1} \\
& - 17.62S_{17,1} + 7.45S_{18,1} - 25.04S_{19,1} + 20.31S_{20,1} + 7.53S_{21,1} - 26.62S_{22,1} + 13.77S_{23,1} \\
& + 5.92S_{24,1} + 0.15S_{25,1} - 2.09S_{26,1} - 0.02S_{27,1} - 3.64S_{28,1} - 10.36S_{29,1} + 14.64S_{30,1} \\
& - 3.78S_{31,1} + 0.01S_{32,1} - 1.32S_{33,1} + 3.76S_{34,1} - 5.96S_{35,1} + 3.32S_{36,1} - 6.29S_{37,1}
\end{aligned}
\tag{4.3}
$$

The designed equation (4.3) was tested on the simulated S_{i1} curves for normal human lung, edema and emphysema infected lung ϵ_r values (stated in [45]) to see the accuracy of the equation. Table 4.5 shows the comparison of the exact vs simulated ϵ_r for normal human lung and infected lung. Equation (4.3) can estimate the ϵ_r of the simulated S_{i1} with an average error of 0.85%. This error is due to estimation of weight coefficient using LS method.

Table 4.5: Comparison of exact vs simulated ϵ_r for normal human lung and with infected lung.

Category	Exact ϵ_r	Simulated ϵ_r	Simulated Error (%)
Normal Lung	34.2	33.74	1.35
Emphysema	19.5	19.47	0.17
Edema	51.2	51.74	1.05

4.2.5 Electrical Properties Measurement Using a Dielectric Assessment Kit (DAK)

A DAK is used to measure the electrical properties (permittivity, loss tangent and conductivity) of any liquid solution. Figure 4.12 (a) shows the measurement setup of DAK. Glycerin is important for breast imaging. Its permittivity can be varied considerably because it is soluble in water. It is non-toxic and ideal from human safety prospective [86]. The human chest outer and different inner layer electrical properties are formed using a mixture of salt, water, IPA and glycerin. The permittivity of the available solutions are measured using the DAK. Figure 4.12 (b) shows the measured dielectric constant for glycerin, water and IPA in the frequency range between 10 MHz to 100 MHz. Due to its low dielectric constant, IPA can be used in the inner layer during the experiments for emphysema case. Different solutions are optimized for normal, edema and emphysema infected human lungs. A 10ml IPA with 80ml glycerin solution is used for a normal human lung. For the edema infected lung, 200ml glycerin, 40ml water and 10g salt mixture is used. Porcine lung properties are formed using a 200ml water with 0.7g salt solution. The salt-water solution was used to increase the permittivity, conductivity and loss tangent values. The human chest outer layer properties are optimized using 70ml IPA, 50ml glycerin, 20ml water and 5g salt solution. The obtained dielectric constant values in the frequency range of 10 MHz to 100 MHz for all these cases are shown in Figure 4.12 (c).

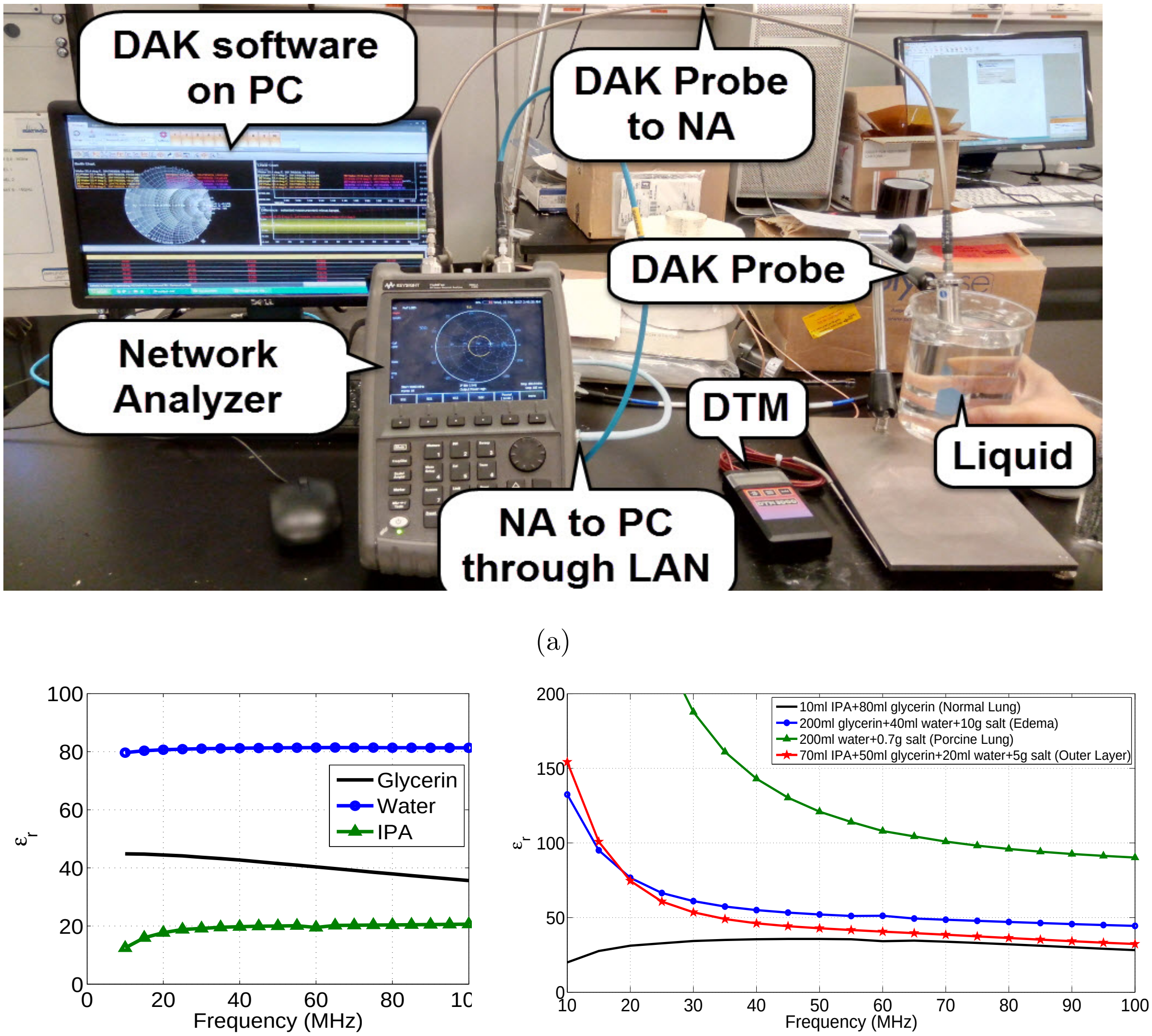

(a)

(b)

(c)

Figure 4.12: (a) Measurement setup of DAK, Electrical properties measurement using DAK (b) Glycerine, water and IPA (Emphysema) (c) Normal lung, Edema, Porcine Lung and outer chest layer .

4.3 Experimental Results of the RF Sensor on Polyimide Substrate Using SOC Ink

The outer layer electrical properties of the human chest are formulated using a mixture of glycerin, water, salt and IPA. A mixture of 1190ml IPA, 850ml glycerin, 340ml water and 85g salt is filled in the outer layer of the upper chest torso. The measured ϵ_r using dielectric assessment kit (DAK) was 40.6 for the outer layer of the chest model. The inner layer of the chest model was filled with the water. The experimental setup for this case is shown in Figure 4.13 (a). The VNA port A is connected with port 1 of the RF sensor (the active port) and VNA port B is switched to other passive ports to collect S_{i1}. Each port reading is taken three times to reduce the measurements inaccuracies and the average measurement is considered for dielectric constant estimation using (4.3). Figure 4.13 (b) shows the comparison of average measured and simulated S_{i1}. The average measured curve is far away from the simulated one.

To confirm the issue of the fabricated sensor, another measurement was conducted for water and salt mixture in the inner layer of the chest model. The 9 liters water with 3.15g of salt is used for this case in inner layer. The obtained ϵ_r is 108 which is similar to porcine lung properties [45]. Figure 4.14 (a) shows the measurement setup for water and salt solution in inner layer of the chest and Figure 4.14 (b) shows the comparison of average measured and simulated S_{i1}. The average measured S_{i1} are not matching with the simulation. Table 4.6 shows a comparison of exact vs simulated and average measured ϵ_r for water only and water+salt solution test. The average measured error is 33.15% which is very high.

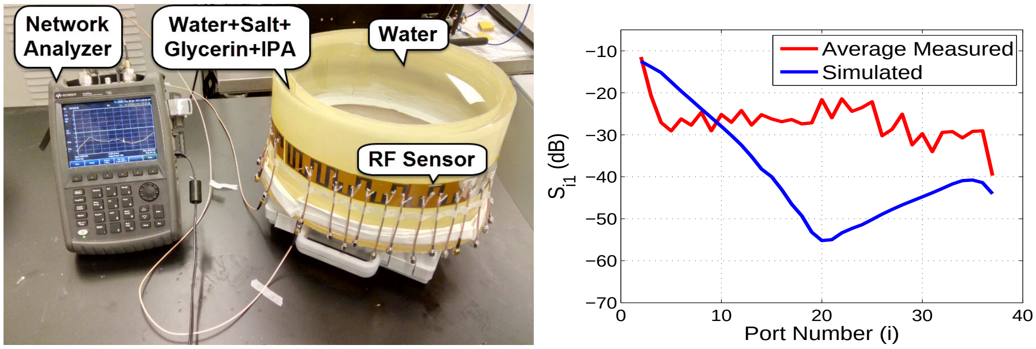

(a) (b)

Figure 4.13: Water test (a) Measurement setup (b) comparison of average measured and simulated S_{i1}.

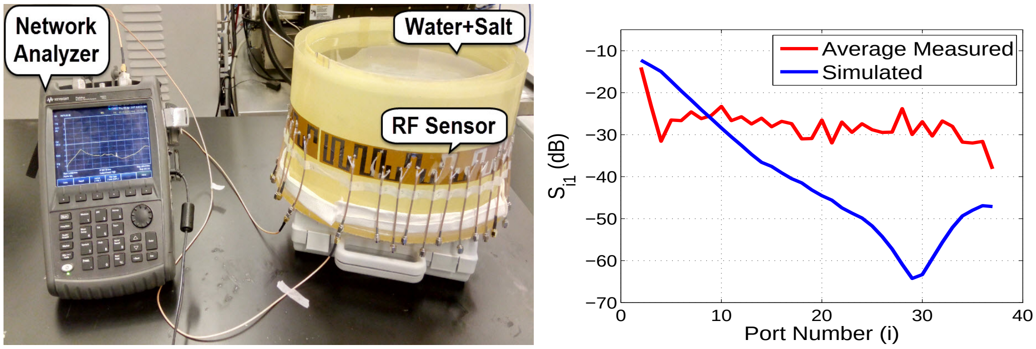

(a) (b)

Figure 4.14: Water and salt solution case (a) Measurement setup (b) comparison of average measured and simulated S_{i1}.

Table 4.6: Comparison of exact vs simulated and average measured ϵ_r for water only and water+salt solution test.

Category	Exact ϵ_r	Simulated ϵ_r	Measured ϵ_r	Simulated Error (%)	Measured Error (%)
Water+Salt	108	109.31	70.12	1.21	35
Water	81	80.34	106.4	0.82	31.3

4.3.1 Investigation of the Results using SOC Ink

The measured S_{i1} curves are far away from the simulated ones. This is due to non-uniform SOC ink printing on polyimide substrate using Inkjet printer. The second reason is the non uniform IR bulb curing of the silver ink. The enlarged view of first electrode is shown in Fig. 4.15 (a) which clearly shows the nonuniform and irregular sliver layers on electrodes using SOC silver ink. Figure 4.15 (b) shows the sensor printing using ANP ink. ANP sliver ink can print uniform ink layers on polyimide substrate.

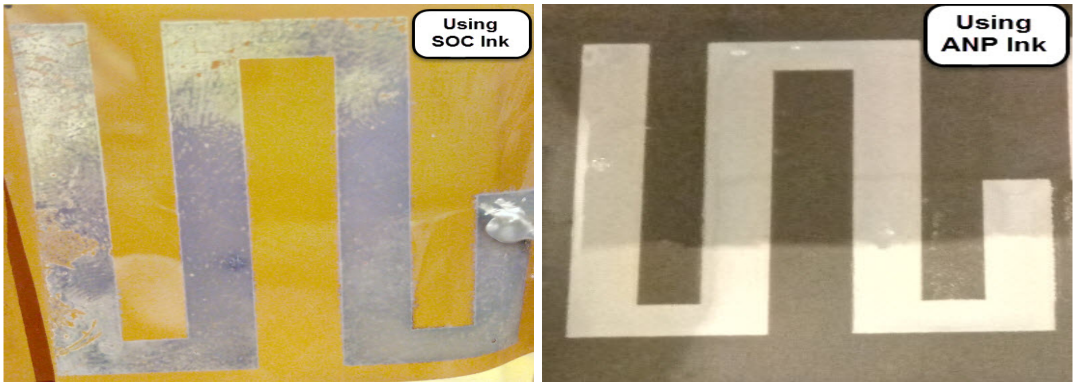

(a) (b)

Figure 4.15: Inkjet Printing (a) using SOC silver ink (b) using ANP silver ink.

4.4 Experimental Results of the RF Sensor on Polyimide Substrate Using ANP Ink

The outer layer electrical properties are formed using a mixture of IPA, salt, water and glycerin. A mixture of 1190ml IPA, 850ml glycerin, 340ml water and 85g salt filled the outer layer of the upper chest torso. The achieved ϵ_r is 40.6 which is the same as stated in [53]. 8000ml glycerin and 1000ml IPA mixture filled the inner layer of the torso with $\epsilon_r = 34.2$ which is similar to a normal lung. Figure 4.16 (a) shows the measurement setup for the normal lung test. Port A of the VNA is connected to the active port and port B is switched to other ports for S_{i1} measurements. Each port measurement was taken three times and the comparison of the average measured and simulated S_{i1} curves for the normal lung case are shown in Figure 4.16 (b). The averaged measured S_{i1} are in good agreement with the simulated ones for the three cases.

IPA filled the inner layer of the torso with $\epsilon_r = 19.5$ for the emphysema case. Figure 4.16 (c) shows the measurement setup for emphysema test. Figure 4.16 (d) shows the comparison of average measured and simulated S_{i1} for the emphysema test. A mixture of 7500ml glycerin, 1500ml water and 375g slat solution filled the inner layer of the chest upper torso with $\epsilon_r = 51.2$ which is similar to the edema case. Figure 4.16 (e) shows the measurement setup for the edema test. Figure 4.16 (f) shows the comparison of average measured and simulated S_{i1} for the edema test. The averaged measured S_{i1} are matching with the simulated ones. Table 4.7 shows the exact, simulated and measured ϵ_r values using (4.3) with an average measured error less than 4.83%. The simulated error is due to LS method weight estimation error.

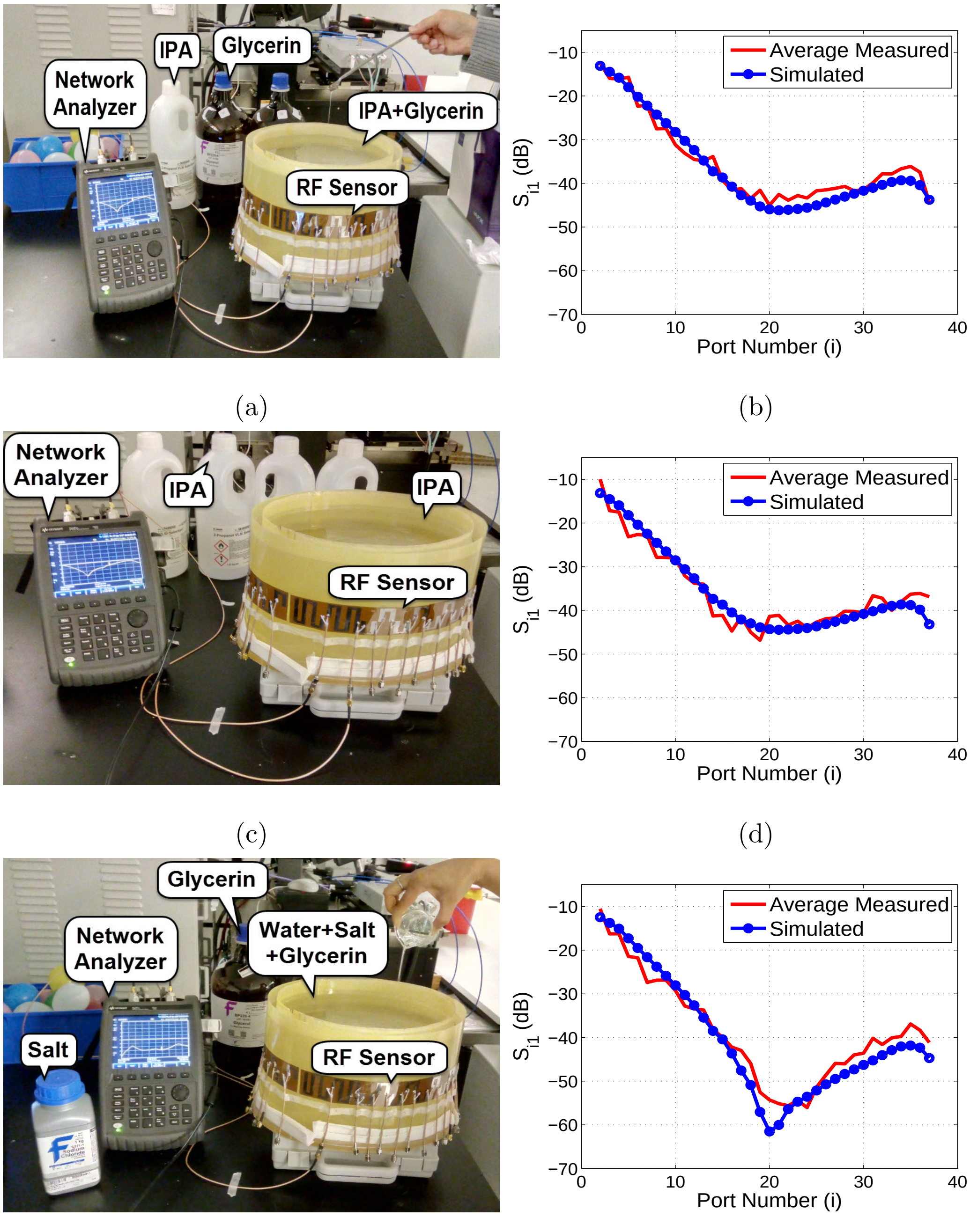

(a) (b)

(c) (d)

(e) (f)

Figure 4.16: (a) Normal lung case measurement setup (b) comparison of average measured and simulated S_{i1} for normal lung case (c) emphysema case measurement setup (d) comparison of average measured and simulated S_{i1} for emphysema case (e) edema case measurement setup (f) comparison of average measured and simulated S_{i1} for edema case

Table 4.7: Comparison of exact vs simulated and average measured ϵ_r for normal human lung and with different diseases.

Category	Exact ϵ_r	Simulated ϵ_r	Measured ϵ_r	Simulated Error (%)	Measured Error (%)
Normal Lung	34.2	33.74	32.99	1.35	3.54
Emphysema	19.5	19.47	18.72	0.17	4
Edema	51.2	51.74	53.67	1.05	4.83

Another test was conducted on a porcine lung (to show applicability of the sensor). The ϵ_r value of the porcine lung is 106.8 [45]. The normal water and salt solution filled the inner layer of the chest upper torso in ratio of 0.7g of salt in 200ml of water. The 9000ml water with 3.15g of salt is used for this case. The obtained ϵ_r was 108 which is similar to the porcine lung. Figure 4.17 (a) shows the measurement setup for the porcine lung case and Figure 4.17 (b) shows the comparison of average measured and simulated S_{i1} for that case. The average measurement is close to the simulation.

To consider different stages of pulmonary edema and making the chest inner layer solutions non-homogeneous, small balloons were filled with water, each with 200ml size. The effective dielectric constant (ϵ_r) of water+salt and water balloons is calculated using (4.4) [19], where d is the volume fraction of water and salt solution, w is the volume of water, $\epsilon_{water+salt}$ is the dielectric constant of water and salt solution with the value of 108 and ϵ_{water} is the dielectric constant of water with a value of 81. Adding six water balls to the inner layer, the obtained average permittivity using (4.4) is 104. Fig. 4.17 (c) shows the measurement setup for the porcine lung case when adding six water balls in its inner layer and Figure 4.17 (d) shows the comparison of average measured and simulated S_{i1} for that case.

The average measurement is in good agreement with the simulated one.

$$\sqrt{\epsilon_r} = d\sqrt{\epsilon_{water+salt}} + w\sqrt{\epsilon_{water}} \tag{4.4}$$

Adding twelve water balls in the inner layer, the calculated average permittivity using (4.4) was 100. Fig. 4.17 (e) shows the measurement setup for the porcine lung case when adding twelve water balls in its inner layer and Figure 4.17 (f) shows the comparison of average measured and simulated S_{i1} for that case. Similarly, adding eighteen water balls, the measurement setup is shown in Figure 4.18 (a) and the comparison of the measured and simulated S_{i1} curves is shown in Figure 4.18 (b). The average measurement is in good agreement with the simulated one for all the cases. Table 4.8 shows the exact, simulated and measured ϵ_r values using (4.3), for all cases of a porcine lung with an average measured error less than 3%. The simulated error is due to the weight estimation error using LS method.

Table 4.8: Comparison of exact vs simulated and average measured ϵ_r for porcine lung with different pulmonary edema stages.

Category	Exact ϵ_r	Simulated ϵ_r	Measured ϵ_r	Simulated Error (%)	Measured Error (%)
Water+Salt	108	109.31	110.89	1.21	2.68
Water+Salt with 6 water balls	104	104.83	104.9	0.79	0.87
Water+Salt with 12 water balls	100	100.3	102.18	0.3	2.18
Water+Salt with 18 water balls	96	96.52	98.69	0.55	2.8

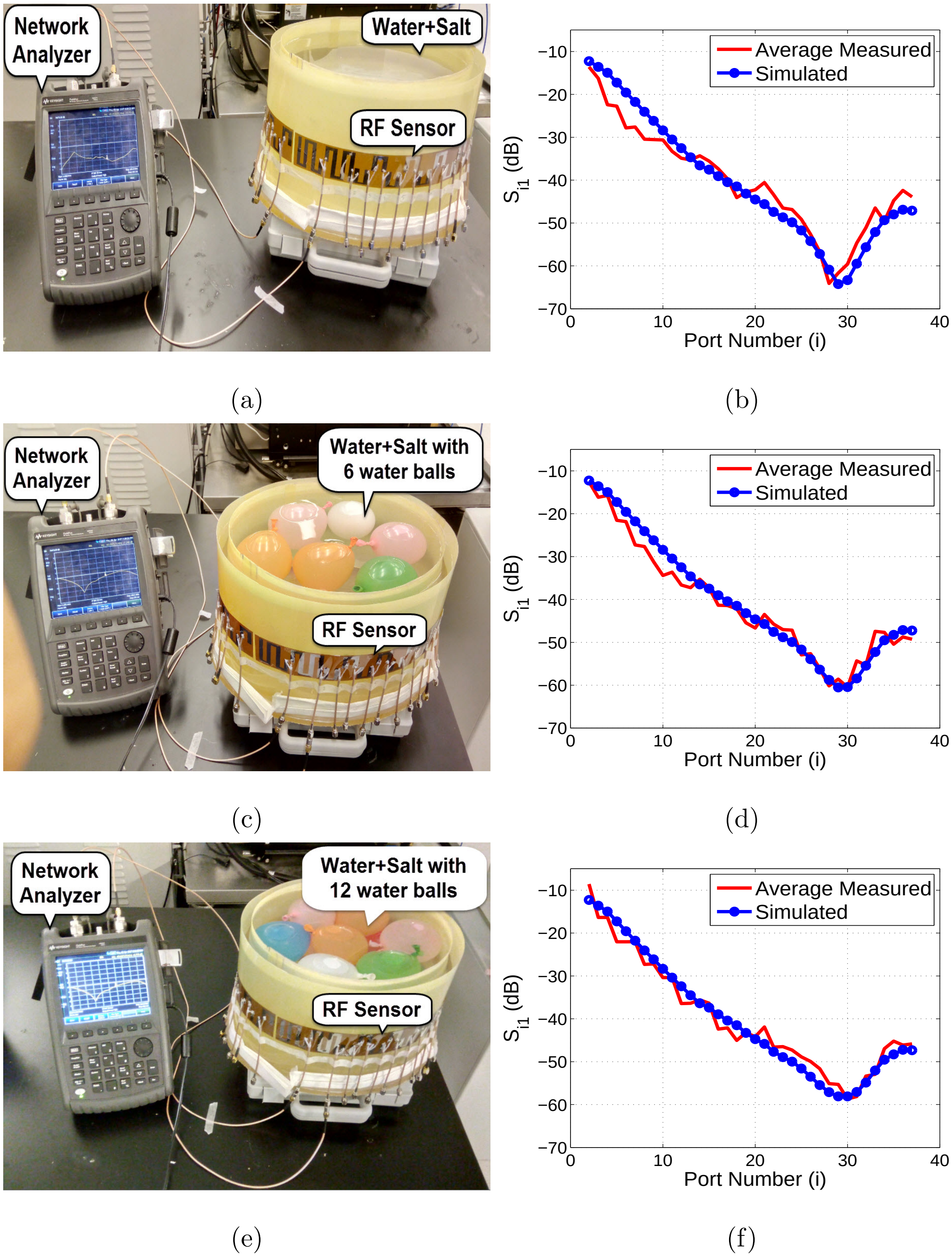

(a) (b)

(c) (d)

(e) (f)

Figure 4.17: (a) Water+salt case measurement setup (b) comparison of average measured and simulated S_{i1} for water+salt case (c) water+salt adding six water balls case measurement setup (d) comparison of average measured and simulated S_{i1} for water+salt adding six water balls case (e) water+salt adding tweleve water balls case measurement setup (f) comparison of average measured and simulated S_{i1} for water+salt adding tweleve water balls case

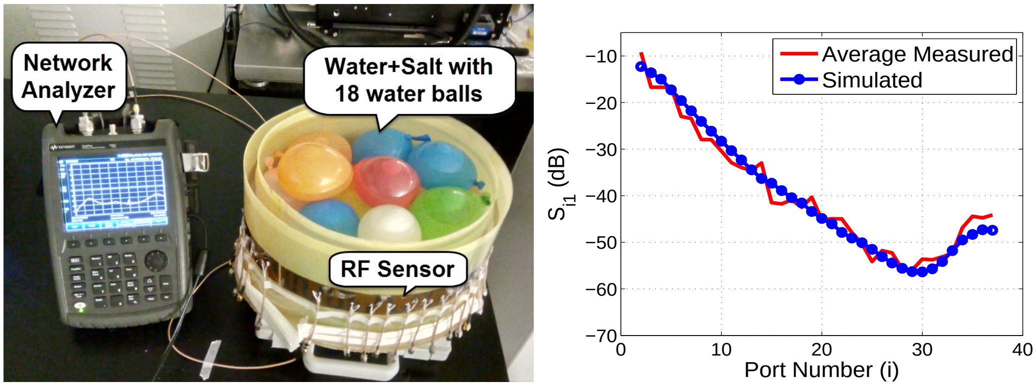

(a) (b)

Figure 4.18: (a) Water+salt adding eighteen water balls case measurement setup (b) comparison of average measured and simulated S_{i1} for water+salt adding eighteen water balls case

4.5 Conclusions

The sensor fabrication on fabric substrate was not possible due to unavailability of dielectric interface ink for the substrate design. The sensor printing on a polyimide substrate using SOC silver ink result in non-uniform printing thus high error percentages in ϵ_r estimation. The sensor was finally build on a flexible polyimide substrate of thickness 0.005 cm using ANP silver ink. It was found that the sensor can estimate the ϵ_r for a human lung (normal, edema infected, emphysema infected) with maximum average error of 4.83%. To differentiate between different stages of pulmonary edema, the inner layer of an elliptical upper torso model was filled with water+salt solution (porcine lung case) and water balls were added to the inner layer with the increment of six water balls. The average error for pulmonary edema stages detection was found to be less than 3%.

CHAPTER 5

CONCLUSIONS

In this work, two flexible, low complex, low RF frequency based sensor arrays for dielectric constant estimation are proposed with two major applications, the first for oil pipes and the other for biomedical applications.

A 28-port RF based low cost, low complexity and non-invasive sensor for average ϵ_r estimation is designed for two/three phase flow measurements. The sensor was build on a AP9131 flexible substrate of $6 \times 27.93 \times 0.01016 cm^3$ size. 2-phase static and 3-phase (static and dynamic) test were conducted. To reduce the measurement inaccuracies, we have conducted each measurement three times and consider the average measured value as final S_{i1} value. It was observed that the average measured S_{i1} curves are very close to the simulated one in all cases. By increasing the number of measurements, the accuracy in dielectric constant estimation can be improved.

For the oil-water case, a reduction in error percentage was observed as the water volume in the pipe increased. The overall error percentage remained below

10% and the average measured error was 5.5%. For the gas-water combination, the measured error percentage was too high when the acrylic pipe was filled with 100% gas which has ϵ_r=1. Since the ϵ_r value is too low the difference in various points will cause a huge error percentage. As the theoretical ϵ_r value increased (the water percentage in acrylic pipe increases), the error percentage starts reducing. The average measured error was 17.3%. If we exclude the 100% gas case then the average measured error becomes 14%. For the gas-oil combination, high measured error percentage in two cases was obtained. This was because of the low ϵ_r values of both gas and oil. For the low ϵ_r values, the high error percentage is expected. It can be noticed that the theoretical and measured ϵ_r values are very close to each other. Our designed sensor can still work for the gas-oil case. The average measured error is 16%.

For 3-phase oil combination, It was observed that as the water volume in the acrylic pipe increased, the error percentage started reducing. The highest error percentage was below 11%. The average measured error was 6.2%. The three phase combination was also tested by adding few drops of a surfactant to make the combination homogeneous. The error percentage for that case was reduced from 9.1% to 4.3%.

For the shake test of the 3-phase oil combination, more variations were observed in measurements in comparison to the static case but still the average measured transmission coefficient values were close to the simulated ones. The overall measured error percentages was below 10% for the four cases investigated and below 15% in case 2.

It was found that the sensor can achieve 9.8% in measured ϵ_r estimation errors with more accurate estimate for high ϵ_r combinations. The shake test for the 3-phase combinations of oil-water-gas showed average measured error of 9.3%. This is the first low complexity sensor that provide accurate ϵ_r estimation with less than 10% average errors across its dynamic range and works with (was tested for) 2-phase, 3-phase static cases and 3-phase shaked up scenarios.

An RF based low cost, low complexity and non-invasive wearable sensor for average ϵ_r estimation was proposed for pulmonary edema monitoring. A 37-port Inkjet printed using ANP silver ink RF based low complexity, low cost and non-invasive human chest sensor for ϵ_r estimation of different lung diseases that can be integrated with cloths easily is designed. The sensor was build on a flexible polyimide substrate of thickness 0.005 cm. It was found that the sensor can estimate the ϵ_r for a human lung (normal, edema infected, emphysema infected) with maximum average error of 4.83%. To differentiate between different stages of pulmonary edema, the inner layer of an elliptical upper torso model was filled with water+salt solution (porcine lung case) and water balls were added to the inner layer with the increment of six water balls. The average error for pulmonary edema stages detection was found to be less than 3%.

5.1 Future Work

In future work, we will consider the idea of a complete multiphase flow volume fraction measurements system. The complete system idea is given in Fig. 5.1 in which RF sensor first port is directly connected to the VNA port 1. The remaining ports of RF sensor are connected with VNA port 2 using RF switch. A PC control is connected to both RF switch and VNA. Using the RF switch, the ports will connect sequentially to VNA through PC control. Using this system, the measurement time will reduce as there is no need to connect each port individually to VNA and sensor. So, we can extend the experiments for more cases of multiphase combination in flow condition. Also, by taking the average of 100 measurement instead of three, the accuracy of sensor will significantly improve.

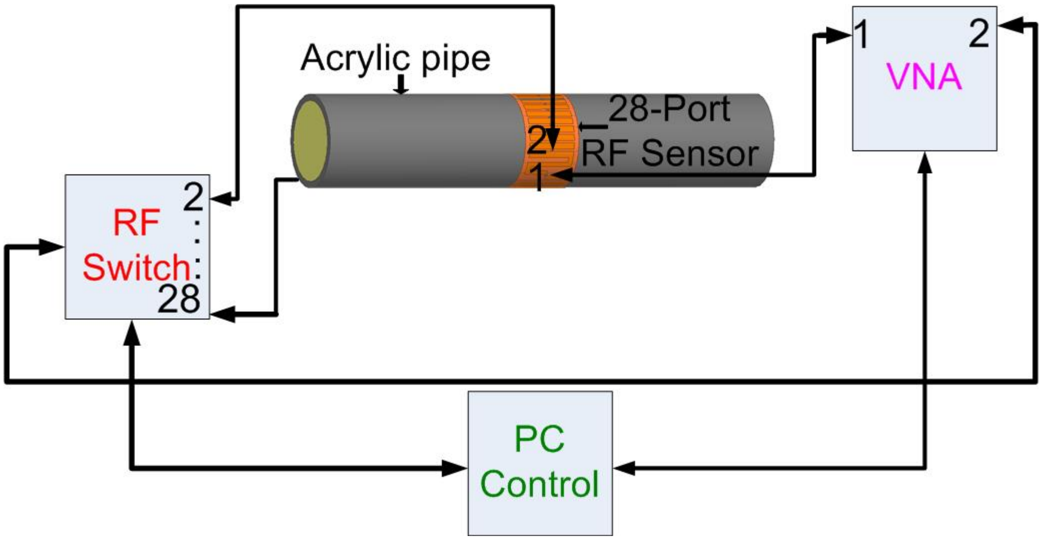

Figure 5.1: Idea of a complete system

For the biomedical sensor, the RF sensor array can be connected via bluetooth to a data collection device (cell phone) using microcontroller and RF switch. The collected data can be transferred wirelessly using body area network (BAN) to a post processing unit. The post processing unit estimates the dielectric constant based on the retrieved transmission coefficients values and provide the patient real time and continuous health information to his/her health care provider (Doctor).

REFERENCES

[1] B. K. Arvoh, R. Hoffmannb and M. Halstensen, "Estimation of volume fractions and flow regime identification in multiphase flow based on gamma measurements and multivariate calibration", Flow Measurement and Instrumentation Elsevier journal, pp. 56-65, 2012.

[2] Corneliussen, Sidsel, Couput, J. Paul, Dahl and Eivind, "Handbook of Multiphase Flow Metering", Revision 2, pp. 36-53, March 2005.

[3] Ismail, J.C. Gamio, S.F.A. Bukhari and W.Q. Yang, "Tomography for multiphase flow measurement in the oil industry", Flow Measurement and Instrumentation Elsevier, pp. 145155, 2005.

[4] S. L. Ashton, N. G. Cutmore, G. L. Roach, J. S. Watt, R. W. Zastawny and A. J. McEwan, "Development and trial of microwave techniques for measurement of multiphase flow of oil, water and gas", Proc. SPE Asia Pacific Oil and Gas Conf. (Melbourne, Australia) (Society of Petroleum Engineers), 1994.

[5] S. Gainsford and R. Hide, "Field testing of the multi-fluid LP multiphase meter", Proc. 11th North Sea Flow Measurement Workshop (Norway), 1993.

[6] B. Hogan, A. I. AI-Shamma and J. Lucas, "Real-Time Multiphase Metering Using Non-Intrusive Microwave Sensor", 2nd North American Conference on Multiphase Technology, (ISBN 1-86058252-4), pp. 281-96, 2000.

[7] E. Dykesteen, A. Hallanger, E. A. Hammer, E. Samnoy and R. Thorn, "Nonintrusive three component ration measurement using an impedance sensor", J Phys.Sci. Instrum. 18, pp. 540-44, 1985.

[8] G. L. Kruger, A. Birke and R. Weiss, "Nuclear magnetic resonance (NMR) two phase mass", 1996.

[9] A. Bonfiglio and D. D. Rossi, "Wearable Monitoring Systems", New York, USA, Springer, 2011.

[10] R. Paradiso, G. Loriga and N. Taccini, "A wearable health care system based on knitted integrated sensors", IEEE Trans. Technol. Biomed, vol. 9, no. 3, pp. 337-345, 2005.

[11] S. Salman, "A Wearable Real-Time and Non-Invasive Thoracic Cavity Monitoring System", PHD Thesis, The Ohio State University, 2015.

[12] A. Adlert, Y. Berthtaume, R. Guardo and R. Amyo, "Imaging of pulmonary edema with electrical impedance tomography", IEEE-EMBC and CMBEC, pp. 557-558, 1995.

[13] A. V. Shahidi, R. Guardo and P. Savard, "On the Monitoring of Pulmonary Edema by Impedance Tomography", IEEE conference, 1994.

[14] S. A. Rezaeieh and A.M. Abbosh, "Review of Systems for the Detection and Monitoring of Accumulated Fluids in the Human Torso", IEEE ISAP, 2015.

[15] S. N. Narouze, "Atlas of Ultrasound-Guided Procedures in Interventional Pain Management", Springer, 2011.

[16] P. M. Meaney, P. A. Kaufman, L. S. Muffly, M. Click, S. P. Poplack, W. A. Wells, G. N. Schwartz, R. M. d. F. Alexander, T. D. Tosteson, Z. Li, S. D. Geimer, M. W. Fanning, T. Zhou, N. R. Epstein and K. D. Paulsen, "Microwave imaging for neoadjuvant chemotherapy monitoring: initial clinical experience", Breast Cancer Research, (in press).

[17] C. A. Balanis, "Advance Engineering Electromagnetic", 2nd edition, pp. 41-47, 2012.

[18] J. W. M. Rogers and C. Plett, "Radio frequency integrated circuit design", 2nd edition, pp. 126-128, 2010.

[19] N. Xie, H. Zhang, S. Gao and W. Chen, "Research of Measuring Instrument for Water-in-oil Percentage with Capacitance Sensor", IEEE The 1st International Conference on Information Science and Engineering (ICISE2009), pp.5030-5032, 2009.

[20] S. Salman, D. Psychoudakis and J. L. Volakis, "Determining the Relative Permittivity of Deep Embedded Biological Tissues", IEEE transactions on Antennas and Propagation vol. 11, pp. 1694-1697, 2012.

[21] G. Strang, "Linear Algebra and its Application", 4th edition, pp. 161-170, 2006.

[22] M. Khabiri, "Design and Simulation of Implantable PIFA in Presence of ANSYS Human Body Model for Biomedical Telemetry Using ANSYS HFSS", OZEN Engineering, Inc., pp. 1-11.

[23] C. N. Strizzolo and J. Converti, "Capacitance Sensors for Measurement of Phase Volume Fraction in Two-Phase Pipelines", IEEE transection on instrumentation and measurement, vol. 42, no. 3, pp. 726-729, June 1993.

[24] W. H. Ahmed, "Capacitance Sensors for Void-Fraction Measurements and Flow-Pattern Identification in AirOil Two-Phase Flow", IEEE sensor journal, vol. 6, no. 5, pp. 1153-1163, October 2006.

[25] M. Z. Aslam and T. B. Tang, "A High Resolution Capacitive Sensing System for the Measurement of Water Content in Crude Oil", Sensor Journal, pp. 11351-11361, 2014.

[26] E. J. Mohamad, R. A. Rahim, L. P. Ling, M. H. F. Rahiman, O. M. F. B. Marwah and N. M. N. Ayob, "Segmented Capacitance Tomography Electrodes: A Design and Experimental Verifications", IEEE sensor journal, vol. 12, no. 5, pp. 1589-1598, May 2012.

[27] S. K. Aggarwak and R. H. Johnston, "Oil and Water Content Measurement of Sandstone Cores Using Microwave Measurement Techniques", IEEE transaction on instrumentation and measurements, vol. im-35, no.4, pp. 630-637, December 1986.

[28] S. I. Sheikh, H. A. Ragheb, K. Y. Alqurashi and I. Babelli, "A Microwave Technique for Detecting Water Deposits in an Air Flow Pipelines", ACES Journal, vol. 25, no. 7, pp. 647-651, July 2010.

[29] Y. S. A. AlFaouri, "Microwave Technique for monitoring fluid level in horizontal petroleum carrying pipelines", PHD thesis KFUPM, April 2014.

[30] S. I. Sheikh, K. Y. Alqurashi, H. A. Ragheb and I. Babelli, "Simple microwave method for detecting water holdup", Wiley Microwave and optical technology letters, Vol. 50, no. 2, , pp. 354-355, February 2008.

[31] H. E. D. L. vila, D. J. Pagano and F. R. D. Sousa, "Water Fraction Measurement Using a RF Resonant Cavity Sensor", 19th Symposium IMEKO TC 4 Symposium and 17th IWADC Workshop Advances in Instrumentation and Sensors Interoperability Barcelona, Spain, pp. 281-285, July 2013.

[32] S. Al-Hajeri, S. R. Wylie, A. Shaw and A. I. Al-Shamma, "Real Time EM Waves Monitoring System for oil Industry Three Phase Flow Measurement", Journal of Physics Sensors and their Applications XV, pp. 1-6, 2009.

[33] S. Rwylie, A. Shaw and A. I. Al-Shamma, "RF sensor for multiphase flow measurement through an oil pipeline", Measurement science and technology, pp. 21412149, 2006.

[34] M.A. Al-Kizwini, S.R. Wylie, D.A. Al-Khafaji and A.I. Al-Shamma, "The monitoring of the two phase flow-annular flow type regime using microwave sensor technique", Flow Measurement and Instrumentation journal Elesiver, pp. 45-51, 2013.

[35] H. E. D. L. Avila, D. J. Pagano and F. R. D. Sous, "Improving the performance of an RF resonant cavity water-cut meter using an impedance matching network", Flow Measurement and Instrumentation journal Elesiver, pp. 14-22, 2015.

[36] V. R. Bom, M. C. Clarijsl and W.E. V. Eijk, "Accuracy Aspects in Multi Phase Flow Metering using X-ray Transmission", IEEE Journal, pp. 125-128, 2001.

[37] V. R. Bom, M. C. Clarijs, C. W. E. van Eijk, Z. I. Kolar and L. M. Scheers, "The Optimal X-Ray Energy Problem in Multi-Phase Flow Metering", IEEE transaction on nuclear science, vol. 50, no. 3, pp. 718-722, June 2003.

[38] A. M. Scheers and W. F. J. Slijkerman, "Multiphase flow measurement using multiple energy gamma ray absorption measurement", Denver, CO, SPE 36 593, October 1995.

[39] H. V. Santen, Z. Kolar, and A. M. Scheers, "Photon selection for dual energy gamma and/or X-ray absorption composition measurement in oil/water/gas mixtures", Nucl. Geophys, vol. 9, no. 3, pp. 193-202, 1995.

[40] V. R. Bom, M. C. Clarijs, C. W. E. V. Eijk, Z. I. Kolar, J. Frieling, A. M. Scheers, and G. Miller, "Accuracy aspects in multiphase flow metering using X-ray transmission", in Proc. Conf. IEEE, vol. 1(1008), Lyon, France, 2000.

[41] S. Gehrke and K. Wirth, "Application of Conventional- and Dual-Energy X-Ray Tomography in Process Engineering", IEEE sensor journal, vol. 5, no. 2, pp. 183-187, April 2005.

[42] Y. Li and W. Yang, "Measurement of multi-phase distribution using an integrated dual-modality sensor", Imaging Systems and Techniques, IEEE International Workshop , May 2009.

[43] B. T. Hjertaker, S. Tjugum, E. A. Hammer and G. A. Johansen, "Multimodality Tomography for Multiphase Hydrocarbon Flow Measurements", IEEE sensor journal, vol. 5, no. 2, pp. 153-160, April 2005.

[44] M. Wang , J. Jia, Y. Faraj, Q. Wang, C. Xie, G. Oddie, K. Primrose and C. Qiu, "A new visualisation and measurement technology for water continuous multiphase flows", Flow Measurement and Instrumentation, volume 46, pp. 204-212, 2015.

[45] S. Salman, Z. Wang, E. Colebeck, A. Kiourti, E. Topsakal and J. L. Volakis, "Pulmonary Edema Monitoring Sensor With Integrated Body-Area Network for Remote Medical Sensing", IEEE Transaction on antenna and propagation, vol. 62, no. 5, pp. 2787-2794, May 2014.

[46] T. Yilmaz, T. Karacolak, and E. Topsakal, "Characterization and testing of a skin mimicking material for implantable antennas operating at ISM band (2.4 GHz-2.48 GHz)", IEEE Antennas and Wireless Propagation Letters, vol. 7, pp. 418-420, 2008.

[47] M. V. Dancsisin, "Characterization of Tissue Mimicking Materials for Testing of Microwave Medical Devices", M.S. Thesis, MSU, Starkville, MS, 2011.

[48] P. C. Pedersen, C. C. Johnson, C. H. Durney and D. G. Bragg, "Microwave Reflection and Transmission Measurements for Pulmonary Diagnosis and Monitoring", IEEE transaction on biomedical engineering, vol. BME-25, no. 1, pp. 40-48, January 1978.

[49] N. Celik, R. Gagarin, H. Youn and M. F. Iskander, "A Noninvasive Microwave Sensor and Signal Processing Technique for Continuous Monitoring of Vital Signs", IEEE antenna and wireless propagation letters, vol. 10, pp. 286-289, 2011.

[50] S. Salman and J. L. Volakis, "An In-vivo Electrical Property Based Health Monitoring Sensor", 7th European Conference on Antennas and Propagation, pp. 785-786, EUCAP 2013.

[51] R. Gagarin, G. C. Huang, N. Celik and M. F. Iskander, "Determination of Pulmonary Edema Using Microwave Sensor Array: Simulation Studies With Anatomically Realistic Human CAD-Models", IEEE Conference on Antennas and Propagation APS, pp. 2189-2190, 2013.

[52] S. Salman, A. Kiourti and J. L. Volakis, "An On-Body Wrap-Around Sensor for Monitoring Changes in Lung Permittivity", IEEE Conference, 2014.

[53] M. A. Islam, A. Kiourti and J. L. Volakis, "A Novel Method of Deep Tissue Biomedical Imaging Using a Wearable Sensor", IEEE Sensors Journal, pp. 1-7, 2015.

[54] M. A. Islam, A. Kiourti and J. L. Volakis, "A Novel Body-Worn RF Sensor for Deep Tissue Imaging", IEEE Conference, pp. 43-44, 2015.

[55] S. Salman, L. Z. Lee and J. L. Volakis, "An In-vivo Wrap-Around Permittivity Sensor for Deep Biological Tissue Monitoring", IEEE Conference APS, pp. 2054, 2013.

[56] S. Salman, D. Psychoudakis and J. L. Volakis, "Determining the Relative Permittivity of Masses in the Human Body", IEEE conference, 2012.

[57] S. Salman, A. Kiourti and J. L. Volakis, "Rudimentary Deep Tissue Imaging Through a Wearable Real-Time Monitoring System", IEEE Conference APS, pp. 1194, 2015.

[58] S. Salman, D. Psychoudakis and J. L. Volakis, "Determining the Relative Permittivity of Deep Embedded Biological Tissues", IEEE antenna and wireless propagation letters, vol. 11, pp. 1694-1697, 2012.

[59] S. Salman, Lanlin Z. Lee and J. L. Volakis, "A Wearable Wrap-Around Sensor for Monitoring Deep Tissue Electric Properties", IEEE sensor journal, vol. 14, no. 8, pp. 2447-2451, August 2014.

[60] Z. Wang, A. Kiourti, M. H. Zhang, L. Z. Lee and J. L. Volakis, ”A Wireless Communication System for Remote Medical Monitoring”, IEEE Conference URSI, pp. 211, 2013.

[61] K. Karathanasis, A. Kiourti and J. L. Volakis, ”A Wireless Body Area Network for Carefree Medical Sensing”, IEEE Conference APS, pp. 317, 2014.

[62] S. A. Rezaeieh, A. Abbosh and M.A. Antoniades, ”Broadband UHF Antenna for Heart Failure Detection System”, IEEE Conference on Antennas and Propagation APS, pp. 2089-2090, 2013.

[63] S. A. Rezaeieh, K. S. Bialkowski and A. M. Abbosh, ”Microwave System for the Early Stage Detection of Congestive Heart Failure”, IEEE special section on Bio-compatible materials and Bio-Electromagnetics for Bio-medical applications, volume 2, pp. 921-929, 2014.

[64] P. Nepa and H. Rogier, ”Wearable Antennas for Off-Body Radio Links at VHF and UHF Bands Challenges, the state of the art and future trends below 1 GHz”, IEEE Antennas and Propagation Magazine, pp. 30-52, October 2015.

[65] C. Liu, Y. X. Guo and S. Xiao, ”A Review of Implantable Antennas for Wireless Biomedical Devices”, Forum for Electromagnetic research methods and application technologies (FERMAT) .

[66] J. Moll, J. Vrba, I. Merunka, O. Fiser and V. Krozer, "Non-Invasive Microwave Lung Water Monitoring: Feasibility Study", Dept. of Biomedical Technology, Czech Technical University in Prague.

[67] M. A. Karimi and A. Shamim, "A flexible inkjet printed antenna for wearable electronics applications", IEEE conference APS, pp. 1935-1936, 2016.

[68] J. Trajkovikj and A. K. Skrivervik, "Comparison of SAR of UHF Wearable Antennas", EUCAP Davous, Switzerland, pp. 10-15, April 2016.

[69] M. Radai, H. Krief, T. Engelman and S. Abboud, "A novel telemedicine system for monitoring congestive heart failure patients", International Conference on Information Technology: Research and Education, pp. 45, 2006.

[70] N. Singh, A. K. Singh and V. K. Singh, "Design and performance of wearable ultrawide band textile antenna for medical applications", Wiley Microwave and optical technology letters, vol. 57, no. 7, pp. 1553-1557, July 2015.

[71] P. F. Silva, R. C. S. Freire, A. J. R. Serres, P. H. da F. Silva and J. C. Silva, "Wearable textile bioinspired antenna for 2G, 3G, and 4G systems", Wiley Microwave and optical technology letters, vol. 58, no. 12, pp. 2818-2823, December 2016.

[72] S. Salman, Z. Wang, A. Kiourti, E. Topsakal and J. L. Volakis, "A Non-Invasive Lung Monitoring Sensor with Integrated Body-Area Network", IEEE MTT-S International Microwave Workshop Series on RF and Wire-

less Technologies for Biomedical and Healthcare Applications (IMWS-BIO), 2013.

[73] L. Zhang, Z. Wang and J. L. Volakis, "Textile Antennas and Sensors for Body-Worn Applications", IEEE antenna and wireless propagation letter, VOL. 11, pp. 1690-1693, 2012.

[74] A. Kiourti and J. L. Volakis, "Colorful Textile Antennas Integrated into Embroidered Logos", Journal of Sensor and Actuator Networks, pp. 371-377, 2015.

[75] L. Zhang, Z. Wang, S. Salman and J. L. Volakis, "Embroidered Textiles for RF Electronics and Medical Sensors", IEEE Conference, 2012.

[76] A. Kiourti, C. Lee and J. L. Volakis, "Fabrication of Textile Antennas and Circuits With 0.1 mm Precision", IEEE antenna and wireless propagation letters, vol. 15, pp. 151-153, 2016.

[77] A. Kiourti and J. L. Volakis, "Wearable Antennas Using Electronic Textiles for RF Communications and Medical Monitoring", ElectroScience Laboratory, Dept. of Electrical and Computer Engineering, The Ohio State University, Columbus, OH, USA.

[78] R. R. G. Perron, G. C. Huang and M. F. Iskander, "Textile Electromagnetic Coupler for Monitoring Vital Signs and Changes in Lung Water Content", IEEE antenna and wireless propagation letters, vol. 14, pp. 151-154, 2015.

[79] Data-sheet, "DuPont Pyralux AP flexible circuit materials", Technical Data-sheet.

[80] Acrylic Pipe, "General information and physical properties of Plexiglas acrylic sheet", Technical data-sheet.

[81] S. Salman, L. Z. Lee and J. L. Volakis, "A Wearable Wrap-Around Sensor for Monitoring Deep Tissue Electric Properties", IEEE sensor journal, vol. 14, no. 8, pp. 2447-2451, August 2014.

[82] E. P. Hanavan, "A mathematical model of the human body", Behavioral science laboratory, Air force base, Ohio, Oct 1964.

[83] Available online, "https://msis.jsc.nasa.gov/sections/section03.htm"

[84] Available online, "http://www.goodfellow.com/A/Polyimide-Film.html"

[85] Available online, "http://www.americanepoxy.com/g10-fr4-datasheet.html"

[86] P. M. Meaney, C.J. Fox, S. D. Geimer, et al., "Electrical Characterization of Glycerin: Water Mixtures: Implications for Use as a Coupling Medium in Microwave Tomography", IEEE transaction on microwave theory and techniques, pp. 1-8, 2017.

Vitae

Muhammad Tayyab received his BSc degree in Electrical Engineering from University of the Punjab, Lahore, Pakistan in 2012. He received Gold Medal award for obtaining first position in his BSc degree. Right after the graduation, he joined Wi-tribe Pakistan Limited, a multi-national cellular operator, as a Radio Frequency Planning and Optimization Executive and served for more than 2 years till 2015. During his stay at Wi-tribe, he received Star Champion award in his first year of work and Outstanding performance award in his second year of work at Wi-tribe. He also served Ministry of Finance, Pakistan, as a Technical Training Coordinator for three months in 2015. He started his MSc degree in Electrical Engineering, King Fahd University of Petroleum and Minerals (KFUPM), Saudi Arabia, in 2015. During his stay at KFUPM, he had associated with King Abdullah University of Science and Technology (KAUST), Saudi Arabia, as a visiting student and worked on KFUPM-KAUST joint research initiative. His research interests include, RF sensor arrays design for the diagnosis of human chest diseases and RF sensor arrays design for the multiphase flow measurements in oil industry.

- Date of Birth: 24 March 1991
- Email: *tayyabmalik_pu@yahoo.com*
- Permanent Address: M. Tayyab s/o M. Rafique, Village and post office Abdal tehsil and district Gujranwala, Pakistan. Postal code: 52250.

PUBLICATIONS

Patents

1. M. S. Sharawi, M. Tayyab and A. Al-Sarkhi, ”Radio Frequency Sensor For Multi-phase Flow Determination”, *Submitted to USPO*, 2017.

Journal Papers

1. M. Tayyab, M. S. Sharawi and A. Al-Sarkhi, ”A Radio Frequency Sensor Array for Dielectric Constant Estimation of Multiphase Oil Flow in Pipelines”, *IEEE Sensor Journal*, 2017. [Under Review]

2. M. Tayyab, M. S. Sharawi, A. Shamim and A. Al-Sarkhi, ”A Low Complexity Radio Frequency Based Sensor Array For Lung Disease Detection Using Inkjet Printing”, *IET Microwaves, Antennas and Propagation*, 2017. [Under Review]

Conference Papers

1. M. Tayyab, M. S. Sharawi and A. Al-Sarkhi, ”Low Complexity RF Sensor for Multiphase Oil Flow Estimation in Pipelines”, *IEEE APS conference*, USA, 2017. [Accepted]

2. M. Tayyab, M. S. Sharawi and A. Shamim, ”A Wearable RF Sensor on Fabric Substrate for Pulmonary Edema Monitoring”, *IEEE Senset conference*, 2017.